3-24-2009

Frequency Diversity for Improving Synthetic Aperture Radar Imaging

Jawad L. Farooq

FREQUENCY DIVERSITY FOR
IMPROVING SYNTHETIC APERTURE RADAR IMAGING

DISSERTATION

Jawad Farooq, Major, USAF

AFIT/DEE/ENG/09-04

AFIT/DEE/ENG/09-04

FREQUENCY DIVERSITY FOR
IMPROVING SYNTHETIC APERTURE RADAR IMAGING

DISSERTATION

Presented to the Faculty

Graduate School of Engineering and Management

Air Force Institute of Technology

Air University

Air Education and Training Command

In Partial Fulfillment of the Requirements for the

Degree of Doctor of Philosophy

Jawad Farooq, B.S.E.E., M.S.C.S.

Major, USAF

March 2009

AFIT/DEE/ENG/09-04

Frequency Diversity for Improving Synthetic Aperture Radar Imaging

Jawad Farooq, B.S.E.E., M.S.C.S.
Major, USAF

Approved:
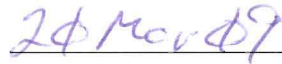
_____   20 Mar 2009
Maj Michael A. Saville, PhD   Date
Dissertation Advisor
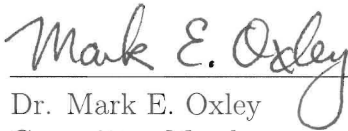
_____   20 Mar 09
Dr. Michael A. Temple   Date
Committee Member

_____   20 Mar 09
Dr. Mark E. Oxley   Date
Committee Member

Accepted:

_____   24 Mar 09
M. U. Thomas   Date
Dean, Graduate School of
Engineering and Management

AFIT/DEE/ENG/09-04

Abstract

Synthetic aperture radar (SAR) is a critical battlefield enabler as it provides imagery during day or night and in all-weather conditions. SAR image resolution is a function of the transmit signal parameters and collection time where classic measures of resolution depend on waveform bandwidth, operating frequency and sensor flight path. Improving resolution is challenging because of the two dimensional resolution: down-range and cross range. Decades of research exist for the down-range dimension, but very little exists for improving cross-range dimension.

Fine cross-range resolution requires a long collection time, which increases an airborne sensor's exposure to hostile forces and causes undesirable defocusing effects from uncontrolled platform motion and moving targets in the scene. For the first time, this research investigates techniques to improve cross-range resolution using waveform diversity. The importance of waveform diversity has been highlighted by senior U.S. Air Force leaders as a growing and vital part of future operational capabilities.

In this work, a novel theoretical framework is presented for using recent advances in frequency diversity arrays (FDAs). Unlike a conventional array, the FDA simultaneously transmits a unique frequency from each element in the array. As a result, special time and space properties of the radiation pattern are exploited to improve cross-range resolution. The idealized FDA radiation pattern is compared with and validated against a full-wave electromagnetic solver, and it is shown that the conventional array is a special case of the FDA. A new signal model, based on the FDA, is used to simulate SAR imagery of ideal point mass targets and the new model is used to derive the impulse response function of the SAR system, which is rarely achievable with other analytic methods.

This work also presents an innovative solution for using the convolution back-projection algorithm, the gold standard in SAR image processing, and is a significant

advantage of the proposed FDA model. The new FDA model and novel SAR system concept of operation are shown to reduce collection time by 33 percent while achieving a 4.5 dB improvement in cross-range resolution as compared to traditional imaging systems.

Acknowledgements

بِسْمِ اللّٰهِ الرَّحْمٰنِ الرَّحِيمِ

"In the name of God, the Beneficent, the Merciful"

Before all, I praise my Creator for all the favors He has bestowed upon me. I am ever grateful for all Your blessings: a beautiful wife, loving children, supportive parents, and all other gifts I cannot even begin to list. I was able to complete my studies at AFIT only through the knowledge and capabilities You have given me.

To my wife, your comfort and motivation have been invaluable these past three years. You are the bedrock of our family. Your support, through all the tough times, allowed me to keep focused on my studies and research and I am truly fortunate to have you by my side. To my beautiful children, you are the biggest gifts God has given me. Watching you grow and mature has been the most important and enjoyable part of our time here in Ohio. I pray that God blesses you in this life with that which is good, and in the hereafter with that which is good. Finally, I thank my parents for the encouragement and unconditional love throughout my life. You have been there for me at every milestone and I can never repay this debt to you.

Many students and faculty at AFIT provided crucial support. I especially want to thank my committee members. Maj. Saville, your driving motivation energized me to tackle the tough problems while encouraging me to stay the course. I am forever grateful for you scholarship, insight, and thought-provoking questions. Dr. Temple, thank you for introducing me to the subject of this research and for your wisdom on clearing all the hurdles to successfully complete AFIT requirements. Dr. Oxley, thank you for your substantial feedback during the course of this research.

Jawad Farooq

Table of Contents

List of Figures

Figure   Page

x

List of Tables

List of Symbols

List of Abbreviations

Frequency Diversity for Improving Synthetic Aperture Radar Imaging

I. Introduction

1.1 Research Motivation

Synthetic aperture radar (SAR) is an active radio frequency (RF) imaging technique that utilizes signal processing to produce high quality images. SAR systems gather information about a target area's reflectivity when illuminated by an electromagnetic (EM) wave at a specific radio frequency and from a particular aspect angle. Sequential observations of the target area, or scene, over varying aspect angles are processed to produce an estimate of the scene's reflectivity which is viewed similar to a photographic image. EM waves propagate virtually unattenuated through most atmospheric conditions enabling SAR to provide an all weather, day/night imaging capability.

Traditional SAR theory has shown that image resolution is a function of radar bandwidth, angular extent of collected data, and the operating frequency [29, 51] and is independent of range. The recent emergence of frequency diversity techniques within the arena of waveform diversity (WD) offers new prospects for SAR processing. Specifically, frequency diversity (FD), defined as the use of multiple or varying operating frequencies by the radar system, has demonstrated potential for SAR imaging [20–22].

Frequency diversity can be applied to SAR applications in one of two approaches. First, FD may be applied across the synthetic aperture baseline by varying center frequency from collection point to collection point as in [9, 34, 40, 47]. In this case the radar system selects an operating frequency according to some predefined ruleset. Given a set system bandwidth, the use of multiple operating frequencies effectively attains a larger overall bandwidth and directly improves range resolution.

With all the potential of WD for SAR imaging, little has been done to apply these techniques to improving resolution in the cross-range dimension. However, it is the time required for adequate cross-range resolution that keeps collection platforms and aircrews exposed to hostile forces. The FDA SAR processing aims to decrease this time when personnel and equipment are in harms way. Rather than applying FD sequentially as above, FD is applied simultaneously at each collection point in the SAR baseline via use of frequency diverse arrays (FDA). The authors in [2–4] demonstrate the ability to form range-dependent beam patterns by operating radiating elements across the physical array at different frequencies. Such frequency diverse arrays have been successfully applied in radar to space-time adaptive processing (STAP) based forward-looking radar scenarios using ground moving target indicator (GMTI) processing [5].

This document establishes a generalized formulation for waveform diversity applied to SAR. The majority of the effort focused on exploiting the unique array patterns generated by an FDA to improve image resolution in the cross-range dimension. The motivation behind this approach is an attempt at synthesizing an apparent collection aperture that is longer than what is actually subtended while retaining benefits of shorter synthetic apertures and integration times.

1.2   Research Scope and Assumptions

SAR imaging is an umbrella term that encompasses a number of specific applications including inverse synthetic aperture radar (ISAR) [51], interferometric SAR (InSAR) [43], spotlight SAR [12, 29], and stripmap SAR [51]. Thus, it is important to define at the outset which specific employment of SAR is utilized. This research considers airborne spotlight SAR and, although the models developed allow for generalization, simulations are performed for the broadside collection geometry with a linear flight path.

The location of the target scene relative to the radar is given by azimuth angle θ, elevation angle ψ, and range r. It has been shown that in spotlight SAR ψ is small and nearly constant during data collection, and θ is small and varies by only a few degrees [29]. These conditions allow the following small angle approximations to be used throughout the analytical development:

$$
\begin{aligned}
\sin(\varphi) &\approx \varphi\,,\\
\cos(\varphi) &\approx 1\,,\\
\tan(\varphi) &\approx \varphi\,.
\end{aligned}
\tag{1.1}
$$

A number of hardware and environmental factors influence signal amplitude and phase during data collection including transmit power, antenna efficiency, filter design, etc. While these factors contribute to any radar pulse return, SAR image reconstruction relies solely on target reflectivity and phase information in a scattered pulse return. Other amplitude and phase contributions are approximately constant over the spotlighted scene for the duration of data collection and provide no target information. Therefore, as is customary in SAR literature, these contributions are acknowledged during the development but not retained.

Analytical development is empirically validated through simulation. Ideal point targets are used and it is assumed reflectivity is invariant to both aspect angle and excitation frequency. Additionally, array pattern development and simulation assume ideal radiators with no inter-element coupling between antenna elements. These assumptions are common in SAR literature.

1.3 Document Overview

This document details the FDA SAR theory and methodology. Chapter II provides a summary of SAR imaging to introduce terminology and establish a basis for incorporating FDA processing. Common imaging scenarios and image reconstruction

methods are presented. Chapter III presents the theory of FDAs. Whereas previous analysis of FDAs was performed for one-dimensional (1-D) linear arrays, this chapter extends the development to a two-dimensional (2-D) planar arrays. Next, Chapter IV introduces a novel technique to produce a widebeam, wideband waveform using FDA technology. The new FDA transmit waveform is derived and waveform amplitude, phase, periodicity, and frequency characteristics are analyzed. Finally, Chapter V presents the core research of applying FDA processing to SAR. The approach for SAR processing synthesizes an apparent collection aperture that is longer than what is actually subtended yielding superior cross-range resolution. Finally, Chapter VI summarizes the document and proposes future research with regard to FDA and WD applied to SAR.

II. Synthetic Aperture Radar Imaging

Spotlight SAR imaging is introduced in this chapter. Although many introductory texts [12,29,51] cover the material thoroughly, two major challenges in SAR literature are the varied approach to describing the imaging problem and lack of standardized terminology, making it difficult for the unfamiliar to grasp the concepts. This chapter addresses these issues by establishing a novel, physically-based approach to describing SAR.

In Section 2.1, SAR imaging is presented in a geometrical framework to emphasize the three-dimensional (3-D) reality of data collection. A vector construct is used throughout the mathematical development as common across many disciplines. Most importantly, the remainder of the document utilizes the framework established to enable the development of SAR signal modelling and imaging within the context of waveform diversity. Next, Section 2.2 outlines the polar format and time domain backprojection image reconstruction algorithms. The point spread function (PSF) is the basic metric in SAR imaging and is derived for each algorithm. It is noted that for all the popularity of time domain backprojection, an analytical formulation for the PSF is not readily found in literature. The theory developed in this document allows this metric to be succinctly described. Finally, Section 2.3 reviews current research efforts in waveform diversity and improving SAR imaging, i.e., the two main thrusts of this research.

2.1 Background

Radar's historical mission has been to detect, range, and track objects using radio waves. The radar transmits an electromagnetic signal into space through an antenna. The energy propagates until it encounters and scatters off of some target. The term target in radar is application specific. Aircraft are targets of interest to air traffic control radars, while in maritime operations ships are of concern. In SAR imaging, a patch of terrain on the earth's surface is the desired target, or scene, of interest. A portion of the energy incident the target is scattered back towards the

radar where it is received by the antenna. This received signal carries information about the target. The time delay of the received signal is proportional to the round-trip range to the target and the received power carries information of the target's reflectivity or radar cross-section.

One metric used to describe the effectiveness of a radar system is range resolution. Range resolution specifies the ability to distinguish, or resolve, two targets in a radial direction from the radar. It is well-known that range resolution δ_x is improved with an increase in waveform bandwidth and is given by [29, 51]

$$\delta_x = \frac{c}{2B} \ ,\qquad(2.1)$$

where c is the speed-of-light and B is the 3 dB bandwidth. Improving range resolution through a variety of techniques has been an area of research for decades [15].

While it is critical to know a target's range, it is equally important to locate a target in cross-range, i.e., the target's angular location. Traditional radars are less effective at performing this function. Transmitted energy propagates spherically away from the radar. Reflected energy from two targets at the same range, but different angular locations, will arrive back at the radar simultaneously. The radar will be unable to discriminate between the two, yielding poor cross-range resolution. For a given target range R, center frequency wavelength λ, and actual array (aperture) size D, cross-range resolution δ_y is [29]

$$\delta_y = \frac{R\lambda}{D} \ .\qquad(2.2)$$

Cross-range resolution is improved with increased operating frequency (smaller λ) or increased aperture size.

Synthetic aperture radar (SAR) is a radar modality that simultaneously attempts to glean information about a target in both range and cross-range. Specifically, SAR imaging estimates the reflectivity function that can be interpreted similar to a

6
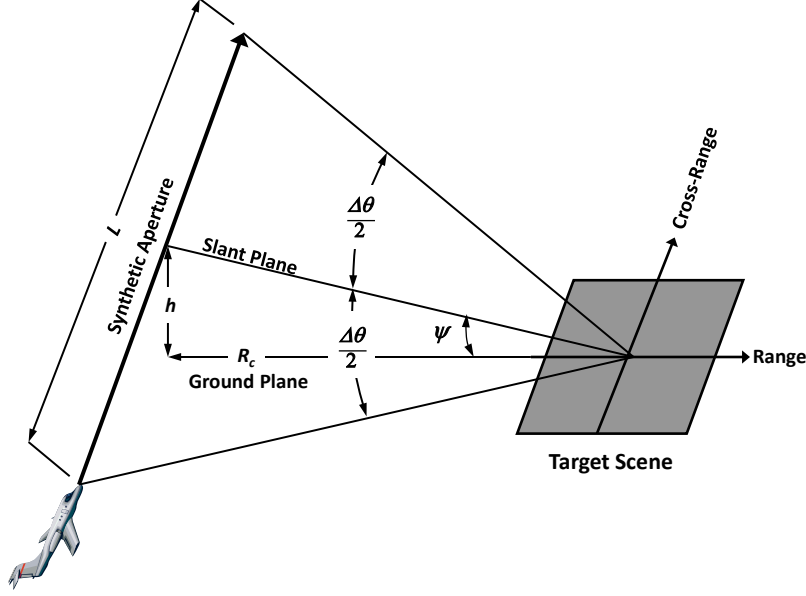
Figure 2.1: Overview of airborne spotlight SAR collection in broadside mode. The platform traverses a linear flight path of length L over which the synthetic aperture is formed. A series of M one-dimensional range profiles is generated at discrete points along L. Synthetic aperture length L, or conversely the angular extent of the collected data $\Delta\theta$, determines cross-range resolution in reconstructed image.

geospatial image. The requirement for SAR processing can be seen when considering an imaging example. Sub-meter image resolution is often desired in military applications. A realistic airborne collection scenario may require a 40 km operational standoff distance from the target area using an X-band radar ($f = 10$ GHz, $\lambda = 0.03$ m) with a desired range resolution of $\delta_x = 0.5$ m. Under these conditions, $B = 300$ MHz according to Equation (2.1). To achieve equal cross-range resolution with traditional processing, an antenna of size $D = 2,400$ m from Equation (2.2) is required. This is clearly unrealistic for airborne radar systems.

SAR processing alleviates the aperture size requirement by synthesizing a larger aperture. Figure 2.1 illustrates a typical SAR collection geometry. The collection platform with side-looking radar flies a linear path at altitude h and range R_c from scene center while coherently transmitting and receiving pulses. The dimension perpendicular to the flight path is the range dimension while that parallel to the flight path is the cross-range dimension. After transmitting M pulses, a series of M one-dimensional

range profiles are generated at equally spaced collection points along the flight path of length L. This set of points defines the synthetic aperture. The receive signals are coherently processed as if the data was collected from an array of stationary radars.

The total angular extent subtended by the synthetic aperture is $\Delta\theta$. It has been shown that cross-range resolution of spotlight SAR (to be discussed in Section 2.1.1) is [29, 51]

$$\delta_y = \frac{\lambda}{2\Delta\theta} \ .$$

(2.3)

Using the example previously mentioned, $\Delta\theta = 0.03$ rad to achieve $\delta_y = 0.5$ m cross-range resolution. With the small angle assumption $\sin(\varphi) \approx \varphi$, the required synthetic aperture length is $L = R_c \sin(\Delta\theta) = 1,200$ m, and the required synthetic aperture length is one-half the required real aperture size. The ideals of Equations (2.1) and (2.3) define the best case resolution. Noticeably absent in these two equations is the range variable R_c. In theory, SAR image resolution is independent of the range between the collection platform and scene. The limiting resolution is called the point spread function (PSF) and is the measure of SAR image quality.

In Figure 2.1, the ground plane is the plane in which the scene is actually located. The slant plane contains the line-of-sight (LOS) between the radar and scene. The slant plane lies at an angle ψ with respect to the ground plane. Data collection is performed in the slant plane and therefore SAR image reconstruction produces a slant plane image, i.e., the 3-D target scene is projected onto the 2-D slant plane. Throughout this document the term range refers to slant range unless specifically identified as ground range. Additionally, all image reconstruction is performed in the slant range. A two-dimensional ground plane image is easily produced by projecting the generated SAR image back onto the ground plane.

2.1.1 Collection Geometries and Terminology. The popularity of SAR imaging has led to many operating modes, with stripmap SAR and and spotlight SAR being the two prominent ones. Stripmap SAR was the first operating mode developed for SAR imaging [36, 37] and provides large area coverage with the trade-off of coarser
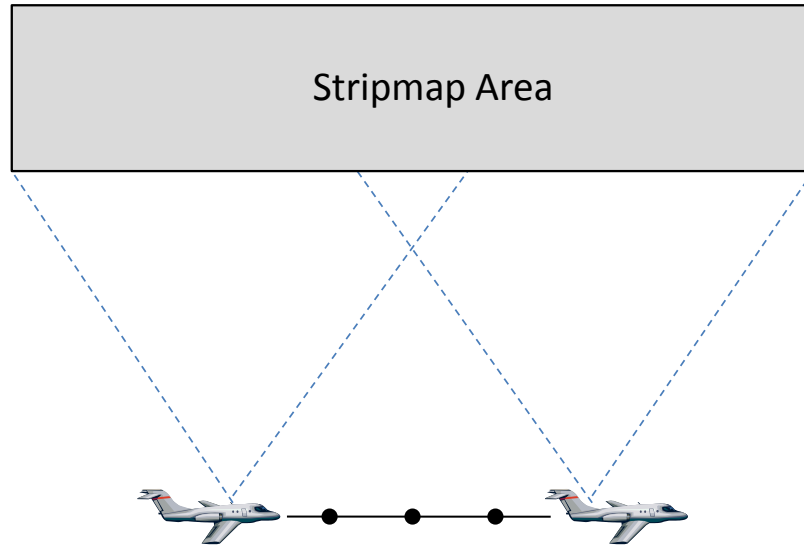
Figure 2.2: Imaging geometry for stripmap mode SAR. The side-looking radar is pointed perpendicular to the platform's velocity vector. The antenna pattern is fixed for the duration of the collection yielding a large coverage area. Solid circles indicate collection locations along the synthetic aperture.
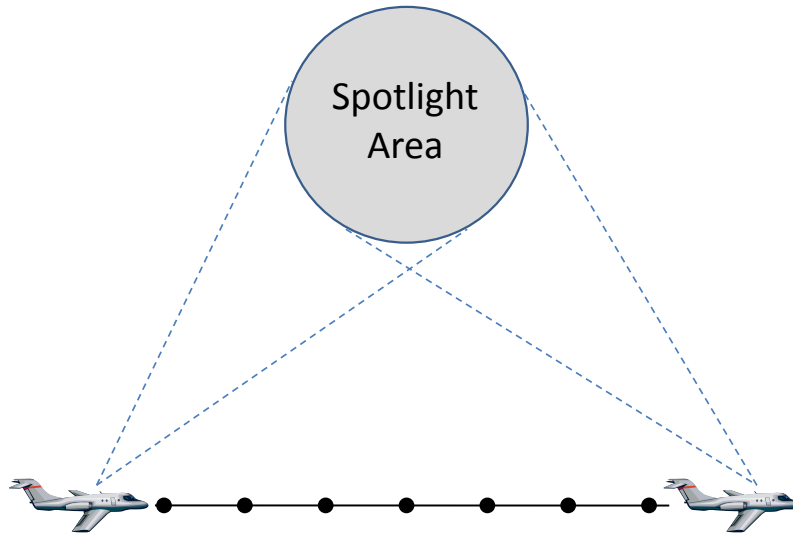
Figure 2.3: Spotlight SAR collection geometry. The radar mainbeam is continuously steered to illuminate a given patch of ground throughout the collection period, reducing coverage area compared to stripmap SAR but improving azimuth resolution in the target area. Solid circles indicate collection locations along the synthetic aperture.

cross-range resolution when compared to spotlight SAR. The imaging geometry for stripmap SAR is depicted in Figure 2.2. The side-looking radar is pointed perpendicular to the platform's velocity vector and is fixed for the duration of the collection. The antenna beam sweeps out a strip on the ground yielding a large coverage area. Solid circles indicate collection locations along the synthetic aperture. The amount of time a given target remains illuminated by the mainbeam is proportional to the beamwidth. With stripmap SAR, the best achievable azimuth resolution is [12]

$$\delta_y = \frac{D}{2} \ , \tag{2.4}$$

while range resolution given by Equation (2.1). Thus cross-range resolution is solely dependent upon real aperture size D. A smaller real aperture widens the mainbeam [8], illuminating targets for a longer period of time and yielding improved cross-range resolution.

Alternatively, spotlight SAR provides finer cross-range resolution for smaller coverage areas [39]. In the spotlight mode, the radar mainbeam is continuously steered to illuminate a specific patch of ground throughout the collection period as shown in Figure 2.3. This steering is performed either mechanically or electronically. All targets in the spotlighted area are illuminated for a longer time duration relative to stripmap SAR, which in turn improves azimuth resolution. Solid circles in the figure indicate collection locations along the synthetic aperture. Range and cross-range resolutions are given by Equation (2.1) and Equation (2.3) respectively. Although antenna size D does not directly affect resolution in spotlight SAR as was the case in stripmap mode, it does determine the radar footprint, i.e., the spotlighted area.

Within spotlight SAR, collection can either be broadside or squinted. In Figure 2.3, the synthetic aperture is centered on the scene in cross-range. This particular collection geometry is referred to as broadside operation. Squinted operation refers to a scenario where the synthetic aperture and scene centers are not aligned in cross-range. With forward squint, the target area is in the direction of velocity vector, i.e.,
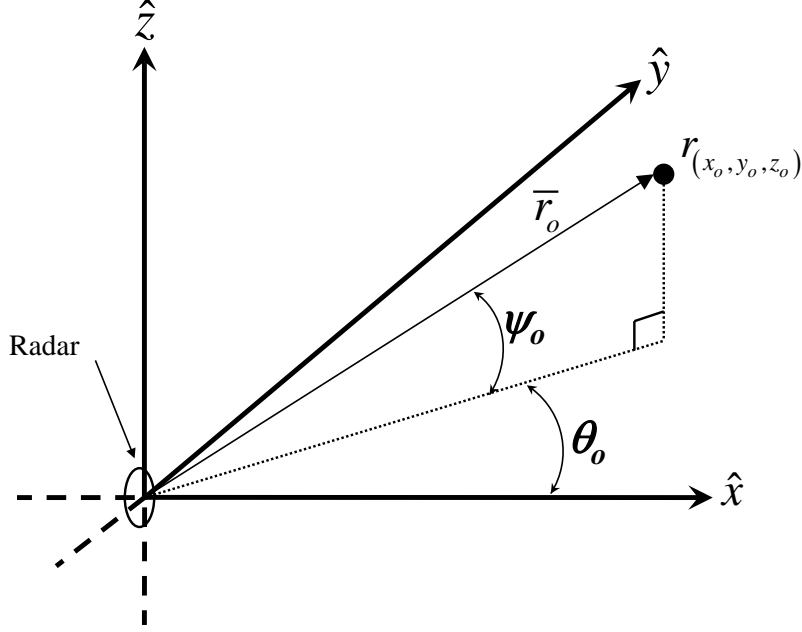
Figure 2.4: The radar-centric coordinate system is used to define a location in space. Radar boresight is along $\hat{\mathbf{x}}$. Azimuth angle θ is referenced to $\hat{\mathbf{x}}$ and is measured positive toward $\hat{\mathbf{y}}$. Elevation angle ψ is referenced to $\hat{\mathbf{x}}$ and is measured positive toward $\hat{\mathbf{z}}$.

the radar is moving toward the scene for the duration of the collection. In backward squint the radar is moving away from the scene for the duration of the collection.

Image reconstruction is performed through signal processing of the collected dataset, termed the phase history. The time interval required for the radar to traverse the synthetic aperture and collect the phase history is called the coherent processing interval (CPI). SAR processing is two-dimensional in both the range and cross-range domains. SAR literature has accepted terminology when referring to each of the two dimensions [51, 53]. The range domain is often referred to as fast-time because sampling is on the order of the operating frequency. For frequencies used in radar, this sampling requirement may be on the order of nanoseconds. The cross-range domain is often referred to as slow-time because sampling associated with the platform motion is on the scale of the pulse repetition interval, typically on the order of milliseconds.

2.1.2 Radar Coordinate System. The coordinate system for the signal model development is shown in Figure 2.4. Vectors are bold with an overbar or hat for unit vectors. SAR systems utilize side-looking radar whereby radar boresight is normal to the host platform velocity vector. The radar-centric coordinate system in Figure 2.4 is oriented such that the platform's velocity vector is parallel to $\hat{\mathbf{y}}$ and the radar boresight is along $\hat{\mathbf{x}}$. Azimuth angle θ is referenced to $\hat{\mathbf{x}}$ and is measured positive toward $\hat{\mathbf{y}}$. Elevation angle ψ is referenced to $\hat{\mathbf{x}}$ and is measured positive toward $\hat{\mathbf{z}}$.

The established geometry allows the location of any coordinate to be specified relative to the radar by its range r_o, azimuth angle θ_o, and elevation angle ψ_o as

$$
\begin{aligned}
\bar{\mathbf{r}}_o &= r_o \hat{\mathbf{r}}_o \\
&= r_o \left(\hat{\mathbf{x}} \cos \psi_o \cos \theta_o + \hat{\mathbf{y}} \cos \psi_o \sin \theta_o + \hat{\mathbf{z}} \sin \psi_o \right) \\
&= \hat{\mathbf{x}} \, x_o + \hat{\mathbf{y}} \, y_o + \hat{\mathbf{z}} \, z_o \, ,
\end{aligned}
\tag{2.5}
$$

where $\hat{\mathbf{x}}$, $\hat{\mathbf{y}}$, and $\hat{\mathbf{z}}$ are the Cartesian unit vectors,

$$
\begin{aligned}
x_o &= r_o \cos \psi_o \cos \theta_o = r_o \kappa_x \, , \\
y_o &= r_o \cos \psi_o \sin \theta_o = r_o \kappa_y \, , \\
z_o &= r_o \sin \psi_o = r_o \kappa_z \, ,
\end{aligned}
\tag{2.6}
$$

and

$$
\begin{aligned}
\kappa_x \left(\psi_o, \theta_o \right) &= \cos \psi_o \cos \theta_o \, , \\
\kappa_y \left(\psi_o, \theta_o \right) &= \cos \psi_o \sin \theta_o \, , \\
\kappa_z \left(\psi_o \right) &= \sin \psi_o \, .
\end{aligned}
\tag{2.7}
$$

In Equation (2.5), $\bar{\mathbf{r}}_o$ has magnitude r_o and direction given by the unit vector

$$
\hat{\mathbf{r}}_o = \hat{\mathbf{x}} \kappa_x + \hat{\mathbf{y}} \kappa_y + \hat{\mathbf{z}} \kappa_z \, .
\tag{2.8}
$$
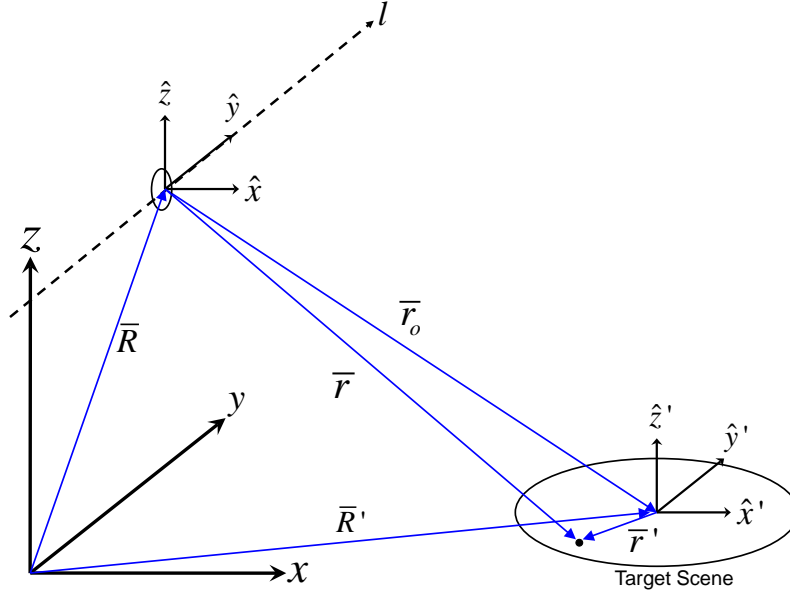
Figure 2.5: Radar coordinates for spotlight mode SAR operation. The radar maintains focus on a finite target area. Vectors $\overline{\mathbf{R}}$ and $\overline{\mathbf{R}}'$ define the locations of the radar and scene center, respectively, while $\bar{\mathbf{r}}$ defines the location of point $\bar{\mathbf{r}}'$ relative to the radar [46].

As discussed in Section 2.1.1, the spotlight mode operates while the radar maintains focus on a finite target area centered at some point as it traverses the synthetic aperture. Figure 2.5 illustrates the radar coordinate system for an airborne SAR operating in spotlight mode [46]. With the radar continuously steered to a fixed point at target scene center, $\bar{\mathbf{r}}_o$ varies during the CPI. It is convenient to define the radar location along the flight path as

$$\overline{\mathbf{R}}\left(t\right) = \hat{\mathbf{x}}R_x\left(t\right) + \hat{\mathbf{y}}R_y\left(t\right) + \hat{\mathbf{z}}R_z\left(t\right) \ . \tag{2.9}$$

The set of individual collection locations given by $\overline{\mathbf{R}}$ over time defines the synthetic aperture. Any arbitrary synthetic aperture, depicted by the dashed line l, can then

be characterized by point-mass equations of motion

$$
\begin{aligned}
R_x(t) &= R_{xo} + v_x t + \frac{1}{2} a_x t^2 \ , \\
R_y(t) &= R_{yo} + v_y t + \frac{1}{2} a_y t^2 \ , \\
R_z(t) &= R_{zo} + v_z t + \frac{1}{2} a_z t^2 \ ,
\end{aligned}
\tag{2.10}
$$

where (R_{xo}, R_{yo}, R_{zo}) identify the starting position, (v_x, v_y, v_z) specifies the velocity, and (a_x, a_y, a_z) is acceleration in the noted dimension.

In Figure 2.5, $\bar{\mathbf{r}}'$ defines the location of an arbitrary point r' in the scene in target-centric coordinates as

$$
\bar{\mathbf{r}}' = \hat{\mathbf{x}}\, x' + \hat{\mathbf{y}}\, y' + \hat{\mathbf{z}}\, z' \ ,
\tag{2.11}
$$

and $\bar{\mathbf{r}}$ describes the location of point r' with respect to the radar

$$
\bar{\mathbf{r}} = \bar{\mathbf{r}}_o + \bar{\mathbf{r}}' \ .
\tag{2.12}
$$

Lastly, $\overline{\mathbf{R}}'$ specifies the location of the target scene center with coordinate (X_c, Y_c, Z_c)

$$
\overline{\mathbf{R}}' = \hat{\mathbf{x}}\, X_c + \hat{\mathbf{y}}\, Y_c + \hat{\mathbf{z}}\, Z_c \ .
\tag{2.13}
$$

Using $\overline{\mathbf{R}}'$ and $\overline{\mathbf{R}}(t)$, the established geometry can mathematically define any spotlight imaging geometry, i.e., broadside, forward squint, or backward squint.

The scene consists of a finite rectangular volume V centered at $\overline{\mathbf{R}}'$, with

$$
V = [X_c - X_o, X_c + X_o] \times [Y_c - Y_o, Y_c + Y_o] \times [Z_c, Z_c + Z_o] \ .
\tag{2.14}
$$

Relative to scene center, the volume is bound in range by $\pm X_o$, by $\pm Y_o$ in cross-range, in height by Z_o.

14

From Figure 2.5, it is seen that

$$
\begin{aligned}
\bar{\mathbf{r}}_o(t) &= \mathbf{R}' - \mathbf{R}(t) \\
&= \hat{\mathbf{x}}\left[X_c - R_x(t)\right] + \hat{\mathbf{y}}\left[Y_c - R_y(t)\right] + \hat{\mathbf{z}}\left[Z_c - R_z(t)\right], \quad\quad (2.15)
\end{aligned}
$$

where the range $r_o = |\bar{\mathbf{r}}_o|$ is time dependent as

$$
r_o(t) = \sqrt{\left[X_c - R_x(t)\right]^2 + \left[Y_c - R_y(t)\right]^2 + \left[Z_c - R_z(t)\right]^2}. \quad\quad (2.16)
$$

Equating like terms in Equation (2.5) and Equation (2.15) leads to the following system of equations

$$
\begin{aligned}
r_o(t)\cos\psi_o\cos\theta_o &= X_c - R_x(t), \\
r_o(t)\cos\psi_o\sin\theta_o &= Y_c - R_y(t), \\
r_o(t)\sin\psi_o &= Z_c - R_z(t), \quad\quad (2.17)
\end{aligned}
$$

which can be solved to show

$$
\theta_o(t) = \tan^{-1}\left[\frac{Y_c - R_y(t)}{X_c - R_x(t)}\right], \quad\quad (2.18)
$$

and

$$
\psi_o(t) = \sin^{-1}\left[\frac{Z_c - R_z(t)}{r_o(t)}\right], \quad\quad (2.19)
$$

where both angles are explicitly parameterized with time. It is important to note that, in radar, time is customarily used to parameterize equations of motion and signals making the geometric expressions in Equation (2.16) to Equation (2.19) easy to work with in the context of signal processing.

    2.1.3 Signal Model Development.   Initially, the radar is treated as stationary and transmits a single pulse. In general, the transmit waveform $s(t)$ is conveniently

expressed in complex envelope notation as

$$s(t) = a(t) \exp \left\{ j \left[\omega_o t + \phi(t) \right] \right\} , \tag{2.20}$$

where $a(t)$ defines the instantaneous amplitude modulation of $s(t)$, $\omega_o = 2\pi f_o$ is the angular frequency, and $\phi(t)$ is a function of time defining the phase modulation of $s(t)$. For now, a continuous wave (CW) signal is assumed making $\phi(t) = \phi_o = 0$. In many radar operations, $a(t)$ is either a square wave or constant. The normalized transmitted radar signal is then simply

$$s(t) = \exp(j\omega_o t) . \tag{2.21}$$

After transmission, the normalized signal propagates with phase accrual as

$$s(t, \bar{\mathbf{k}}) = \exp \left[j \left(\omega_o t - \bar{\mathbf{k}}_o \cdot \bar{\mathbf{r}} \right) \right] , \tag{2.22}$$

where $\bar{\mathbf{k}}_o$ is the wavevector and denotes the radar LOS to the reference path

$$\bar{\mathbf{k}}_o = k_o \hat{\mathbf{r}}_o , \tag{2.23}$$

and wavenumber k_o is given by

$$k_o = \frac{\omega_o}{c} = \frac{2\pi}{\lambda_o} . \tag{2.24}$$

For the moment, it is convenient to set $\bar{\mathbf{r}}' = 0$ in Equation (2.12), reducing Equation (2.22) to

$$
\begin{aligned}
s(t, \bar{\mathbf{k}}) &= \exp \left[j \left(\omega_o t - \bar{\mathbf{k}}_o \cdot \bar{\mathbf{r}} \right) \right] \\
&= \exp \left[j \left(\omega_o t - \bar{\mathbf{k}}_o \cdot \bar{\mathbf{r}}_o \right) \right] \\
&= \exp \left[j \omega_o \left(t - t_o \right) \right] ,
\end{aligned} \tag{2.25}
$$

where

$$\begin{aligned}
\bar{\mathbf{k}}_o \cdot \bar{\mathbf{r}}_o &= k_o \left(\hat{\mathbf{x}} \kappa_x + \hat{\mathbf{y}} \kappa_y + \hat{\mathbf{z}} \kappa_z \right) \cdot r_o \left(\hat{\mathbf{x}} \kappa_x + \hat{\mathbf{y}} \kappa_y + \hat{\mathbf{z}} \kappa_z \right) \\
&= \omega_o \frac{r_o}{c} \left(\kappa_x^2 + \kappa_y^2 + \kappa_z^2 \right) \\
&= \omega_o t_o ,
\end{aligned} \tag{2.26}$$

and the propagation delay t_o from the radar to scene center is

$$t_o = \frac{r_o}{c} . \tag{2.27}$$

From Equation (2.25), it is seen that $s\left(t, \bar{\mathbf{k}}\right)$ is reduced from a spherical wave travelling away from the radar to a uniform plane wave [7], but the spherical wave is easily recovered. The phase accrued during propagation is nicely represented as a time delay

$$t_o = \frac{\sqrt{\left[x - R_x\left(t\right)\right]^2 + \left[y - R_y\left(t\right)\right]^2 + \left[z - R_z\left(t\right)\right]^2}}{c} , \tag{2.28}$$

where the coordinates x, y, z define the wave at any point in space. In the far-field, it is customary to approximate $s\left(t, \bar{\mathbf{k}}\right)$ as a uniform plane wave that is tangent to the spherical wavefront. In Section 2.2 it will be seen that, although phase history is collected for a 3-D scene, image reconstruction is performed in the x-y plane. Therefore, it is appropriate to define lines of uniform phase in the two dimensional reconstruction scene. Specifically, the slopes of these lines are of interest as they directly relate the orientation of the plane wave relative to propagation direction.

The slope $\partial x / \partial y$ is computed by implicitly differentiating x with respect to y in Equation (2.28). Assuming a stationary radar, i.e., eliminating time dependency of R_x, R_y, and R_z,

$$D\left[t_o\right] = D \left[\frac{\sqrt{\left(x - R_x\right)^2 + \left(y - R_y\right)^2 + \left(z - R_z\right)^2}}{c} \right] , \tag{2.29}$$

17

where $D[\cdot]$ denotes a partial derivative with respect to y $(\partial/\partial y)$. Simplification of Equation (2.29) yields

$$
\begin{aligned}
0 &= \frac{D\left[(x-R_x)^2 + (y-R_y)^2 + (z-R_z)^2\right]}{c2\sqrt{(x-R_x)^2 + (y-R_y)^2 + (z-R_z)^2}} \\
&= \frac{1}{c2r_o}\left\{D\left[(x-R_x)^2\right] + D\left[(y-R_y)^2\right] + D\left[(z-R_z)^2\right]\right\} \\
&= \frac{2(x-R_x)\frac{\partial x}{\partial y}}{c2r_o} + \frac{2(y-R_y)\frac{\partial y}{\partial y}}{c2r_o} + \frac{2(z-R_z)\frac{\partial z}{\partial y}}{c2r_o} \\
\frac{\partial x}{\partial y} &= -\frac{(y-R_y)}{(x-R_x)} - \frac{(z-R_z)}{(x-R_x)}\frac{\partial z}{\partial y} .
\end{aligned}
\tag{2.30}
$$

In Equation (2.30) only the first term is of interest for the x-y plane and represents the slope of the line of uniform phase. The angle θ' this line makes with the $\hat{\mathbf{y}}'$ axis is the inverse tangent of the slope

$$
\theta' = -\tan^{-1}\left[\frac{(y-R_y)}{(x-R_x)}\right] , \tag{2.31}
$$

whose magnitude at scene center $y = Y_c$, $x = X_c$ is the same as Equation (2.18) as shown in Figure 2.6.

This result is intuitive because the far-field uniform plane waves, waves with uniform amplitude and phase across the wavefront, travel normal to the radar LOS. However, it will be shown in Chapter V that FDA SAR processing takes advantage of non-uniform plane waves produced by an FDA. In that case, the propagating signal exhibits a uniform phasefront and uniform amplitude wavefront which are not co-planar. Planes of uniform amplitude are not normal to the radar LOS. This fact is a key characteristic of the FDA waveform exploited by FDA SAR processing.

Having discussed properties of the transmitted signal, the scattered and received signal is now considered. The propagating signal in Equation (2.22) scatters off the scene and a portion of the scattered energy is received back at the radar at a time delay proportional to the round-trip range. The pulse return is composed of a superposition

18
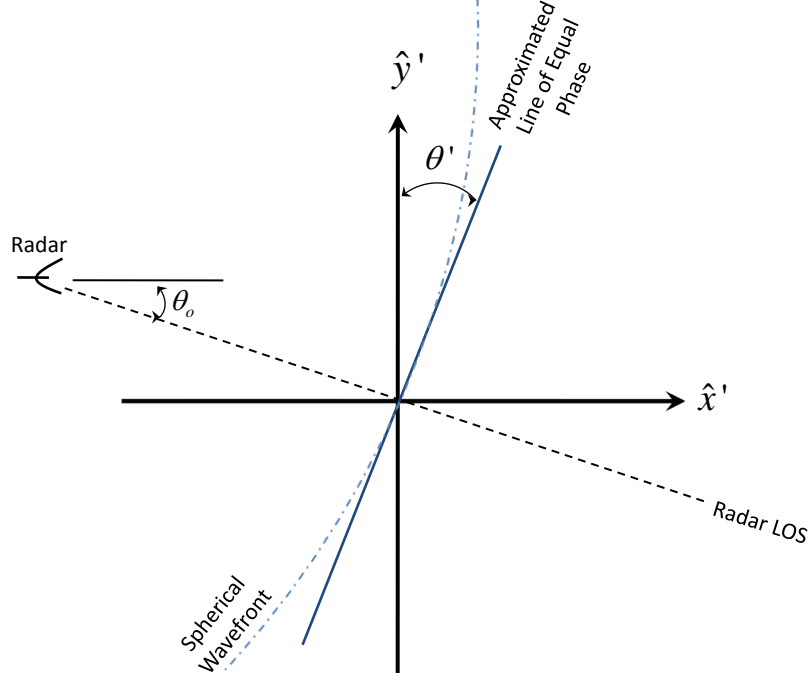
Figure 2.6: Lines of equal phase are normal to the radar LOS in traditional SAR imaging. When the radar squint angle is θ_o, equal phase lines lie at angle θ' with respect to $\hat{\mathbf{y}}'$.

of individual returns from all the scatterers in the volume V. When considering the scene as a continuum of scatterers, the pulse return $r\left(t, \bar{\mathbf{r}}', \bar{\mathbf{r}}_o\right)$ is often approximated using the Born approximation [23] as

$$
\begin{aligned}
r\left(t, \bar{\mathbf{r}}', \bar{\mathbf{r}}_o\right) &= \int_V d\bar{\mathbf{r}}' \rho\left(\bar{\mathbf{r}}'\right) \sqrt{P_r} \exp\left[j\left(\omega_o t - 2\,\bar{\mathbf{k}}_o \cdot \bar{\mathbf{r}}\right)\right] \\
&= \int_V d\bar{\mathbf{r}}' \rho\left(\bar{\mathbf{r}}'\right) \sqrt{P_r} \exp\left\{j\left[\omega_o\left(t - 2t_o\right) - 2\,\bar{\mathbf{k}}_o \cdot \bar{\mathbf{r}}'\right]\right\} \\
&= \sqrt{P_r} \exp\left[j\omega_o\left(t - 2t_o\right)\right] \int_V d\bar{\mathbf{r}}' \rho\left(\bar{\mathbf{r}}'\right) \exp\left(-j2\,\bar{\mathbf{k}}_o \cdot \bar{\mathbf{r}}'\right) \,, \quad (2.32)
\end{aligned}
$$

where $\rho\left(\bar{\mathbf{r}}'\right)$ is the reflectivity function of the continuum of scatterers in the scene and P_r is the ideal receive power [26]

$$
P_r = \frac{P_t G^2 \lambda^2}{(4\pi)^3 \, r_o^4} \,. \tag{2.33}
$$

19

In Equation (2.33), P_t is the transmit power, G is antenna gain, λ is wavelength, and r_o is range. In SAR imaging, the value of P_r is generally not of interest. The receive power is approximately constant across the scene and provides no target information. Rather, phase information and target reflectivity in the integrand of Equation (2.32) are of interest, which is why Equation (2.20) and Equation (2.22) were normalized.

The nature of SAR imaging is such that the radar samples the environment in the fast-time and slow-time dimensions. Signal processing theory dictates sampling requirements in order to fully capture frequency content in the signal. In fast-time processing, it is well-known that a signal $f(t)$ must be sampled at twice its bandwidth in order to reconstruct $f(t)$ from its samples. Failure to meet this criteria results in aliasing and distortion of $f(t)$ upon reconstruction [32, 49]. Similar sampling requirements exist in the slow-time domain.

The radar traverses the synthetic aperture while emitting a series of pulsed waveforms that serve to sample the scene in slow-time. The timing between pulses is the pulse repetition interval (PRI) whose inverse is the pulse repetition frequency (PRF). It is shown in [29, 51] that the PRI is dependent upon the scene size in cross-range, i.e., the value of Y_o in Equation (2.14). In fast-time processing, failure to meet minimum temporal sampling requirements results in aliasing, i.e., sampling rates are inadequate to accurately reconstruct a continuous time signal using discrete samples. In the counterpart slow-time domain, sampling is performed spatially. Therefore, failure to meet sampling requirements along the synthetic aperture results in spatial aliasing and the scene reflectivity cannot be reconstructed with the discrete spatial samples. When manifested in the reconstructed image, targets are not correctly located at the proper cross-range positions. Cross-range, or slow-time, processing is often related to Doppler sensing because of the well-known Doppler-PRI relationship [49, 51, 53].

In [29], the minimum increment of azimuth angle θ between successive samples along the synthetic aperture for broadside spotlight SAR imaging is shown to be

$$\delta\theta = \frac{\lambda}{4Y_o} \ . \tag{2.34}$$

When θ is small, as is often the case in spotlight SAR imaging, the required maximum distance Δ_y between samples along the y-axis is shown to be

$$\Delta_y \leq \frac{\lambda R_c}{4Y_o} \ . \tag{2.35}$$

With platform velocity v_y along the y-axis, the minimum PRF is then

$$\text{PRF}_{\min} = \frac{v_y}{\Delta_y} \ . \tag{2.36}$$

Assuming a constant velocity, Equation (2.36) results in an equally spaced set of collection points along the synthetic aperture. The number of pulses M transmitted during data collection is given by

$$M = \frac{L}{\Delta_y} \ , \tag{2.37}$$

where L is the total length of the synthetic aperture shown in Figure 2.1.

2.2 *Image Reconstruction*

SAR imaging can be developed using linear systems theory. Data collection is the forward problem. Given a set of discrete scatterers, which in the limiting case is a continuum, and known input (the transmitted pulse), a deterministic output $r\left(t, \bar{\mathbf{r}}', \bar{\mathbf{r}}_o\right)$ is produced. This process can be represented as a transformation $\mathcal{L}$ that operates on the scene reflectivity function:

$$r\left(t, \bar{\mathbf{r}}', \bar{\mathbf{r}}_o\right) = \mathcal{L}\left\{\rho\left(\bar{\mathbf{r}}'\right)\right\} \ . \tag{2.38}$$

Image reconstruction is the inverse problem where processing aims to produce an approximation to the reflectivity function, denoted $\hat{\rho}\left(\bar{\mathbf{r}}'\right)$, by applying inverse transformation (assuming it exists) $\mathcal{L}^{-1}$ on the compact-support phase history such that

$$\hat{\rho}\left(\bar{\mathbf{r}}'\right) \approx \mathcal{L}^{-1}\left\{r\left(t, \bar{\mathbf{r}}', \bar{\mathbf{r}}_o\right)\right\} \ . \tag{2.39}$$

In practical terms, $\mathcal{L}^{-1}$ is the reconstruction algorithm. All reconstruction algorithms have various limitations such that only an estimate $(\hat{\rho})$ of the actual scene reflectivity (ρ) is produced. Numerous frequency and time domain reconstruction algorithms exist and are covered extensively in the literature [12, 29, 51]. Though all algorithms effectively address the inverse image formation problem, each inherently has advantages and disadvantages. Commonly used Fast Fourier Transform (FFT) based techniques include wavefront reconstruction [51], range migration algorithm [12], and polar reformatting [29]. The time domain backprojection and time domain correlation algorithms operate directly on temporal data [51]. This section presents two commonly used reconstruction algorithms, polar format algorithm [29] and time domain backprojection, for the purpose of demonstrating imaging from FDA SAR.

Section 2.1 introduced SAR for an arbitrary spotlight collection geometry (squint or broadside) and synthetic aperture path (linear, circular, etc.). In the following discussion and the remainder of this document, discussion is emphasized for the broadside mode with linear synthetic aperture collection geometry. In this case, geometry is specified by the flight path in Equation (2.9) with

$$\begin{aligned}
R_x\left(t\right) &= 0 \ , \\
R_y\left(t\right) &\in \left[-\frac{L}{2}, \frac{L}{2}\right] \ , \\
R_z\left(t\right) &= h \ ,
\end{aligned} \tag{2.40}$$

and scene center at $(X_c, 0, 0)$. Additionally, the synthetic aperture length L is small compared to range r_o, making the elevation angle ψ_o approximately constant over the

CPI as

$$\psi_o = \tan^{-1}\left(-\frac{h}{X_c}\right) .$$

(2.41)

2.2.1 Polar Format Algorithm. Discussion of polar format algorithm (PFA) begins with introduction of the linear frequency modulated (LFM) waveform. LFM is the most common waveform used in general radar applications [25] and in imaging radar [29] specifically. This waveform is comparatively simple to generate and has desirable pulse compression characteristics, highly beneficial in SAR. Yet, it also lends itself to a simple understanding for constructing $\mathcal{L}^{-1}$.

An LFM pulse $s_{LFM}(t)$ is described by [29]

$$s_{LFM}(t) = \text{rect}\left(\frac{t}{\tau_c}\right)\exp\left[j\left(\omega_c t + \alpha t^2\right)\right] ,$$

(2.42)

where ω_c is the center frequency, τ_c is the pulse width, and

$$\text{rect}(\varphi) = \begin{cases} 1 & |\varphi| \leq \frac{1}{2} \\ 0 & \text{else} \end{cases} .$$

(2.43)

This waveform is composed of a linear phase term $\omega_c t$ and quadratic phase term αt^2. Because frequency is the time derivative of phase, the term $2\alpha t$ increases, or ramps, frequency linearly with time. In Equation (2.42) α is called the chirp rate. The LFM waveform spans the radian frequency range $[\omega_o - \alpha\tau_c , \omega_o + \alpha\tau_c]$ such that the total bandwidth (Hertz) is

$$B_{LFM} = \frac{2\alpha\tau_c}{2\pi} = \frac{\alpha\tau_c}{\pi} .$$

(2.44)

The LFM waveform is used with the SAR collection geometry in Figure 2.7. This waveform is discussed again in Chapter V where it is compared to the FDA waveform developed under this research.

Figure 2.7 shows the collection geometry of Figure 2.5 viewed along **y**. From a given location on the synthetic aperture, the two-way time delay τ_o to scene center is

23
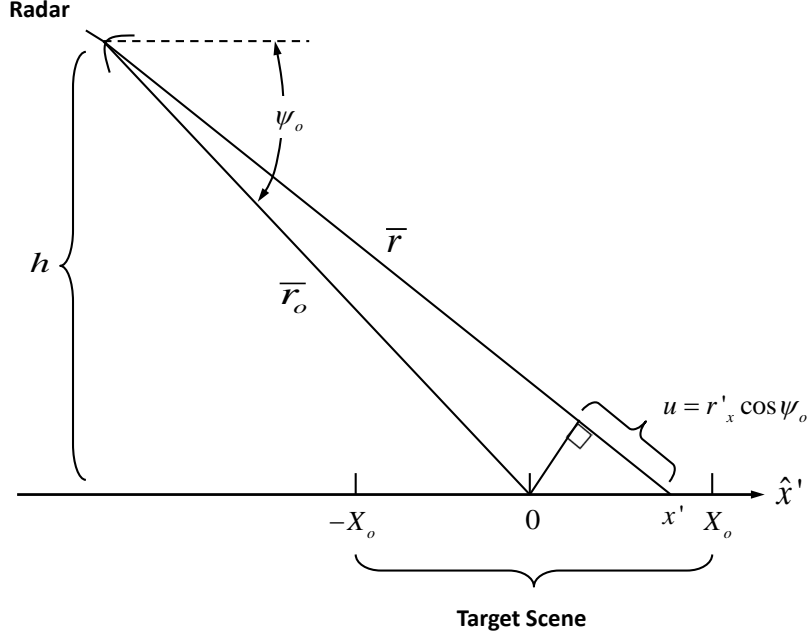
Figure 2.7: Collection geometry of Figure 2.5 viewed along the cross-range axis. The range from the radar to scene center is r_o. The additional distance to an arbitrary scatterer is given by $x' \cos \psi_o$. Figure based on development in [29].

proportional to slant range r_o and is given by

$$\tau_o = 2t_o \ , \tag{2.45}$$

with t_o given in Equation (2.27). Relative to τ_o, the additional round-trip time τ' to an arbitrary point $\mathbf{r}'$ in the scene with slant range

$$|\bar{\mathbf{r}}| = r_o + u \ , \tag{2.46}$$

is a function of additional propagation distance u

$$\tau'(u) = \frac{2u}{c} \ , \tag{2.47}$$

where

$$u(x') = x' \cos \psi_o \ , \tag{2.48}$$

24

as seen in Figure 2.7. The illuminated scene extends from $-X_o$ to X_o in the ground plane. The corresponding slant plane ranges varies from $-u_1$ to u_1, where $u_1 = X_o \cos \psi_o$. Considering long standoff distances and the small scene sizes typically encountered with spotlight SAR, the grazing angle ψ_o is approximated as constant between $-X_o$ and X_o.

The scene is composed of a continuum of scatterers characterized by complex microwave reflectivity $\rho(\bar{\mathbf{r}}')$, which can also be written as $\rho(u)$ from Equation (2.48), that scales the transmitted pulse upon scattering. The pulse return $r(t)$ is composed of return signals from all individual scatterers in the scene and is expressed as

$$r(t) = \int_{-u_1}^{u_1} du \, \rho(u) \exp\left(j \left\{ \omega_c \left[t - \tau_o - \tau'(u) \right] + \alpha \left[t - \tau_o - \tau'(u) \right]^2 \right\} \right) . \qquad (2.49)$$

The radar receiver removes known features of the recovered signal, and in SAR is simply a mixing operation with a chirp of the opposite ramp. This process is known as deramping [29] where the deramp signal

$$\exp\left\{ -j \left[\omega_c \left(t - \tau_o \right) + \alpha \left(t - \tau_o \right)^2 \right] \right\} , \qquad (2.50)$$

is a signal referenced to the scene center. The deramped pulse return is

$$r_D(u) = \int_{-u_1}^{u_1} du \, \rho(u) \exp\left(j \left\{ \alpha \tau'(u)^2 - \tau'(u) \left[\omega_c + 2\alpha \left(t - \tau_o \right) \right] \right\} \right) . \qquad (2.51)$$

When substituting Equation (2.47) into Equation (2.51), the first term in the exponential is eliminated by

$$\alpha \tau'(u)^2 = \alpha \left(\frac{2u}{c} \right)^2 = \frac{4\alpha u^2}{c^2} \approx 0 , \qquad (2.52)$$

25

given that, in practice, $4\alpha u^2$ is orders of magnitude smaller than c^2. The deramped signal reduces to

$$r_D(u) \approx \int_{-u_1}^{u_1} du\, \rho(u) \exp\left(-ju\left\{\frac{2}{c}[\omega_c + 2\alpha(t-\tau_o)]\right\}\right) . \qquad (2.53)$$

The expression in Equation (2.53) has the well-known form of a Fourier Transform (FT), and, in fact, is the FT of the scene reflectivity $\rho(u)$ with kernel $\exp(-j\,u\,U)$. Thus, the deramped return is the FT of $\rho(u)$

$$r_D(u) = \mathcal{F}\{\rho(u)\} , \qquad (2.54)$$

where $\mathcal{F}$ denotes the FT. Equation (2.54) suggests that $\mathcal{L}^{-1} = \mathcal{F}^{-1}$ where $\mathcal{F}^{-1}$ is the Inverse Fourier Transform (IFT). In the strict sense, $\mathcal{L}^{-1}$ must be approximated because of the compact support of $\rho(u)$. Recall that r_D is based on a specific range of spatial frequencies given by [29]

$$\frac{2}{c}(\omega_c - \pi B_{LFM}) \leq U \leq \frac{2}{c}(\omega_c + \pi B_{LFM}) , \qquad (2.55)$$

which can be written in the spatial frequency domain as

$$2k_c - \frac{\Delta k_x}{2} \leq k_x \leq 2k_c + \frac{\Delta k_x}{2} . \qquad (2.56)$$

Center frequency and bandwidth dictate the spatial frequencies traversed. The set of spatial frequencies in Equation (2.56) are centered at

$$\frac{2\omega_c}{c} = 2k_c = \frac{4\pi}{\lambda_c} , \qquad (2.57)$$

with spectral support, or bandwidth

$$\Delta k_x = \frac{2}{c}(2\pi B_{LFM}) . \qquad (2.58)$$

The Projection-Slice Theorem [29] is key to the PFA and is introduced next. Consider the geometry presented in Figure 2.4 where the radar emits a wave propagating along the x axis with targets in the far-field. Upon scattering and reception by the radar, each pulse return time sample corresponds to a constant range sphere in the y-z dimensions. These spheres in the far-field can be approximated as planes [7], i.e., the plane wave approximation in EM theory. A given sample in the pulse return then does not represent reflectivity at a particular point in the scene, rather it is a composite response of integrated returns from all scatterers located on the corresponding plane projected onto the x-axis. The measured reflectivity $\rho(x')$ is defined by projecting the three-dimensional $\rho(\mathbf{\bar{r}}')$ into one dimension as

$$\rho(x') = \iint\limits_{-\infty}^{\infty} dy'\, dz'\, \rho(\mathbf{\bar{r}}') \ . \tag{2.59}$$

The key concept enabling an efficient algorithm for image reconstruction can now be introduced. The Fourier transform of $\rho(\mathbf{\bar{r}}')$ is given by

$$\zeta(k_x, k_y, k_z) = \iiint\limits_{-\infty}^{\infty} dx'\, dy'\, dz'\, \rho(\mathbf{\bar{r}}') \exp\left[-j\left(x'k_x + y'k_y + z'k_z\right)\right] \ . \tag{2.60}$$

Using the Projection-Slice Theorem, the FT of Equation (2.59) is identical to the one-dimensional FT obtained by evaluating $\zeta(k_x, k_y, k_z)$ along the k_x dimension given by

$$\int\limits_{-\infty}^{\infty} dx'\, \rho(x') \exp\left(-jx'k_x\right) = \zeta(k_x, 0, 0) \ . \tag{2.61}$$

Both Equation (2.53) and Equation (2.61) are of the exact form and directly lead to the fact that each deramped return signal $r_D(t)$ is a trace of $\zeta(k_x, k_y, k_z)$. The rotational property of FT states that if $f(x')$ and $F(k_x)$ are FT pairs, then a θ-rotated version of $f(x')$ is a θ-rotated version of $F(k_x)$. Therefore, the angular orientation
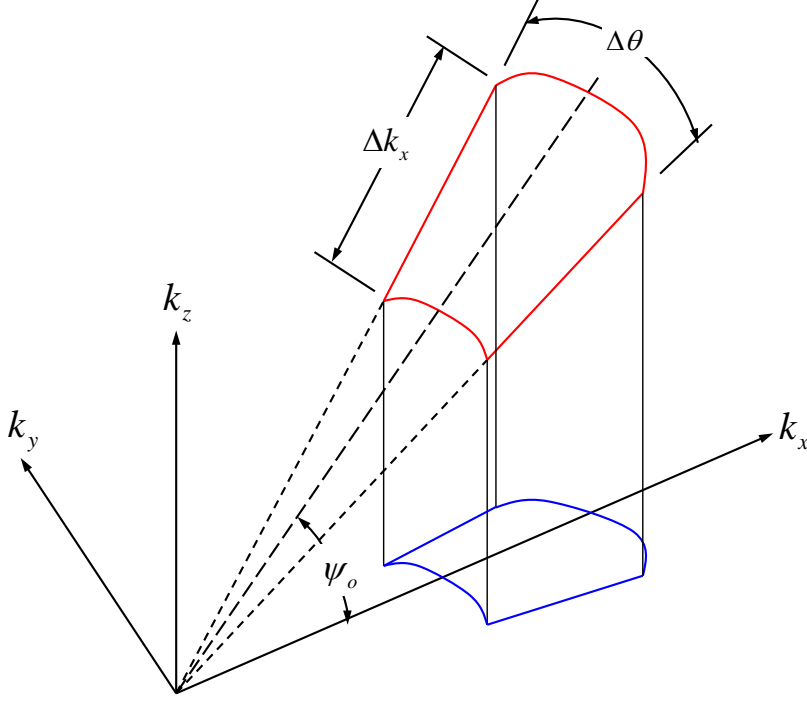
Figure 2.8: The set of deramped returns forms the red collection surface in the spatial frequency domain. This data produces a slant plane image. A ground plane image is produced by projecting the collected data onto the k_x-k_y plane in the Fourier domain as shown in blue. Figure based on development in [29].

of the trace defined in Equation (2.53) in the spatial frequency domain is coincident with the aspect angle θ from which the data is collected.

The Projection Slice Theorem is critical as it implies that image reconstruction is possible provided a sufficient number of one-dimensional projection functions from different viewing angles are obtained. The set of all processed returns along the synthetic aperture creates a collection surface in the spatial frequency domain as illustrated by the red outline in Figure 2.8. This figure represents slant plane data collected in the broadside collection geometry.

Ideally, 2-D image reconstruction is then simply performed via a 2-D IFT

$$\hat{\rho}\left(\bar{\mathbf{r}}'\right) = \mathcal{F}^{-1}\left\{r_D\left(u\right)\right\} = \iint\limits_{-\infty}^{\infty} dk_x\, dk_y\, r_D\left(u\right) \exp\left[j\left(x'k_x + y'k_y\right)\right] . \qquad (2.62)$$
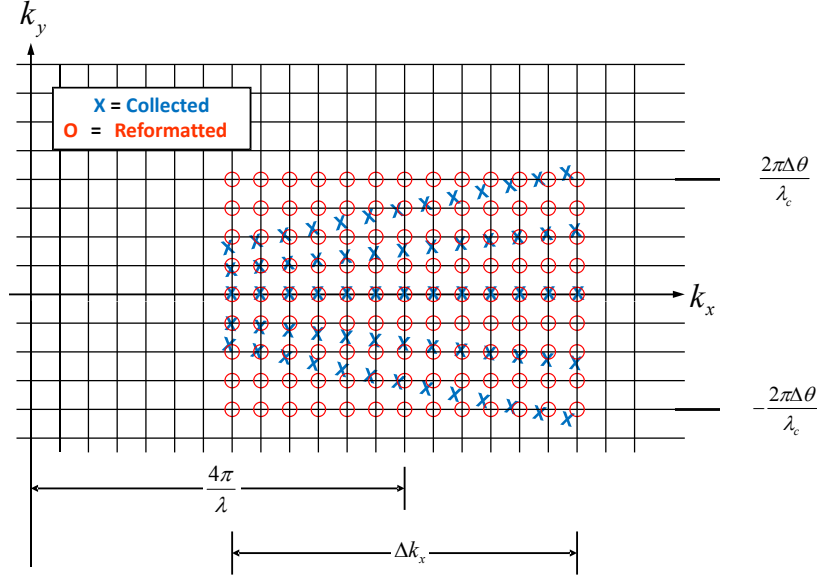
Figure 2.9: Collected data samples (blue X symbols) reside on a polar raster in the Fourier domain. To take advantage of FFT techniques, the original data is interpolated onto a Cartesian grid. The reformatted data (red O symbols) is shown in the figure. Figure based on development in [29].

An IFT of the deramped phase history produces a slant plane image. When the collection surface is projected onto the k_x-k_y plane (the blue surface in Figure 2.8), a ground plane image is formed.

The ideal image reconstruction of Equation (2.62) is not practical as the phase history provides a compact support region over k_x and k_y as seen in Figure 2.8. Detailed analysis and implications of the compact support regions is given in [38]. Additionally, in practice, the radar receiver samples and stores the pulse returns. Thus, FT and IFT presented above are implemented by the Discrete Fourier Transform (DFT) and Inverse Discrete Fourier Transform (IDFT). Due to the rotational property of the FT, the discrete data do not reside on a Cartesian grid. Instead, collected data samples (blue X symbols) in Figure 2.9 reside on a polar raster in the spatial frequency domain. To take advantage of Inverse Fast Fourier Transform (IFFT) techniques, this polar formatted data must first be interpolated in two dimensions onto a Cartesian grid. The interpolated points (red O symbols) are shown in Figure 2.9. This interpolation process (conversion from X located to O located data) is called polar

29

reformatting. Simply performing an IFFT on the collected data leads to phase errors and causes image defocusing which becomes more pronounced as the scatterer distance increases from scene center [29]. A sufficiently robust interpolator must be used to ensure no loss of high spatial frequency data. Once interpolation is performed, the set of spatial frequencies k_y represented in the collected data is seen in Figure 2.9 to be

$$
\begin{aligned}
-\frac{2\pi\Delta\theta}{\lambda_c} \leq & \ k_y \ \leq \frac{2\pi\Delta\theta}{\lambda_c} \\
-k_c\Delta\theta \leq & \ k_y \ \leq k_c\Delta\theta \ .
\end{aligned}
\tag{2.63}
$$

Equation (2.62) is modified to reflect compact support regions and interpolation by [53]

$$
\begin{aligned}
\hat{\rho}\left(\bar{\mathbf{r}}'\right) \ = \ & \int\!\!\!\int_{-\infty}^{\infty} dk_x \, dk_y \, W_x\left(k_x\right) W_y\left(k_y\right) I\left(k_x, \tilde{k}_x\right) I\left(k_y, \tilde{k}_y\right) \\
& \times r_D\left(u\right) \exp\left[j\left(x'k_x + y'k_y\right)\right] \\
= \ & \mathcal{L}^{-1}\left[r_D\left(u\right)\right] \ .
\end{aligned}
\tag{2.64}
$$

Compact support regions in Equations (2.55) and (2.63) are represented as windows in the spatial frequency domain as

$$
W_x\left(k_x\right) = \text{rect}\left(\frac{k_x - 2k_c}{\Delta k_x}\right) \ ,
\tag{2.65}
$$

and

$$
W_y\left(k_y\right) = \text{rect}\left(\frac{k_y}{2k_c\Delta\theta}\right) \ ,
\tag{2.66}
$$

respectively. Interpolation from k_x to $\tilde{k}_x$ and from k_y to $\tilde{k}_y$, where $(\tilde{k}_x, \tilde{k}_y)$ are rectangular grid points, is represented by $I(k_x, \tilde{k}_x)$ and $I(k_y, \tilde{k}_y)$ respectively.

Range and cross-range resolutions are completely defined by the limits of integration imposed by Equation (2.65) and Equation (2.66). In deriving the PSF,

an single point scatter with complex reflectivity $\rho_{\bar{\mathbf{r}}'}$ is assumed in the target area. An ideal point scatterer has uniform frequency content across k_x, k_y in the spatial frequency domain and

$$r_D(u) = \mathcal{F}\left\{\rho(\bar{\mathbf{r}}') = \rho_{\bar{\mathbf{r}}'}\delta(\bar{\mathbf{r}}')\right\} = \rho_{\bar{\mathbf{r}}'} . \tag{2.67}$$

Incorporating the sample support into the limits of integration and after interpolation, Equation (2.64) becomes

$$\text{PSF}(x', y') = \rho_{\bar{\mathbf{r}}'} \int\limits_{2k_c - \frac{\Delta k_x}{2}}^{2k_c + \frac{\Delta k_x}{2}} dk_x \exp(jx'k_x) \int\limits_{-k_c\Delta\theta}^{k_c\Delta\theta} dk_y \exp(jy'k_y) , \tag{2.68}$$

and defines the PSF. The first integral is reduced as

$$\int\limits_{2k_c - \frac{\Delta k_x}{2}}^{2k_c + \frac{\Delta k_x}{2}} dk_x \exp(jx'k_x) = \left.\frac{\exp(jx'k_x)}{jx'}\right|_{2k_c - \frac{\Delta k_x}{2}}^{2k_c + \frac{\Delta k_x}{2}} . \tag{2.69}$$

Substituting in the limits of integration and simplifying using Euler's formula

$$\exp(j\varphi) = \cos(\varphi) + j\sin(\varphi) , \tag{2.70}$$

produces the principle cut of the PSF along the range axis

$$
\begin{aligned}
\text{PSF}(x')_{\text{range}} &= \frac{\exp(jx'2k_c)\left[\exp\left(jx'\frac{\Delta k_x}{2}\right) - \exp\left(-jx'\frac{\Delta k_x}{2}\right)\right]}{jx'} \\
&= \exp(jx'2k_c)\,\Delta k_x\,\text{sinc}\left(x'\frac{\Delta k_x}{2}\right) ,
\end{aligned}
\tag{2.71}
$$

where

$$\text{sinc}(\varphi) = \frac{\sin(\varphi)}{\varphi} . \tag{2.72}$$

31

The first nulls of the sinc $(\cdot)$ function yields the range resolution and occurs at

$$
\begin{aligned}
x' \frac{\Delta k_x}{2} &= \pm \pi \\
x' \frac{(2\pi B_{LFM})}{c} &= \pm \pi \\
x' &= \pm \frac{c}{2 B_{LFM}} \;,
\end{aligned}
\tag{2.73}
$$

and the result agrees with Equation (2.1).

Evaluating the second integral in Equation (2.68) produces the principle cut of the PSF along the cross-range axis

$$
\int_{-k_c \Delta\theta}^{k_c \Delta\theta} dk_y \exp\left(jy'k_y\right) = \left. \frac{\exp\left(jy'k_y\right)}{jy'} \right|_{-k_c \Delta\theta}^{k_c \Delta\theta} .
\tag{2.74}
$$

Following development from Equation (2.69) to Equation (2.73) it is straightforward to show the cross-range component of the PSF is

$$
\mathrm{PSF}\,(y')_{\mathrm{cross-range}} = 2k_c \Delta\theta \, \mathrm{sinc}\,(y' k_c \Delta\theta) \;,
\tag{2.75}
$$

and that cross-range resolution agrees with Equation (2.3). The overall PSF is a two-dimensional sinc $(\cdot)$ function given by the product of Equation (2.71) and Equation (2.75) is

$$
\mathrm{PSF}\,(x', y') = |\rho_{\bar{\mathbf{r}}'}| \, 2k_c \Delta\theta \Delta k_x \mathrm{sinc}\left(x' \frac{\Delta k_x}{2}\right) \mathrm{sinc}\,(y' k_c \Delta\theta) \;,
\tag{2.76}
$$

as only pixel magnitude is shown after image reconstruction.

The greatest advantage of the PFA and other FFT-based algorithms is speed. Modern computing power allows for efficient computer of large IFFT's. Unfortunately, the use of FFT-based algorithms present operational challenges. The polar-to-rectangular re-gridding operation is computationally expensive, and attainable image quality is sufficient in case of relatively small bandwidths [19]. Additionally, the

phase history must be acquired over the full synthetic aperture before processing can begin, i.e., range and cross-range processing are coupled. Finally, FFT-based algorithms are sensitive to motion errors in the flight path resulting in poor focus for large integration angles and/or large motion errors [44]. Time domain techniques are well suited to address these limitations and are inherently capable of incorporating non-ideal carrier track, propagation effects, and nonstandard aperture sampling [19]. Time Domain Backprojection is one popular algorithm and is introduced next.

2.2.2   Time Domain Backprojection.   The second technique presented is time domain backprojection, simply called backprojection henceforth for brevity. Backprojection is based on tomography and is widely used in the medical sciences [29, 37]. Backprojection provides distinct advantages over FFT-based algorithms. First, backprojection is able to account for near-field spherical wavefront effects unlike many FFT-based algorithms which rely on the far-field plane wave approximation. Second, backprojection eliminates the two-dimensional interpolation required with FFT-based algorithms as shown in Section 2.2.1. Instead, backprojection requires one-dimensional time domain interpolation which is readily implemented using common signal processing techniques [42]. Finally, while PFA is primarily implemented using the LFM waveform, backprojection is generalized to arbitrary transmit waveforms. It is noted that the following development of time domain backprojection is similar, but not identical to, the convolution backprojection algorithm. The latter operates on data in the frequency domain and utilizes a ramp filter during the backprojection process [29].

The primary disadvantage of the backprojection algorithm is its computational complexity [51]. Each pulse return is processed individually, as opposed to the PFA which performs image reconstruction using the entire phase history in one step (after interpolation). Though the serial processing of pulse returns is initially a disadvantage, ironically it can be a benefit in the image formation process. With backprojection, range and cross-range processing are separable and image reconstruction can

commence immediately with the first pulse return before the entire phase history is acquired. This fact reduces transient storage requirements and computational power required for large IFFT's. Additionally, backprojection can take advantage of parallel computing whereby the phase history is divided among several processors, each forming an image with a subset of data, and combining the resulting interim products into a final image through a simple coherent summation. Recent works aim to improve backprojection performance including faster implementation methods [14, 57].

The backprojection algorithm performs range and cross-range processing independently. Thus, it is possible to produce a single image with only range information by performing pulse compression and backprojection with a single pulse return. Alternatively, iteratively performing backprojection for each radar location $\overline{\mathbf{R}}$ without fast-time processing produces an image with only cross-range content.

Image reconstruction begins by defining the imaging grid in the x-y plane. This image reconstruction grid defines points, or pixels, at which the estimated scene reflectivity $\hat{\rho}(\hat{\mathbf{r}}')$ is produced. Any point in this grid is specified by

$$\hat{\mathbf{r}}' = \hat{\mathbf{x}}\,\hat{x}' + \hat{\mathbf{y}}\,\hat{y}' \,. \tag{2.77}$$

The first step in backprojection is range processing through pulse compression. This step is often performed via fast-time matched filtering to maximize signal to noise ratio (SNR) and produce a one-dimensional range profile along the radar LOS [25]. Next, this range profile is backprojected onto the reconstruction grid to isolate the contribution from a hypothesized scatterer at each point $\hat{\mathbf{r}}'$ in the pulse return. Each gridpoint has corresponding round-trip time delay $\hat{\tau}'$ given by

$$
\begin{aligned}
\hat{\tau}' &= \frac{1}{\omega_o} 2\,\overline{\mathbf{k}}_o \cdot (\overline{\mathbf{r}}_o + \hat{\mathbf{r}}') \\
&= 2t_o + \frac{1}{\omega_o} 2\,\overline{\mathbf{k}}_o \cdot \hat{\mathbf{r}}' \\
&= 2t_o + \frac{2\,\hat{\mathbf{r}}_o \cdot \hat{\mathbf{r}}'}{c} \,,
\end{aligned}
\tag{2.78}
$$
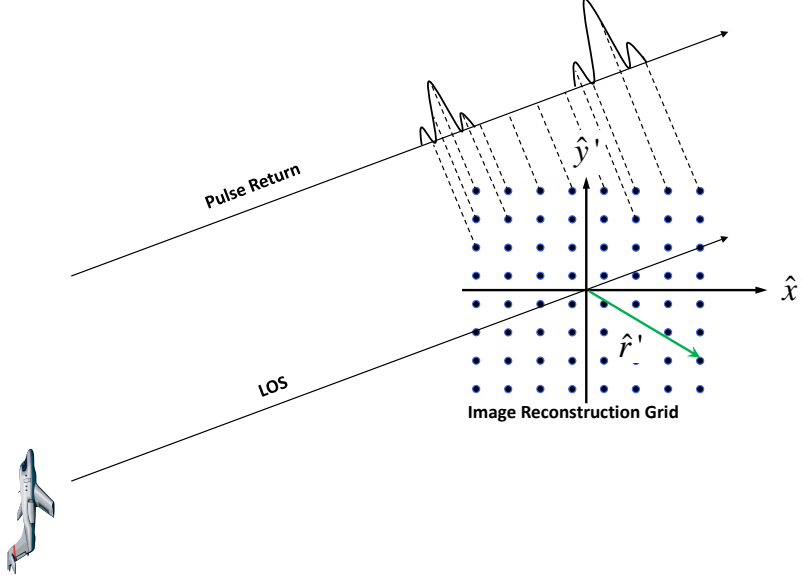
Figure 2.10: In backprojection the range profile is traced back to each individual reconstruction grid point to estimate the contribution from a scatterer at that point in the pulse return. The final grid values in the reconstructed image are obtained by coherently summing the backprojected response of all pulse returns.

where target specific time delay is referenced to scene center. The sample in the pulse return closest to $\hat{\tau}'$ is selected for backprojection to $\hat{\mathbf{r}}'$. Figure 2.10 illustrates the backprojection process for one pulse return.

Backprojection requires interpolation of complex time domain data given that the discrete pulse return time samples do not exactly coincide with $\hat{\tau}'$. If low order interpolation is used, high spatial frequency content is lost [44,51]. Ideal time domain interpolation is implemented by performing a FT on the compressed pulse, zero-padding in the frequency domain and then performing an IFT. This process produces an ideally upsampled signal and the closest point to $\hat{\tau}'$ is selected for backprojection. The amount of zero-padding presents a trade-off between interpolation accuracy and computational load.

As shown in Figure 2.10, each reconstruction grid point is mapped back to a time delay in the processed pulse return. This delay however also contains contributions from other points at the same slant range. When the delayed returns from a number of collection locations are integrated during iterative backprojection from

each point on the synthetic aperture, contributions from a scatterer at $\hat{\mathbf{r}}'$ add coherently, while returns from other points add incoherently. Thus, the backprojection process is repeated for all pixel locations and pulse returns. Image pixel values for each collection location are coherently integrated for all pulse returns to produce the estimated scene reflectivity $\hat{\rho}(\bar{\mathbf{r}}')$ as

$$\hat{\rho}(\bar{\mathbf{r}}') = \int_{\mathbf{R}} d\overline{\mathbf{R}} \; r\left(\hat{\tau}', \overline{\mathbf{R}}\right) \; . \tag{2.79}$$

The backprojection PSF is not readily defined by a single analytical formula as fast and slow-time processing are performed independently. It will be shown that range and cross-range resolutions are given by Equation (2.1) and Equation (2.3), respectively. These two components of image resolution are discussed next.

Formulation of the PSF depends on slow-time processing in backprojection, i.e., the integration of complex values for a given reconstruction grid point across the synthetic aperture. To begin, assume the scene consists of a single point scatterer at $\bar{\mathbf{r}}'$ with reflectivity $\rho_{\bar{\mathbf{r}}'}$. The pulse return for this point target from Equation (2.32) is

$$r\left(t, \bar{\mathbf{r}}', \bar{\mathbf{r}}_o\right) = \rho_{\bar{\mathbf{r}}'} \sqrt{P_r} \exp\left[j\omega_o\left(t - 2t_o\right)\right] \exp\left(-j2\,\bar{\mathbf{k}}_o \cdot \bar{\mathbf{r}}'\right) \; . \tag{2.80}$$

In Equation (2.80), amplitude $\sqrt{P_r}$ and phase $\exp\left[j\omega_o\left(t - 2t_o\right)\right]$ are known features of the pulse return and are removed by the receiver, reducing the pulse return to

$$r\left(t, \bar{\mathbf{r}}', \bar{\mathbf{r}}_o\right) = \rho_{\bar{\mathbf{r}}'} \exp\left(-j2\,\bar{\mathbf{k}}_o \cdot \bar{\mathbf{r}}'\right) \; , \tag{2.81}$$

where $\rho_{\bar{\mathbf{r}}'}$ is a single complex number representing the point target's reflectivity and

$$\begin{aligned}
2\,\bar{\mathbf{k}}_o \cdot \bar{\mathbf{r}}' &= 2\,k_o\left(\hat{\mathbf{x}}\kappa_x + \hat{\mathbf{y}}\kappa_y + \hat{\mathbf{z}}\kappa_z\right) \cdot \left(\hat{\mathbf{x}}\,x' + \hat{\mathbf{y}}\,y' + \hat{\mathbf{z}}\,z'\right) \\
&= 2\,k_o\left(x'\kappa_x + y'\kappa_y + z'\kappa_z\right) \; ,
\end{aligned} \tag{2.82}$$

is target phase referenced to scene center.

Each grid location $\hat{\mathbf{r}}'$ has associated phase, again referenced to scene center, given by the inner product in Equation (2.78)

$$2\,\bar{\mathbf{k}}_o \cdot \hat{\mathbf{r}}' = 2\,k_o\left(\hat{x}'\kappa_x + \hat{y}'\kappa_y\right) \ . \tag{2.83}$$

During the backprojection process the time correction in Equation (2.78) can also be presented as a phase correction, where this correction is the difference between Equation (2.82) and Equation (2.83)

$$2\,\bar{\mathbf{k}}_o \cdot (\bar{\mathbf{r}}' - \hat{\mathbf{r}}') \;=\; 2k_o\left[(x' - \hat{x}')\,\kappa_x + (y' - \hat{y}')\,\kappa_y + z'\kappa_z\right] \ . \tag{2.84}$$

The integration of these phase corrections across the synthetic aperture, i.e., for all θ_o, defines the PSF

$$
\begin{aligned}
\hat{\rho}\left(\bar{\mathbf{r}}'\right) \;&=\; \int_{\theta_o} d\theta_o \rho_{\bar{\mathbf{r}}'} \exp\left[-j2\bar{\mathbf{k}}_o \cdot (\bar{\mathbf{r}}' - \hat{\mathbf{r}}')\right] I\left(t, \hat{\tau}'\right) \\
&=\; \mathcal{L}^{-1}\left[r\left(t, \bar{\mathbf{r}}', \bar{\mathbf{r}}_o\right)\right] \ ,
\end{aligned}
\tag{2.85}
$$

where $I\left(t, \hat{\tau}'\right)$ is the required time domain interpolation. Equation (2.85) is expanded to show range and cross-range dependency as

$$\rho_{\bar{\mathbf{r}}'} \int_{\theta_o} d\theta_o \exp\left[-j2k_o\left(x' - \hat{x}'\right)\kappa_x\right] \exp\left[-j2k_o\left(y' - \hat{y}'\right)\kappa_y\right] \exp\left(-j2k_oz'\kappa_z\right) \ . \tag{2.86}$$

It was previously assumed that elevation angle ψ_o is constant through the CPI, i.e., across θ_o. With $\kappa_z = \sin\psi_o$, the third term in the integrant of Equation (2.86) only contributes a constant phase independent of both θ_o and pixel location $(\hat{x}', \hat{y}')$ and can be omitted. Equation (2.86) reduces to

$$\mathrm{PSF}\left(\hat{x}', \hat{y}'\right) = \rho_{\bar{\mathbf{r}}'} \int_{\theta_o} d\theta_o \exp\left[-j2k_o\left(x' - \hat{x}'\right)\kappa_x\right] \exp\left[-j2k_o\left(y' - \hat{y}'\right)\kappa_y\right] \ , \tag{2.87}$$

and describes the PSF as a function of reconstruction grid locations $\hat{x}'$ and $\hat{y}'$.

The range and cross-range PSFs are found by examining the respective principle cuts of the surface described by Equation (2.87). At the target range $x' = \hat{x}'$, Equation (2.87) is purely the cross-range PSF

$$\text{PSF}\,(\hat{y}')_{\text{cross}-\text{range}} = \rho_{\bar{\mathbf{r}}'} \int\limits_{\theta_o} d\theta_o \exp\left[-j2k_o\left(y' - \hat{y}'\right)\kappa_y\right] . \tag{2.88}$$

A change of variables is performed to transform Equation (2.88) from and integral over θ_o to an integral across pulses. As stated in Section 2.1.3 the radar transmits M pulses at equally spaced distance Δ_y across the synthetic aperture. For the moment assume a broadside spotlight imaging geometry as shown in Figure 2.1. The scene center in cross-range is $Y_c = 0$ and the $\mathbf{x}$ and $\hat{\mathbf{x}}'$ axes in Figure 2.5 are coincident. In this case, the cross-range collection location along the $\mathbf{y}$-axis for pulse m is given by

$$R_y = m\Delta_y \qquad m = -\frac{M}{2}, \ldots, \frac{M}{2} , \tag{2.89}$$

and from Equation (2.17), when $Y_c = 0$,

$$\sin\theta_o = \frac{-R_y}{r_o \cos\psi_o} = -\frac{m\Delta_y}{r_o \cos\psi_o} . \tag{2.90}$$

The Jacobian of the transformation is computed from

$$\begin{aligned} \cos\theta_o \, d\theta_o &= -\frac{\Delta_y}{r_o \cos\psi_o}dm \\ d\theta_o &= -\frac{\Delta_y}{r_o \cos\psi_o \cos\theta_o}dm \\ &= -\frac{\Delta_y}{X_c - R_x}dm , \end{aligned} \tag{2.91}$$

where Equation (2.17) is used in the final simplification.

Substituting Equation (2.90) and Equation (2.91) into Equation (2.88) enables the cross-range PSF to be restated as an integral across m. After inverting the limits

38

of integration to eliminate the negative in the Jacobian, the PSF is

$$
\rho_{\bar{\mathbf{r}}'} \frac{\Delta_y}{X_c - R_x} \int_{\frac{M}{2}}^{-\frac{M}{2}} dm \exp\left[-j2k_o\left(y' - \hat{y}'\right)\frac{m\Delta_y}{r_o}\right] , \tag{2.92}
$$

resulting in

$$
\rho_{\bar{\mathbf{r}}'} \frac{\Delta_y}{X_c - R_x} \left. \frac{\exp\left[-j2k_o\left(y' - \hat{y}'\right)\frac{m\Delta_y}{r_o}\right]}{\left[-j2k_o\left(y' - \hat{y}'\right)\frac{\Delta_y}{r_o}\right]} \right|_{\frac{M}{2}}^{-\frac{M}{2}} . \tag{2.93}
$$

Substituting in the limits of integration and simplifying using Euler's formula allows Equation (2.93) to be reduced to

$$
\begin{aligned}
\text{PSF}\left(\hat{y}'\right)_{\text{cross-range}} &= -\rho_{\bar{\mathbf{r}}'} \frac{M\Delta_y}{X_c - R_x} \frac{\sin\left[k_o\left(y' - \hat{y}'\right)\frac{M\Delta_y}{r_o}\right]}{\left[k_o\left(y' - \hat{y}'\right)\frac{M\Delta_y}{r_o}\right]} \\
&= -\rho_{\bar{\mathbf{r}}'} \frac{L}{R_c}\text{sinc}\left[k_o\left(y' - \hat{y}'\right)\frac{L}{r_o}\right] ,
\end{aligned} \tag{2.94}
$$

where $M\Delta_y = L$ is the synthetic aperture length from Equation (2.37) and $X_c - R_x = R_c$ is the ground range to scene center. From Figure 2.1 it is seen that

$$
\frac{L}{R_c} \approx \tan\left(\Delta\theta\right) \approx \Delta\theta , \tag{2.95}
$$

and

$$
\frac{L}{r_o} \approx \sin\left(\Delta\theta\right) \approx \Delta\theta , \tag{2.96}
$$

using the small angle approximations. The cross-range PSF is finally reduced to

$$
\text{PSF}\left(\hat{y}'\right)_{\text{cross-range}} = \left|\rho_{\bar{\mathbf{r}}'}\right| \Delta\theta \, \text{sinc}\left[k_o\left(y' - \hat{y}'\right)\Delta\theta\right] , \tag{2.97}
$$

where the negative sign is eliminated as pixel magnitude is shown in final image reconstruction.

39

Simply stated, given a scatterer at cross-range location y', Equation (2.97) provides final pixel magnitude as a function of reconstruction grid cross-range location $\hat{y}'$ where the maximum response is at $\hat{y}' = y'$. The cross-range resolution is found by locating the first nulls in PSF. These locations are found by equating the argument of the $\mathrm{sinc}\,(\cdot)$ function in Equation (2.97) to $\pm\pi$ and solving for $\hat{y}'$. Allowing $k_o = 2\pi/\lambda_o$ from Equation (2.24),

$$\frac{2\pi}{\lambda_o}\left(y' - \hat{y}'\right)\Delta\theta = \pm\pi$$
$$\hat{y}' = y' \pm \frac{\lambda_o}{2\Delta\theta}\;, \tag{2.98}$$

which agrees with cross-range resolution in Equation (2.3).

The derivation of the cross-range PSF assumed broadside spotlight SAR imaging. The approach is easily generalized for the forward or backward squint case by adjusting the values for index m in Equation (2.89) to appropriately define synthetic aperture collection locations R_y.

Setting $y' = \hat{y}'$ in Equation (2.87) yields the range PSF

$$\mathrm{PSF}\,(\hat{x}')_{\mathrm{range}} = \int\limits_{\theta_o} d\theta_o \rho_{\bar{\mathbf{r}}'} \exp\left[-j2k_o\left(x' - \hat{x}'\right)\kappa_x\right]\;. \tag{2.99}$$

With $\kappa_x = \cos\psi_o \cos\theta_o$, and
$$\cos\theta_o = \frac{X_c - R_x}{r_o \cos\psi_o}\;, \tag{2.100}$$

from Equation (2.17), Equation (2.99) reduces to

$$
\begin{aligned}
\mathrm{PSF}\,(\hat{x}')_{\mathrm{range}} &= \rho_{\bar{\mathbf{r}}'} \int\limits_{-\frac{\Delta\theta}{2}}^{\frac{\Delta\theta}{2}} d\theta_o \exp\left[-j2k_o\left(x' - \hat{x}'\right)\frac{X_c - R_x}{r_o}\right] \\
&= \rho_{\bar{\mathbf{r}}'}\Delta\theta \, \exp\left[-j2k_o\left(x' - \hat{x}'\right)\frac{X_c - R_x}{r_o}\right] \\
&= |\rho_{\bar{\mathbf{r}}'}|\,\Delta\theta\;,
\end{aligned}
\tag{2.101}
$$

Table 2.1: Parameters used for both an LFM and simple sinusoidal pulse for the imaging scenario in Figure 2.11.

Parameter	Value
Center Frequency	10 GHz
Bandwidth	900 MHz
$\Delta\theta$	5.2°
L	450 m
R_c	5 000 m
Theoretical δ_x	0.167 m
Theoretical δ_y	0.167 m

as only pixel magnitude is shown after image reconstruction. The integrand is independent of the variable of integration. Thus, Equation (2.101) integrates to a constant magnitude and the backprojection algorithm provides no range information.

As stated in the introduction to backprojection, pulse compression is the first step. The PSF envelope along the range axis is specific to transmit waveform and pulse compression techniques. The theory of pulse compression is a fundamental principle of radar processing and the well-known formula given by Equation (2.1) yields expected range resolution. Backprojection relies on this basic theory for fast-time processing and the specific pulse compression technique drives the range PSF.

An imaging scenario is now shown to compare the point spread functions of SAR imaging using the LFM waveform and a rectangular sinusoidal pulse when back-projection is used for image reconstruction. Center frequency and bandwidth are held constant between the two waveforms. The parameters in Table 2.1 and imaging geometry shown in Figure 2.11 define the collection scenario. The scene consists of 13 point targets with spacing shown, and collection parameters deliberately set to provide equal resolution in range and cross-range, $\delta_x = \delta_y = 0.167$ m. Ideally, the targets should appear as infetesimal points in the image reconstruction grid as shown in Figure 2.12. However, given the compact-support phase history, the ideal is not attainable in practice.
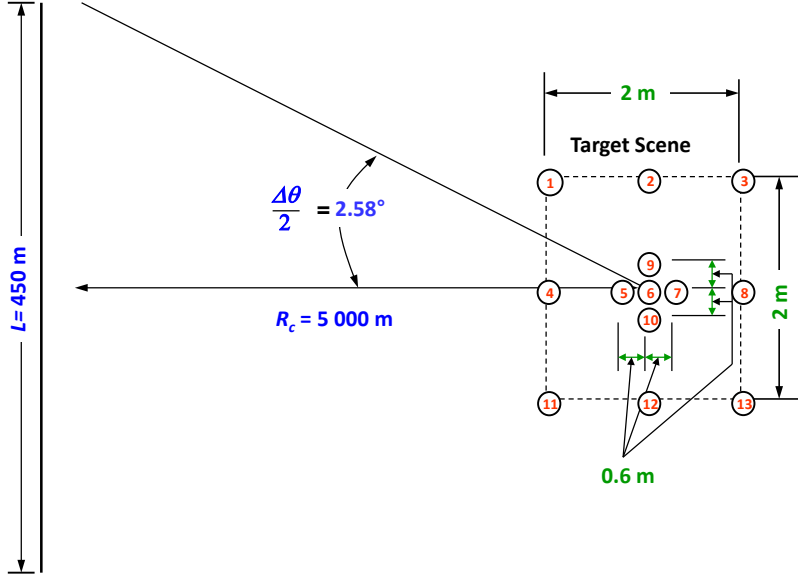
Figure 2.11: Imaging scenario used to compare the point spread functions of SAR imaging using the LFM waveform and a simple sinusoidal pulse when backprojection is used for image reconstruction. Collection parameters are deliberately set to provide equal resolution in range and cross-range of $\delta_x = \delta_y = 0.167$ m.
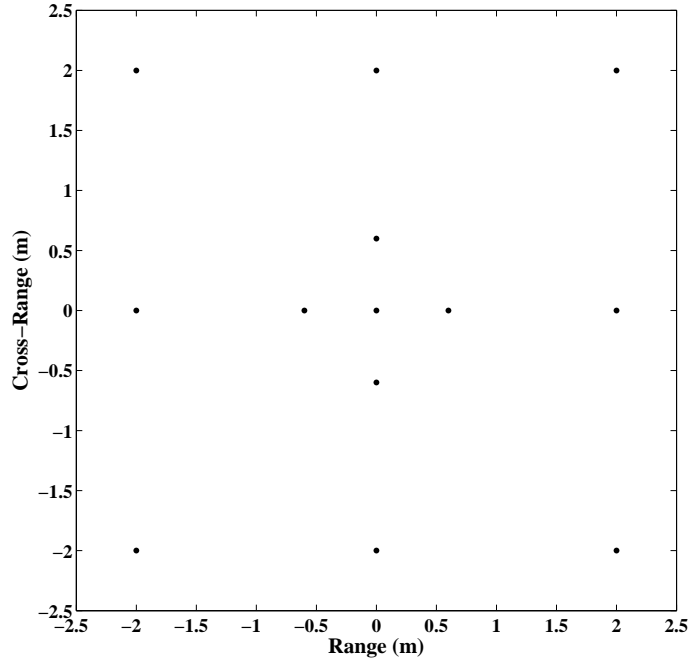
Figure 2.12: Under ideal conditions, the point targets should appear as infetesimal dots in the image reconstruction grid as shown. However, given the compact-support phase history, the ideal is not attainable in practice.
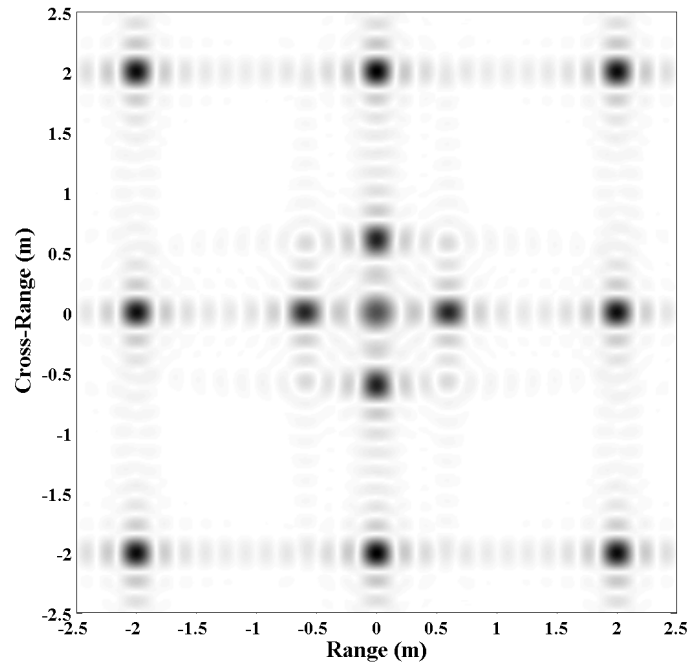
Figure 2.13: Reconstructed image of scene in Figure 2.11 with LFM collected data. Image resolutions compare favorably with the theoretical values.
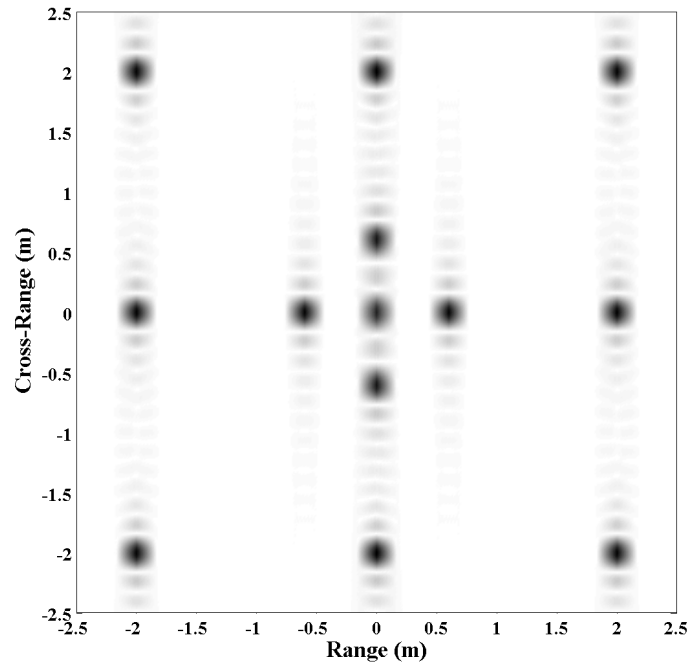
Figure 2.14: Reconstructed image of scene in Figure 2.11 with sinusoidal pulse collected data. Image resolutions compare favorably with the theoretical values.

Reconstructed SAR images using the LFM and sinusoid pulse are shown in Figures 2.13 and 2.14, respectively, where traditional matched filtering is used for pulse compression. Both figures show a focused SAR image. Range and cross-range cuts of the center target, Target #6 in Figure 2.11, for both collection scenarios are shown overlayed in Figures 2.15 and 2.16. The red dashed line in the figures corresponds to the LFM waveform while the blue solid corresponds to the sinusoidal pulse. As shown in Figure 2.15, the range PSF is driven by the shape of the match filtered pulse return. A simple rectangular pulse yields the familiar triangular shape while the LFM waveform yields the well-known $\text{sinc}(\cdot)$ envelope. However, the cross-range PSFs shown in Figure 2.16 are nearly identical regardless of transmit waveform. The $\text{sinc}(\cdot)$ shape agrees with the theoretical given in Equation (2.97).

2.3 Current Research Efforts

The SAR data collection and image reconstruction overview presented in this chapter assumes a single-channel system operating at a fixed center frequency. Recent breakthroughs in multi-channel technology [10] and new interest in the arena of waveform diversity offer exciting prospects for SAR applications. FDA SAR processing developed in the upcoming chapters exploit advances in these two fields to improve SAR image quality. This section summarizes related research in order to motivate the upcoming development.

Extending SAR operations from a single-channel to multi-channel operation offers many benefits including improved ambiguity suppression for MTI and imaging large swaths [18, 24], and improved SNR [58]. However, the majority of literature relating to multi-channel SAR benefits focuses on STAP and moving target indicator (MTI) processing of SAR data, with a representative set of theoretical and experimental given in [13, 17, 27, 56].

MTI is a basic mission performed by many radar systems. Implementation of MTI in airborne radar for detection of slow moving targets is complex as clutter
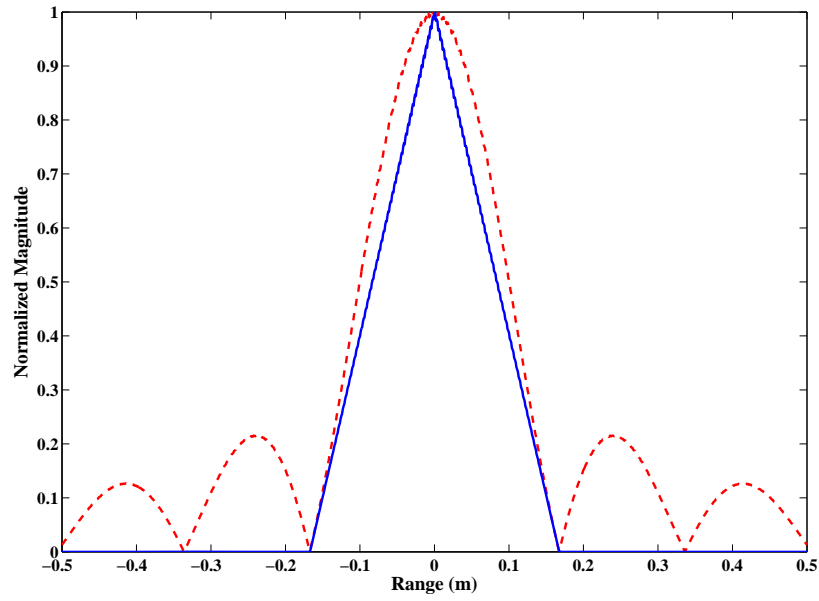
Figure 2.15: The range PSFs for the LFM (red dashed line) and rectangular sinusoidal pulse (blue solid line) are shown. A rectangular pulse produces the familiar triangular shape while the LFM waveform produces the well-known $\mathrm{sinc}\,(\cdot)$ envelope.
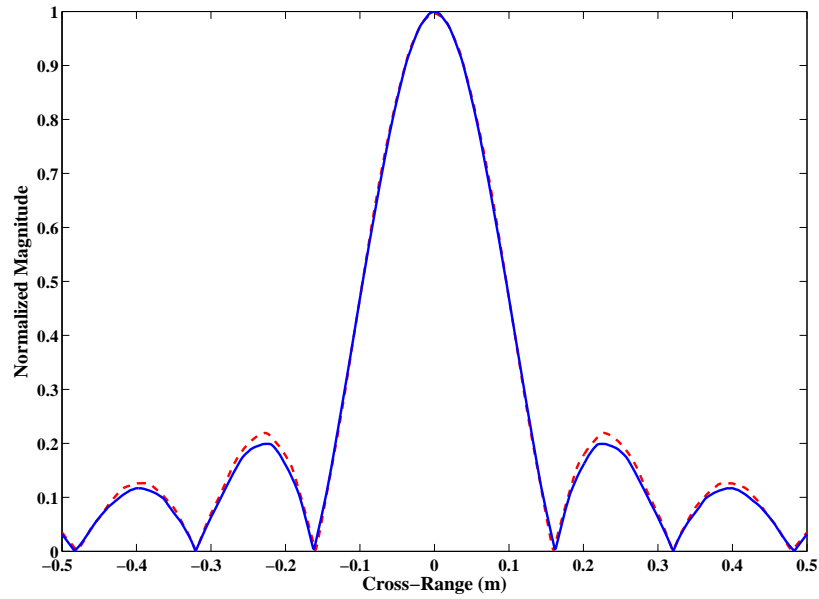
Figure 2.16: The cross-range PSFs for the LFM (red dashed line) and rectangular sinusoidal pulse (blue solid line) are shown. The cross-range PSF is independent of transmit waveform, and the $\mathrm{sinc}\,(\cdot)$ shape agrees with the theoretical given in Equation (2.97).

Doppler spectrum masks the target signal [17]. In traditional airborne MTI, this problem is alleviated with a narrower transmit beam. However, as noted in Section 2.1.1, a narrow beam degrades stripmap SAR image quality and would also limit the MTI surveillance area. Additionally, a single-channel system MTI performs well with targets with a high radar reflectivity and/or those moving at a speed sufficient to highlight their returns from the clutter band.

The MTI detection probability is increased by use of a multi-channel system, particularly through the use of STAP or displaced phase center antenna (DPCA). STAP involves a two-dimensional filtering technique that exploits the relationship between the spatial and temporal domains to improve clutter rejection [30] and enhance MTI performance. Alternatively, with DPCA the forward motion of the moving antenna is compensated for by shifting the effective radiation center of the antenna backward, so that over a few pulses the antenna is effectively stationary in space. The clutter Doppler spectrum is greatly reduced, enhancing detection of slow moving targets [35]. The research presented in this document aims to apply multi-channel operation to enhance SAR imaging. This application has not garnered as much attention in recent literature, though there are many potential contributions.

Extending SAR operations to multi-channel operation is a physical change to radar hardware. A parallel extension exists in the signal processing system. SAR has traditionally used common phase coded waveforms for imaging. The recent emergence of waveform diversity offers new potential to radar operations. The importance of waveform diversity has been highlighted by senior U.S. Air Force leaders [55] as a growing and vital part of future operational capabilities. Innovative concepts like multi-dimensional waveform encoding [31] ushers in a new generation of SAR systems with both improved performance and flexible imaging capabilities. A single system can provide multiple capabilities like InSAR, MTI, and hybrid SAR imaging modes that were previously out of reach.

Waveform diversity applications extend beyond radar applications. In fact, it is the commercial communications industry that has led the charge in maturing these new technologies [55]. Given the generality of waveform diversity, the research presented in this document relates specifically to frequency diversity in SAR operations. Frequency diversity (FD) can be applied to SAR applications in one of two approaches. First, FD may be applied across the synthetic aperture baseline by varying center frequency from collection point to collection point. Alternatively, FD can be applied simultaneously at each collection point in the SAR via use of a multi-channel system.

The most common application of frequency diversity in SAR imaging found in literature is the synthetic bandwidth approach [9,34,40,47]. Range resolution is a function of bandwidth per Equation (2.1), with superior SAR range resolution achieved using higher bandwidths. However, certain factors restrict system bandwidth. The achievable maximum bandwidth is often dictated by hardware constraints and cannot be changed. Additionally, increased bandwidth leads to a proportional increase in thermal noise power introduced by the receiver and poses additional challenges in wideband antenna design.

Synthetic bandwidth is an FFT-based technique where center frequency is varied across the synthetic aperture. The spectral content in the deramped pulse in Equation (2.53) is given by Equation (2.56), where center frequency and bandwidth dictate the spatial frequencies obtained. The use of multiple center frequencies along the synthetic aperture yields greater spectral information as compared to a single carrier system. Figure 2.17 illustrates this approach for two center frequencies ω_1 and ω_2. Setting

$$\omega_2 = \omega_1 + 2\pi B_{LFM} \, , \tag{2.102}$$

enables recovery of adjacent, non-overlapping regions in the spatial frequency domain. Effective system bandwidth is twice the actual bandwidth, as clearly seen by comparing Figure 2.17 and Figure 2.9, and resulting range resolution improved by a factor of two. Although, the synthetic bandwidth approach is well studied and experimentally
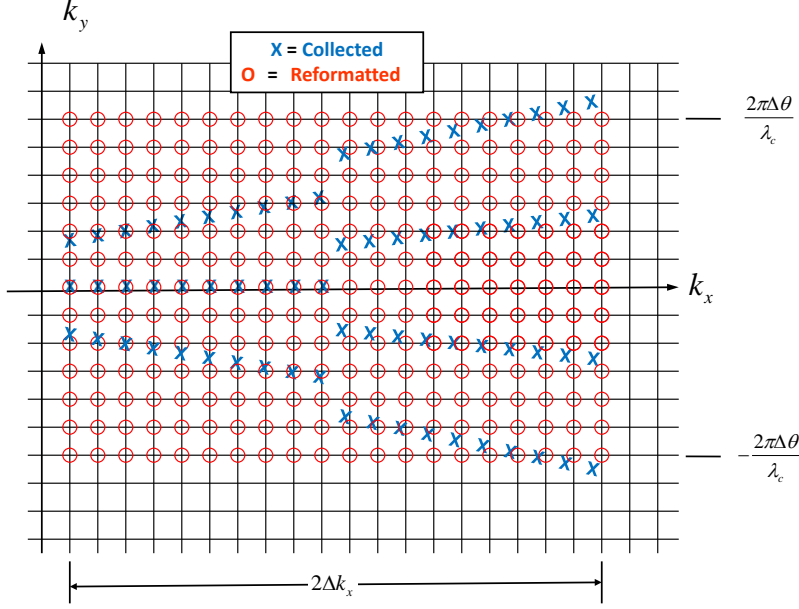
Figure 2.17: The use of multiple carrier frequencies along the synthetic aperture yields greater spectral information as compared to a single carrier system. The two center frequencies enables recovery of adjacent, non-overlapping regions in the spatial frequency domain. Interpolation to the red O grid points yields approximately the same information as a single carrier system with twice the bandwidth.

validated, it focuses on only one dimension of image resolution. The spectral content in the cross-range dimension is unchanged, and this technique provides no benefit in cross-range resolution. FDA SAR processing studied during this research emphasizes resolution improvement in the cross-range dimension and offers a unique application to frequency diversity techniques.

New antenna technologies allow a second application of frequency diversity. The authors in [2–4] demonstrate the ability to form range-dependent beam patterns by operating radiating elements across the physical antenna array at different frequencies. These frequency diverse arrays (FDA) are a novel concept and allow FD to be applied simultaneously at each collection point on the SAR baseline. The limited research in this area is restricted to a one-dimensional FDA pattern analysis and verification [28, 48] and application to STAP/GMTI [6]. Given the importance of waveform diversity and benefits offered by multi-channel systems, the FDA SAR research presented combines the two capabilities for the first time to enhance SAR

cross-range resolution. FDA analysis has been performed under current research at the Air Force Institute of Technology (AFIT) as an innovative approach in radar applications.

III. Frequency Diverse Array Development

The development in Chapter II assumed a single channel system and antenna patterns were only superficially discussed in Section 2.1.1. Many early and current SAR systems utilize a single channel parabolic dish antenna. More recently, the trend has been to transition to active phased array antennas [1, 11, 19].

Phased array antennas offer many benefits including agile beam steering, higher power on target, and increased reliability. Phased array radars have seen breakthroughs leading to capabilities not possible only a few years ago. Developments in radar hardware allow miniaturization on scales not previously seen causing active electronically scanned arrays (AESA) to be lighter in weight, smaller volume, higher reliability and lower cost [10]. Advancements in computing power allow radar hardware to actively control the many transmit/receive modules in an AESA and process and store the sheer volume of data collected.

Many existing and proposed SAR system currently or plan to utilize phased array antennas. Antenna patters from AESAs are well understood [8] and complex antenna response is accounted for in SAR processing [44]. A newer concept in antenna theory is the frequency diverse array (FDA) [2, 4]. The characteristics of a FDA were previously introduced and analyzed in [2, 4, 48], however the FDA pattern was only completely analyzed for a 1-D linear array.

This chapter extends previous work to develop the FDA pattern for a 2-D planar array with frequency progression in both dimensions. The antenna pattern of a waveform diverse planar array is first presented. Each channel may transmit a unique waveform to include channel specific amplitude modulation, operating frequency, and phase modulation. As the more general case, this model applies to a traditional phased array antenna where each channel operates at the same center frequency and beam steering is achieved with a linear phase progression across channels. This baseline allows direct comparison of to the FDA pattern, where a linear frequency progression exists across the channels.
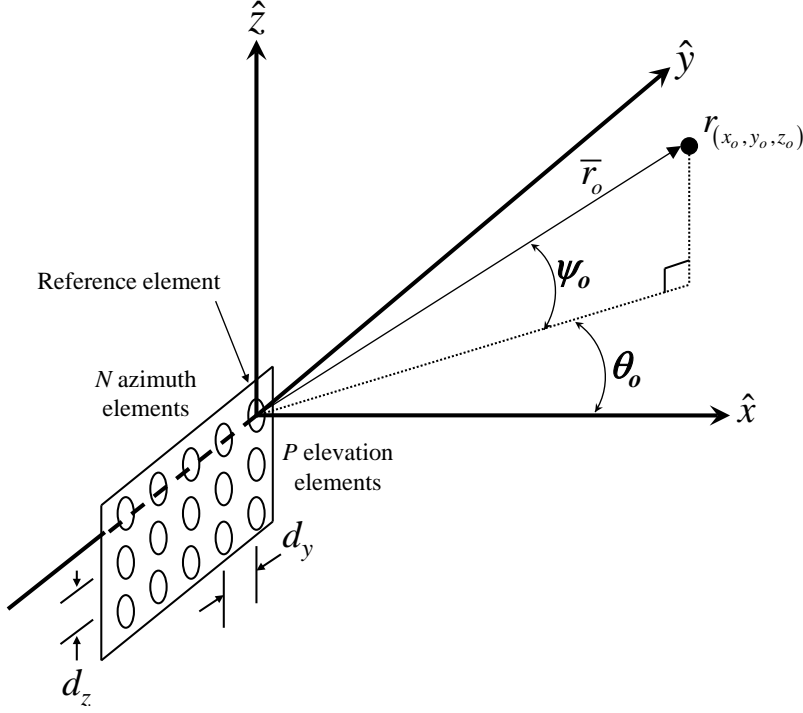
Figure 3.1: Radar-centric coordinate system for the planar array case. The array is located in the $\hat{\mathbf{y}}$-$\hat{\mathbf{z}}$ plane with the coordinate system of Figure 2.4 centered on the reference element [25].

3.1 Planar Array Coordinate System

The geometric basis for the signal model development is depicted in Figure 3.1 for a planar array [25, 46, 53]. This figure extends the radar-centric coordinate system in Figure 2.4, Section 2.1.2, from a single channel to a multi-channel system. The array consists of P rows of N-element linear arrays located in the $\hat{\mathbf{y}}$-$\hat{\mathbf{z}}$ plane. The linear arrays are oriented along $\hat{\mathbf{y}}$ and stacked along $\hat{\mathbf{z}}$. Inter-element spacing in azimuth is d_y while spacing in elevation is d_z. The elements are assumed to be isotropic radiators in this development. Additionally, the development assumes ideal radiators with no inter-element coupling between antenna elements. These assumptions are common in SAR literature. The coordinate system of Figure 2.4 is centered on a reference element. By convention, this reference element is defined to be the first element to receive a pulse return signal from a target at positive elevation and positive azimuth.
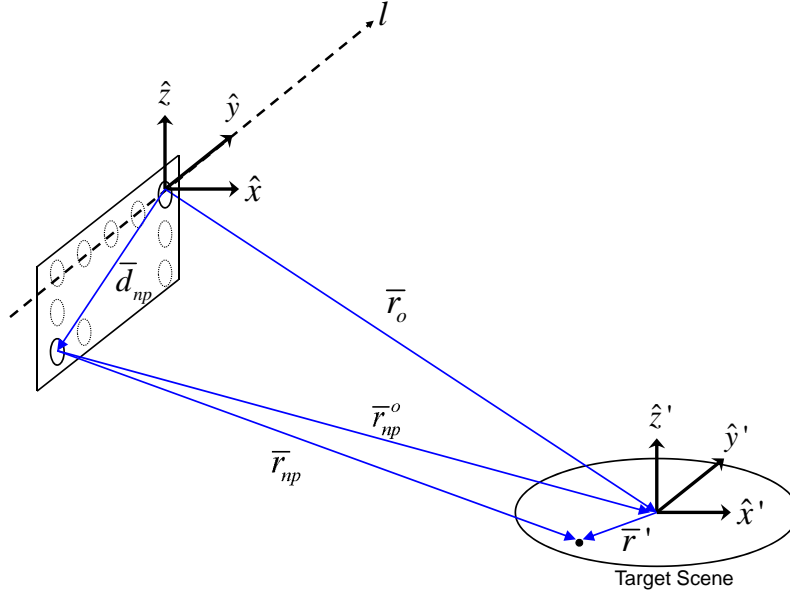
Figure 3.2: Radar coordinates in spotlight mode SAR operation. The radar maintains focus on a finite target area. Vectors $\bar{\mathbf{d}}_{np}$, $\bar{\mathbf{r}}_{\mathbf{o}}$, and $\bar{\mathbf{r}}'$ are used to define the locations of the np^{th} element, scene center, and point r' respectively.

The pulse return from such a target to the remaining elements is therefore delayed with respect to the reference element.

Figure 3.2 illustrates the radar coordinate system for an airborne SAR operating in spotlight mode. This figure extends of Figure 2.5 to portray the planar array antenna case. The reference point r_o in Equation (2.5) is again chosen to be target scene center. The dashed line l depicts the flight path while $\bar{\mathbf{r}}'$ defines an arbitrary point r' in the scene in target-centric coordinates. The location of the np^{th} element is given by $\bar{\mathbf{d}}_{np}$ in radar centric coordinates

$$\bar{\mathbf{d}}_{np} = -\hat{\mathbf{y}} n d_y - \hat{\mathbf{z}} p d_z, \qquad n = 0, \ldots, N-1, \quad p = 0, \ldots, P-1 . \qquad (3.1)$$

Equation (2.5) and Equation (3.1) can be combined to form $\bar{\mathbf{r}}_{np}^o$ from the np^{th} element to scene center. After inverting the direction of $\bar{\mathbf{d}}_{np}$ to point from the np^{th}

52

element to the reference element, $\bar{\mathbf{r}}_{np}^o$ is

$$\bar{\mathbf{r}}_{np}^o = \bar{\mathbf{r}}_o - \bar{\mathbf{d}}_{np} \ . \tag{3.2}$$

Finally, $\bar{\mathbf{r}}_{np}$ describes the location of point r' with respect to the np^{th} element

$$\begin{aligned} \bar{\mathbf{r}}_{np} &= \bar{\mathbf{r}}_{np}^o + \bar{\mathbf{r}}' \\ &= \bar{\mathbf{r}}_o - \bar{\mathbf{d}}_{np} + \bar{\mathbf{r}}' \ . \end{aligned} \tag{3.3}$$

3.2   Planar Array Pattern Development

In general, the np^{th} channel transmit waveform $s_{np}(t)$ is given in complex envelope notation by

$$s_{np}(t) = a_{np}(t) \exp \left\{ j \left[\omega_{np} t + \phi_{np}(t) \right] \right\} \ , \tag{3.4}$$

where $a_{np}(t)$ is a function of time defining the amplitude of $s_{np}(t)$, $\omega_{np} = 2\pi f_{np}$ is the angular frequency, and $\phi_{np}(t)$ is a function of time defining any phase modulation. A CW signal is assumed for this discussion making $\phi_{np}(t) = \phi_o = 0$ for convenience. For practical reasons $a_{np}(t)$ is either a square wave or constant. The normalized transmitted radar signal from the np^{th} element is then simply

$$s_{np}(t) = \exp(j\omega_{np}t) \ . \tag{3.5}$$

After transmission by the antenna, the signal propagates as

$$s_{np}\left(t, \bar{\mathbf{k}}\right) = \exp \left[j \left(\omega_{np} t - \bar{\mathbf{k}}_{np} \cdot \bar{\mathbf{r}}_{np} \right) \right] \ , \tag{3.6}$$

where $\bar{\mathbf{k}}_{np}$ is the wavevector and denotes the radar line-of-sight to the reference path

$$\bar{\mathbf{k}}_{np} = k_{np} \hat{\mathbf{r}}_{np}^o \ , \tag{3.7}$$

53

and the magnitude of this vector is the wavenumber

$$k_{np} = \frac{\omega_{np}}{c} \ .$$ (3.8)

In traditional array theory, the far-field approximation assumes

$$\bar{\mathbf{k}}_{np} = k_{np}\hat{\mathbf{r}}_o \ ,$$ (3.9)

where $\hat{\mathbf{r}}_o$ is given by Equation (2.8). With this approximation the signal s_{Tnp} received at point r' due to the np^{th} channel using Equation (3.3) is

$$
\begin{aligned}
s_{Tnp}\left(t, \bar{\mathbf{r}}', \bar{\mathbf{r}}_o\right) &= \exp\left[j\left(\omega_{np}t - \bar{\mathbf{k}}_{np} \cdot \bar{\mathbf{r}}_{np}\right)\right] \\
&= \exp\left\{j\left[\omega_{np}t - \bar{\mathbf{k}}_{np} \cdot \left(\bar{\mathbf{r}}_o - \bar{\mathbf{d}}_{np} + \bar{\mathbf{r}}'\right)\right]\right\} \\
&= \exp\left\{j\left[\omega_{np}\left(t - \frac{r_o}{c}\right) + \bar{\mathbf{k}}_{np} \cdot \bar{\mathbf{d}}_{np} - \bar{\mathbf{k}}_{np} \cdot \bar{\mathbf{r}}'\right]\right\} \\
&= \exp\left\{j\left[\omega_{np}\left(t - t_o\right) + \bar{\mathbf{k}}_{np} \cdot \bar{\mathbf{d}}_{np} - \bar{\mathbf{k}}_{np} \cdot \bar{\mathbf{r}}'\right]\right\} \ .
\end{aligned}
$$ (3.10)

Each phase component potentially contributes a Doppler component in addition to the time delay t_o in Equation (3.10).

To identify array contributions to range and Doppler induced effects, the array factor is expressed as a superposition of all channels. The oscillatory behavior of the signal components results in constructive and destructive interference of the electric fields in the far-field forming the overall radiation pattern given by

$$
\begin{aligned}
s_T\left(t, \bar{\mathbf{r}}', \bar{\mathbf{r}}_o\right) &= \sum_{n=0}^{N-1}\sum_{p=0}^{P-1} s_{Tnp}\left(t, \bar{\mathbf{r}}', \bar{\mathbf{r}}_o\right) \\
&= \sum_{n=0}^{N-1}\sum_{p=0}^{P-1} \exp\left\{j\left[\omega_{np}\left(t - t_o\right) + \bar{\mathbf{k}}_{np} \cdot \bar{\mathbf{d}}_{np} - \bar{\mathbf{k}}_{np} \cdot \bar{\mathbf{r}}'\right]\right\} \\
&= \sum_{n=0}^{N-1}\sum_{p=0}^{P-1} \exp\left[j\omega_{np}\left(t - t_o\right)\right] \\
&\qquad\qquad \times \exp\left(j\bar{\mathbf{k}}_{np} \cdot \bar{\mathbf{d}}_{np}\right)\exp\left(-j\bar{\mathbf{k}}_{np} \cdot \bar{\mathbf{r}}'\right) \ .
\end{aligned}
$$ (3.11)

The formulation of Equation (3.11) accounts for arbitrary assignment of channel frequencies and is the most general case of a FDA. To develop antenna patterns used for SAR imaging, two specific planar array modalities are considered next. The first case is the constant frequency array (CFA) where all channels operate at the same center frequency. This modality is the standard by which most AESAs operate today. Next, a specific case of the general FDA is considered. All channel frequencies are related to the reference channel via a linear horizontal and/or vertical frequency progression.

3.3 Constant Frequency Array (CFA)

This section develops the antenna pattern for a traditional CFA. The CFA is defined here as one in which all channels operate at the same center frequency. Beam steering is achieved by applying a linear phase progression across the aperture. With no phase progression, the antenna beam points to broadside. However, a linear phase progression causes the radiated electric fields to constructively sum in the far-field in a direction off broadside resulting in an electronic scan.

With all channels operating at the same angular frequency, i.e., $\omega_{np} = \omega_o$ for all n, p, k_{np} in Equation (3.8) is replaced by k_o where

$$k_o = \frac{\omega_o}{c} \ , \tag{3.12}$$

and $\bar{\mathbf{k}}_{np}$ in Equation (3.9) reduces to

$$\bar{\mathbf{k}}_o = k_o \hat{\mathbf{r}}_o \ . \tag{3.13}$$

Substituting Equation (3.12) and Equation (3.13) into Equation (3.11) yields

$$
\begin{aligned}
s_T\left(t, \bar{\mathbf{r}}', \bar{\mathbf{r}}_o\right)_{CFA} &= \sum_{n=0}^{N-1} \sum_{p=0}^{P-1} \exp\left[j\omega_o\left(t - t_o\right)\right] \exp\left(j\bar{\mathbf{k}}_o \cdot \bar{\mathbf{d}}_{np}\right) \exp\left(-j\bar{\mathbf{k}}_o \cdot \bar{\mathbf{r}}'\right) \\
&= \exp\left[j\omega_o\left(t - t_o\right)\right] \exp\left(-jk_o\hat{\mathbf{r}}_o \cdot \bar{\mathbf{r}}'\right) \sum_{n=0}^{N-1} \sum_{p=0}^{P-1} \exp\left(jk_o\hat{\mathbf{r}}_o \cdot \bar{\mathbf{d}}_{np}\right) \\
&= g\left(t, \bar{\mathbf{r}}', \bar{\mathbf{r}}_o\right) f\left(t, \hat{\mathbf{r}}_o\right)_{CFA} .
\end{aligned}
\tag{3.14}
$$

In Equation (3.14) $g\left(t, \bar{\mathbf{r}}', \bar{\mathbf{r}}_o\right)$ is

$$
g\left(t, \bar{\mathbf{r}}', \bar{\mathbf{r}}_o\right) = \exp\left[j\omega_o\left(t - t_o\right)\right] \exp\left(-jk_o\hat{\mathbf{r}}_o \cdot \bar{\mathbf{r}}'\right) ,
\tag{3.15}
$$

and the array factor $f\left(t, \hat{\mathbf{r}}_o\right)_{CFA}$ for a CFA is

$$
f\left(t, \hat{\mathbf{r}}_o\right)_{CFA} = \sum_{n=0}^{N-1} \sum_{p=0}^{P-1} \exp\left(jk_o\hat{\mathbf{r}}_o \cdot \bar{\mathbf{d}}_{np}\right) .
\tag{3.16}
$$

It is customary to omit the time-dependency in the array factor as the antenna is usually treated as stationary. The dependency is retained to emphasize the synthetic aperture's dependence on time.

Derivation of the array factor begins with expansion of the inner product in Equation (3.16)

$$
\begin{aligned}
\hat{\mathbf{r}}_o \cdot \bar{\mathbf{d}}_{np} &= \left(\hat{\mathbf{x}}\kappa_x + \hat{\mathbf{y}}\kappa_y + \hat{\mathbf{z}}\kappa_z\right) \cdot \left(-\hat{\mathbf{y}}nd_y - \hat{\mathbf{z}}pd_z\right) \\
&= -nd_y\kappa_y - pd_z\kappa_z ,
\end{aligned}
\tag{3.17}
$$

where κ_x, κ_y, and κ_z were given in Equation (2.7). The expansion in Equation (3.17) enables Equation (3.16) to be separable in n and p

$$
f\left(t, \hat{\mathbf{r}}_o\right)_{CFA} = \left[\sum_{n=0}^{N-1} \exp\left(-jk_o nd_y\kappa_y\right)\right] \left[\sum_{p=0}^{P-1} \exp\left(-jk_o pd_z\kappa_z\right)\right] .
\tag{3.18}
$$

The partial sum of a geometric series for finite B

$$\sum_{b=0}^{B} a^b = \frac{1 - a^{B+1}}{1 - a} \, , \qquad a \neq 1 \tag{3.19}$$

yields a closed-form solution to each summation in Equation (3.18)

$$f\left(t, \hat{\mathbf{r}}_o\right)_{CFA} = \frac{1 - \exp\left(-jk_o N d_y \kappa_y\right)}{1 - \exp\left(-jk_o d_y \kappa_y\right)} \frac{1 - \exp\left(-jk_o P d_z \kappa_z\right)}{1 - \exp\left(-jk_o d_z \kappa_z\right)} \, , \tag{3.20}$$

when $k_o d_y \kappa_y \neq 2\pi u$ and $k_o d_z \kappa_z \neq 2\pi v$ for integer u, v. The first fraction in Equation (3.20) can be further simplified to be

$$
\begin{aligned}
& \frac{1 - \exp\left(-jk_o N d_y \kappa_y\right)}{1 - \exp\left(-jk_o d_y \kappa_y\right)} \\
= \; & \frac{\exp\left(-jk_o \frac{N}{2} d_y \kappa_y\right)}{\exp\left(-jk_o \frac{1}{2} d_y \kappa_y\right)} \frac{\left[\exp\left(jk_o \frac{N}{2} d_y \kappa_y\right) - \exp\left(-jk_o \frac{N}{2} d_y \kappa_y\right)\right]}{\left[\exp\left(jk_o \frac{1}{2} d_y \kappa_y\right) - \exp\left(-jk_o \frac{1}{2} d_y \kappa_y\right)\right]} \\
= \; & \exp\left[-jk_o\left(\frac{N-1}{2}\right) d_y \kappa_y\right] \frac{\sin\left(k_o \frac{N}{2} d_y \kappa_y\right)}{\sin\left(k_o \frac{1}{2} d_y \kappa_y\right)} \, .
\end{aligned}
\tag{3.21}
$$

Euler's formula is used in the final simplification. Similarly, the second fraction in Equation (3.20) can be shown to simplify to

$$\frac{1 - \exp\left(-jk_o P d_z \kappa_z\right)}{1 - \exp\left(-jk_o d_z \kappa_z\right)} = \exp\left[-jk_o\left(\frac{P-1}{2}\right) d_z \kappa_z\right] \frac{\sin\left(k_o \frac{P}{2} d_z \kappa_z\right)}{\sin\left(k_o \frac{1}{2} d_z \kappa_z\right)} \, . \tag{3.22}$$

Combining Equation (3.21) and Equation (3.22) yields the well-known digital $\operatorname{sinc}(\cdot)$ pattern for a CFA [8]

$$f\left(t, \hat{\mathbf{r}}_o\right)_{CFA} = \exp\left[j\left(\phi_{CFA_y} + \phi_{CFA_z}\right)\right] \frac{\sin\left(k_o \frac{N}{2} d_y \kappa_y\right)}{\sin\left(k_o \frac{1}{2} d_y \kappa_y\right)} \frac{\sin\left(k_o \frac{P}{2} d_z \kappa_z\right)}{\sin\left(k_o \frac{1}{2} d_z \kappa_z\right)} \, , \tag{3.23}$$

where

$$\phi_{CFA_y} = -k_o \left(\frac{N-1}{2} \right) d_y \kappa_y ,$$

$$\phi_{CFA_z} = -k_o \left(\frac{P-1}{2} \right) d_z \kappa_z . \tag{3.24}$$

The composite signal from a CFA at a position $\bar{\mathbf{r}}'$ relative to $\bar{\mathbf{r}}_o$ is given by Equation (3.14) using Equation (3.15) and Equation (3.23).

The power pattern $W(\psi_o, \theta_o)_{CFA}$ is the magnitude squared of Equation (3.23)

$$W(\psi_o, \theta_o)_{CFA} = \left| \frac{\sin\left(k_o \frac{N}{2} d_y \kappa_y\right)}{\sin\left(k_o \frac{1}{2} d_y \kappa_y\right)} \frac{\sin\left(k_o \frac{P}{2} d_z \kappa_z\right)}{\sin\left(k_o \frac{1}{2} d_z \kappa_z\right)} \right|^2 . \tag{3.25}$$

It is clear that the pattern in Equation (3.25) is solely a function of azimuth and elevation implicit in κ_y and κ_z from Equation (2.7). For a stationary radar, the power pattern is independent of both range and time.

In Equation (3.25), the maximum field having the amplitude of $|NP|^2$ is achieved in the limit when

$$\frac{1}{2} k_o d_y \kappa_y = \pi u, \qquad u = 0, \pm 1, \pm 2, \dots , \tag{3.26}$$

and

$$\frac{1}{2} k_o d_z \kappa_z = \pi v, \qquad v = 0, \pm 1, \pm 2, \dots . \tag{3.27}$$

In this case Equation (3.25) equates in the limit to

$$W(\psi_o, \theta_o)_{CFA} = \left| \frac{\sin(N\pi u)}{\sin(\pi u)} \frac{\sin(P\pi v)}{\sin(\pi v)} \right|^2 , \qquad u, v = 0, \pm 1, \pm 2, \dots$$

$$= |NP|^2 . \tag{3.28}$$

via use of L'Hospital's rule. Substituting κ_z from Equation (2.7) into Equation (3.27) yields the maximum at elevation

$$\psi_{max} = \arcsin\left(\frac{2\pi v}{k_o d_z} \right) . \tag{3.29}$$

Table 3.1: CFA parameters used to produce the antenna pattern shown in Figure 3.3 to Figure 3.5.

Parameter	Value
Number Azimuth Elements (N)	9
Number Elevation Elements (P)	9
Operating Frequency ($\omega_o = 2\pi f_o$)	$2\pi(10 \text{ GHz})$
Azimuth Elemental Spacing (d_y)	$\lambda_o/2 = 0.015$ m
Elevation Elemental Spacing (d_z)	$\lambda_o/2 = 0.015$ m

Substituting κ_y from Equation (2.7) and ψ_{max} from Equation (3.29) into Equation (3.26) yields the maximum at azimuth

$$\theta_{max} = \arcsin\left(\frac{2\pi u}{k_o d_y \cos \psi_{max}}\right) . \tag{3.30}$$

For purposes of illustration, the CFA power patterns are shown in Figure 3.3 to Figure 3.5 using the parameters in Table 3.1. Using these parameters in Equation (3.29) and Equation (3.30) and observing for this scenario both arcsin terms are only defined for the $u, v = 0$ case, the peak pattern response is found to occur at $\psi_{max} = 0°$, $\theta_{max} = 0°$. Figure 3.3 shows a cross-section of the CFA power pattern cut along the y-z plane of Figure 3.1. The pattern's dependence on azimuth and elevation is evident. Figure 3.4 and Figure 3.5 illustrate the principal azimuth and elevation plane cuts of the same power pattern. The principal azimuth plane is the x-z plane along $\theta = 0°$. The principal elevation plane is the x-y plane along $\psi = 0°$. In these cases, for a given ψ or θ the pattern does not change as a function of range.

3.4 Frequency Diverse Array (FDA)

Having developed the antenna pattern for a CFA, focus now turns to a frequency diverse array (FDA) where all channels do not necessarily operate at the same center frequency. In general, an FDA may have an arbitrary assignment of channel frequencies. Different schemes can be used to assign these frequencies depending on the radar's intended purpose.
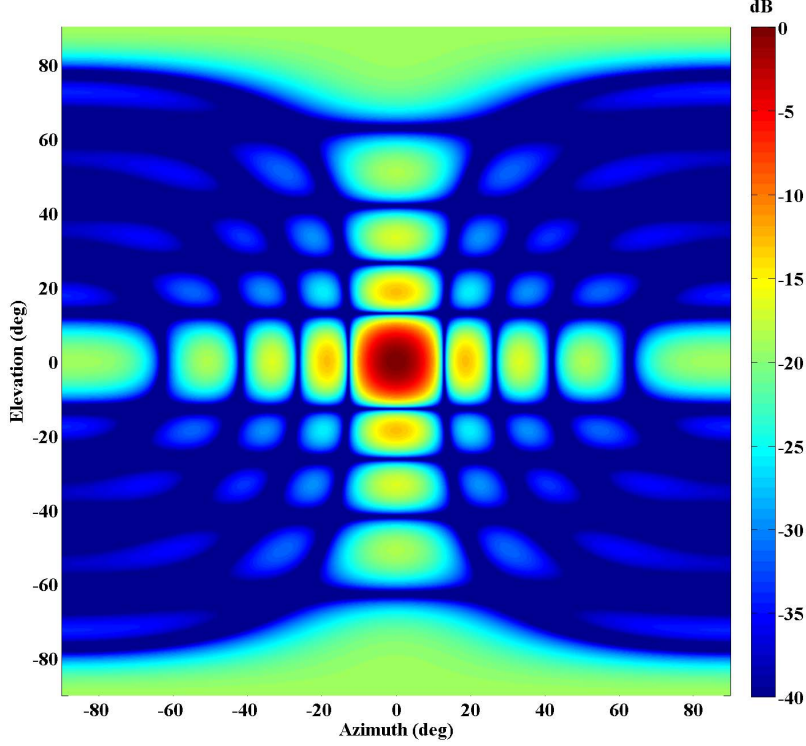
Figure 3.3: Cross-section of CFA power pattern for a 9×9 array cut along the y-z plane. The pattern's dependence on azimuth and elevation is evident.

FDA SAR processing takes advantage of the unique waveform properties obtained when a linear frequency progression is applied across the planar array. These characteristics were previously introduced and analyzed in $[2, 4, 48]$ and showed potential for applications in SAR imaging $[20\text{--}22]$. Under this mode of operation, the antenna continuously scans in range, azimuth, and elevation without the use of phase shifters. The scanning is solely attributed to the progressive frequency shift between antenna channels. Through the remainder of this document, the term FDA is used to denote the general FDA in the specific case of channel frequency assignment based on linear frequency progression.

Previously in $[4, 5, 48]$ the FDA pattern was only completely analyzed for an $N \times 1$ 1-D linear array. Additionally, in $[5]$ a linear FDA is applied to the radar STAP GMTI problem and in $[3]$ other applications are proposed, though the time varying nature of the pattern is not addressed in either. This chapter considers an $N \times P$

60
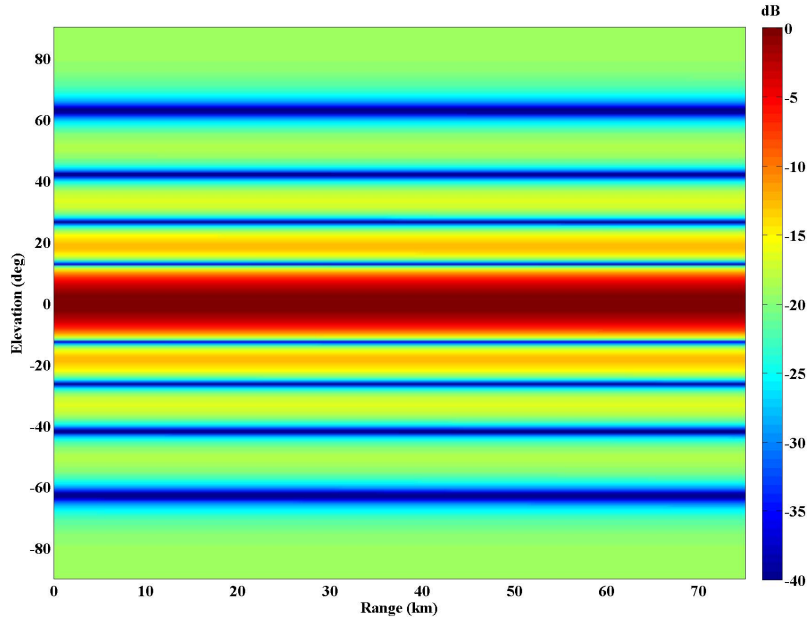
Figure 3.4: Cross-section of CFA power pattern for a 9×9 array in the principal azimuth plane. For a given elevation angle, the CFA pattern does not change as a function of range.
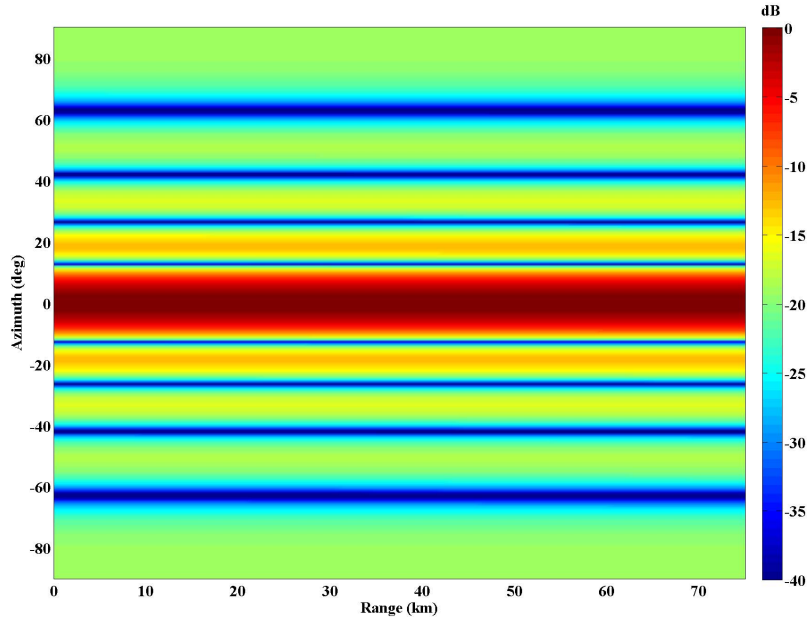
Figure 3.5: Cross-section of CFA power pattern for a 9×9 array in the principal elevation plane. For a given azimuth angle, the CFA pattern does not change as a function of range.

2-D planar array with frequency progression along both dimensions and identifies the conditions under which the resultant analytical patterns are valid.

3.4.1 FDA Frequency Progression. The FDA pattern derivation follows the procedure used for CFA radars in Section 3.3. The distance from each channel to a point in the target scene is broken up into the distance from the reference element to that point, and an incremental path length difference between the reference element and all other array channels. With the linear frequency progression constraint, the reference element is set to some base frequency ω_o. Next, a linear incremental frequency progression $\Delta\omega_y$ is inserted horizontally across the array while a linear incremental frequency progression $\Delta\omega_z$ is inserted vertically. Thus, ω_{np} is the operating frequency of channel np given by

$$\omega_{np} = \omega_o + n\Delta\omega_y + p\Delta\omega_z, \qquad n = 0, \ldots, N-1, \quad p = 0, \ldots, P-1 . \qquad (3.31)$$

The quantities $\Delta\omega_y$ and $\Delta\omega_z$ can either be either positive or negative. As expected this selection effects antenna pattern and waveform properties and these effects are exploited in the FDA SAR processing.

The FDA is conceptually similar to a stepped-frequency waveform whereby a group of M monochromatic pulses are transmitted sequentially in time. The first pulse has frequency ω_o and subsequent pulse each have a an incremental frequency progression of $\Delta\omega$ [53]. The frequency of pulse m is then

$$\omega_m = \omega_o + m\Delta\omega, \qquad m = 0, \ldots, M-1 . \qquad (3.32)$$

Alternatively, frequency within a single pulse is stepped during equal subsections, or chips, of the total pulse width. In either case, the difference between stepped-frequency waveform and FDA is that in the first case the frequency progression is applied temporally while in the latter it is applied spatially.

Development of the FDA pattern begins with the radiation pattern of a generic planar array given in Equation (3.11). With frequency diversity, the channel-dependent wavenumber in Equation (3.8) and wavevector in Equation (3.9) are

$$
\begin{aligned}
k_{np} &= \frac{\omega_{np}}{c} \\
&= \frac{\omega_o + n\Delta\omega_y + p\Delta\omega_z}{c} \\
&= k_o + n\Delta k_y + p\Delta k_z \ ,
\end{aligned}
\tag{3.33}
$$

and

$$
\begin{aligned}
\bar{\mathbf{k}}_{np} &= k_{np}\hat{\mathbf{r}}_o \\
&= \left(k_o + n\Delta k_y + p\Delta k_z\right)\hat{\mathbf{r}}_o \ ,
\end{aligned}
\tag{3.34}
$$

where Δk_y and Δk_z are $\Delta\omega_y/c$ and $\Delta\omega_z/c$ respectively. The composite signal received at $\bar{\mathbf{r}}'$ was given in Equation (3.11) and is repeated here for convenience

$$
\begin{aligned}
s_T\left(t,\bar{\mathbf{r}}',\bar{\mathbf{r}}_o\right) &= \sum_{n=0}^{N-1}\sum_{p=0}^{P-1}\exp\left[j\omega_{np}\left(t - t_o\right)\right] \\
&\qquad\times \exp\left(j\bar{\mathbf{k}}_{np}\cdot\bar{\mathbf{d}}_{np}\right)\exp\left(-j\bar{\mathbf{k}}_{np}\cdot\bar{\mathbf{r}}'\right) \ .
\end{aligned}
\tag{3.35}
$$

In the following simplification of Equation (3.35) for the FDA case, only the phase terms are shown for clarity. The product of the three complex exponentials gives a resultant angle of

$$
\arg\left[s_T\left(t,\bar{\mathbf{r}}',\bar{\mathbf{r}}_o\right)_{FDA}\right] = \omega_{np}\left(t - t_o\right) + \bar{\mathbf{k}}_{np}\cdot\bar{\mathbf{d}}_{np} - \bar{\mathbf{k}}_{np}\cdot\bar{\mathbf{r}}' \ .
\tag{3.36}
$$

Substituting Equation (3.17) and Equation (3.31) to Equation (3.34) into Equation (3.36) gives

$$
\begin{aligned}
& \omega_{np}\left(t-t_{o}\right)+\bar{\mathbf{k}}_{np} \cdot \bar{\mathbf{d}}_{np}-\bar{\mathbf{k}}_{np} \cdot \bar{\mathbf{r}}' \\
= \ & \left(\omega_{o}+n\Delta\omega_{y}+p\Delta\omega_{z}\right)\left(t-t_{o}\right)+\left(k_{o}+n\Delta k_{y}+p\Delta k_{z}\right)\hat{\mathbf{r}}_{o} \cdot \bar{\mathbf{d}}_{np} \\
& -\left(k_{o}+n\Delta k_{y}+p\Delta k_{z}\right)\hat{\mathbf{r}}_{o} \cdot \bar{\mathbf{r}}' \\
= \ & \left(\omega_{o}+n\Delta\omega_{y}+p\Delta\omega_{z}\right)\left(t-t_{o}\right) \\
& +\left(k_{o}+n\Delta k_{y}+p\Delta k_{z}\right)\left(-nd_{y}\kappa_{y}-pd_{z}\kappa_{z}\right) \\
& -\left(k_{o}+n\Delta k_{y}+p\Delta k_{z}\right)\hat{\mathbf{r}}_{o} \cdot \bar{\mathbf{r}}' \\
= \ & \omega_{o}\left(t-t_{o}\right)-k_{o}\hat{\mathbf{r}}_{o} \cdot \bar{\mathbf{r}}' \\
& +n\Delta\omega_{y}\left(t-t_{o}\right)-nk_{o}d_{y}\kappa_{y}-n\Delta k_{y}\hat{\mathbf{r}}_{o} \cdot \bar{\mathbf{r}}' \\
& +p\Delta\omega_{z}\left(t-t_{o}\right)-pk_{o}d_{z}\kappa_{z}-p\Delta k_{z}\hat{\mathbf{r}}_{o} \cdot \bar{\mathbf{r}}' \\
& -n^{2}\Delta k_{y}d_{y}\kappa_{y}-np\Delta k_{y}d_{z}\kappa_{z} \\
& -p^{2}\Delta k_{z}d_{z}\kappa_{z}-pn\Delta k_{z}d_{y}\kappa_{y} \ .
\end{aligned}
\tag{3.37}
$$

The goal of this development is to derive a closed-form solution for the FDA power pattern similar to that derived for the CFA in Equation (3.25). The fact that all the CFA pattern phase terms were both linear and separable in n and p in Equation (3.18), enabled use of Equation (3.19) to arrive at a closed-form solution. This is not the case for the last four terms in Equation (3.37), two of which are quadratic and two are not separable in n and p and no further simplifications are possible.

It is possible to define specific conditions under which phase contributions form these terms are negligible allowing formulation of a closed-form solution. To this end, a physical description of each phase term in Equation (3.37) is now given. The channel frequency relationship given in Equation (3.31) enables the total phase accrual of a signal transmitted by any channel propagated to scene center to be referenced to ω_{o}.

64

Considering only an $N \times 1$ horizontal linear array, the cumulative phase accrual from the nth element operating at frequency ω_n to far-field target can be broken down into four components. First, the overall path length from the nth element to the target is composed of the path length from the nth element to the reference element and the path length from the reference element to the target. Second, given that $\omega_n = \omega_o + n\Delta\omega_y$, cumulative phase accrual over each of the two distances is given in terms of phase due to ω_o plus phase due to $n\Delta\omega_y$. The four components that contribute cumulative phase accrual are then:

- $\omega_o (t - t_o)$ is the cumulative phase accrual over the path length from the reference element to scene center due to base frequency ω_o.

- $n\Delta\omega_y (t - t_o)$ is the additional phase accrual over the path length from the reference element to scene center attributed to the incremental horizontal frequency progression.

- $nk_o d_y \kappa_y$ is the cumulative phase accrual over the path length from the reference element to the nth channel due to base frequency ω_o.

- $n^2 \Delta k_y d_y \kappa_y$ is the additional phase accrual over the path length from the reference element to the nth channel attributed to the incremental horizontal frequency progression.

Phase contributions from this last term is one of the four that should be bounded in order to simplify Equation (3.37).

Next, a $1 \times P$ vertical linear array is considered. The cumulative phase accrual from the pth element operating at a frequency ω_p to a far-field target can be broken down into four components as above. First, the overall path length from the pth element to the target is composed of the path length from the pth element to the reference element and the path length from the reference element to the target. Second, given that $\omega_p = \omega_o + p\Delta\omega_z$, cumulative phase accrual over each of the two distances is given in terms of phase due to ω_o plus phase due to $p\Delta\omega_z$. The four components that contribute cumulative phase accrual are then:

- $\omega_o (t - t_o)$ is the cumulative phase accrual over the path length from the reference element to scene center due to base frequency ω_o as above.

- $p \Delta \omega_z (t - t_o)$ is the additional phase accrual over the path length from the reference element to scene center attributed to the incremental vertical frequency progression.

- $p k_o d_z \kappa_z$ is the cumulative phase accrual over the path length from the reference element to the pth channel due to base frequency ω_o.

- $p^2 \Delta k_z d_z \kappa_z$ is the additional phase accrual over the path length from the reference element the pth channel attributed to the incremental vertical frequency progression.

Phase contributions from this last term is the second of four that should be bounded in order to simplify Equation (3.37).

Consideration now turns to an $N \times P$ planar array. Having accounted for phase due to frequency progression in each dimension individually, focus now turns to what effect frequency progression in one dimension has on the other. The cross-terms that give phase accrual due to frequency diversity over the path length from the reference element to the np^{th} are:

- $pn \Delta k_z d_y \kappa_y$ accounts for the additional phase accrual horizontally across the array due to the vertical frequency progression.

- $np \Delta k_y d_z \kappa_z$ accounts for the additional phase accrual vertically down the array due to the horizontal frequency progression.

Phase contributions from these two terms are the last of four that should be bounded in order to simplify Equation (3.37). In Equation (3.37), the three remaining terms $k_o \hat{\mathbf{r}}_o \cdot \bar{\mathbf{r}}'$, $n \Delta k_y \hat{\mathbf{r}}_o \cdot \bar{\mathbf{r}}'$, and $p \Delta k_z \hat{\mathbf{r}}_o \cdot \bar{\mathbf{r}}'$ account for the additional phase accrual for observation point r'. Focus now turns to the quadratic and nonseparable terms that should be bounded.

The transmitted signal from each channel is a simple sinusoid as shown in Equation (3.5). Two sinusoids of the same frequency interfere perfectly constructively when the relative phase between them is an even multiple of π and interfere perfectly destructively when the relative phase is an odd multiple of π. If the phase contributions from the quadratic terms were limited to a negligible value, these terms could be omitted in further analysis.

As a general rule, uncompensated quadratic phase contributions of less than $\pm\pi/4$ are acceptable [12, 29]. Within this limit, the transmitted signal from the reference element and the np^{th} channel still interfere constructively. Thus, quadratic phase terms can be neglected when their cumulative phase contributions meet the criteria

$$n^2 \Delta k_y d_y \kappa_y + np \Delta k_y d_z \kappa_z + p^2 \Delta k_z d_z \kappa_z + pn \Delta k_z d_y \kappa_y < \pm\frac{\pi}{4} \ . \qquad (3.38)$$

The phase error in Equation (3.38) is most severe at channel $(N-1), (P-1)$, i.e., the channel furthest from the reference element. Considering the NP^{th} channel yields a more conservative restriction and simplifies analysis. With this consideration, Equation (3.38) becomes

$$N^2 \Delta k_y d_y \kappa_y + NP \Delta k_y d_z \kappa_z + P^2 \Delta k_z d_z \kappa_z + PN \Delta k_z d_y \kappa_y < \pm\frac{\pi}{4} \ . \qquad (3.39)$$

In Equation (3.39) no restrictions are placed on the values of κ_y and κ_z, and therefore on θ or ψ, as typical radars scan a wide extent in azimuth and elevation. This consideration is next incorporated. Both κ_y and κ_z from Equation (2.7) are individually maximized to a value of ± 1. However, it is noted that κ_z is maximum at $\psi_o = \pm\pi/2$, at which point $\kappa_y = 0$. Additionally, κ_y is maximized at $\psi_o = 0, \theta_o = \pm\pi/2$ at which point $\kappa_z = 0$. Assuming both κ_y and κ_z can simultaneously achieve their maximum value $(\kappa_y = \kappa_z = 1)$ provides the most conservative restriction

$$N^2 \Delta k_y d_y + NP \Delta k_y d_z + P^2 \Delta k_z d_z + PN \Delta k_z d_y < \pm\frac{\pi}{4} \ . \qquad (3.40)$$

67

For set elemental spacing d_y and d_z, the restriction in Equation (3.40) limits the array size and/or frequency progression allowed across the physical aperture under which the remaining derivation is valid.

With the assumption the restriction in Equation (3.40) holds, the quadratic phase terms are negligible and Equation (3.37) reduces to

$$
\omega_o \left(t - t_o \right) - k_o \hat{\mathbf{r}}_o \cdot \bar{\mathbf{r}}'
$$
$$
+ n \Delta \omega_y \left(t - t_o \right) - n k_o d_y \kappa_y - n \Delta k_y \hat{\mathbf{r}}_o \cdot \bar{\mathbf{r}}'
$$
$$
+ p \Delta \omega_z \left(t - t_o \right) - p k_o d_z \kappa_z - p \Delta k_z \hat{\mathbf{r}}_o \cdot \bar{\mathbf{r}}' \ , \tag{3.41}
$$

and Equation (3.35) is separable in n and p

$$
\begin{aligned}
s_T \left(t, \bar{\mathbf{r}}', \bar{\mathbf{r}}_o \right)_{FDA} &= \exp \left[j \omega_o \left(t - t_o \right) \right] \exp \left(-j k_o \hat{\mathbf{r}}_o \cdot \bar{\mathbf{r}}' \right) \\
&\times \sum_{n=0}^{N-1} \exp \left\{ jn \left[\Delta \omega_y \left(t - t_o \right) - k_o d_y \kappa_y - \Delta k_y \hat{\mathbf{r}}_o \cdot \bar{\mathbf{r}}' \right] \right\} \\
&\times \sum_{p=0}^{P-1} \exp \left\{ jp \left[\Delta \omega_z \left(t - t_o \right) - k_o d_z \kappa_z - \Delta k_z \hat{\mathbf{r}}_o \cdot \bar{\mathbf{r}}' \right] \right\} \\
&= g \left(t, \bar{\mathbf{r}}', \bar{\mathbf{r}}_o \right) f \left(t, \bar{\mathbf{r}}', \bar{\mathbf{r}}_o \right)_{FDA} \ , \tag{3.42}
\end{aligned}
$$

where $g \left(t, \bar{\mathbf{r}}', \bar{\mathbf{r}}_o \right)$ is the same as the CFA case in Equation (3.15). The array factor $f \left(t, \bar{\mathbf{r}}', \bar{\mathbf{r}}_o \right)_{FDA}$ for a FDA is

$$
\begin{aligned}
f \left(t, \bar{\mathbf{r}}', \bar{\mathbf{r}}_o \right)_{FDA} &= \sum_{n=0}^{N-1} \exp \left\{ jn \left[\Delta \omega_y \left(t - t_o \right) - k_o d_y \kappa_y - \Delta k_y \hat{\mathbf{r}}_o \cdot \bar{\mathbf{r}}' \right] \right\} \\
&\times \sum_{p=0}^{P-1} \exp \left\{ jp \left[\Delta \omega_z \left(t - t_o \right) - k_o d_z \kappa_z - \Delta k_z \hat{\mathbf{r}}_o \cdot \bar{\mathbf{r}}' \right] \right\} \\
&= \sum_{n=0}^{N-1} \exp \left(jn\Theta \right) \sum_{p=0}^{P-1} \exp \left(jp\Psi \right) \ , \tag{3.43}
\end{aligned}
$$

where

$$
\Theta \left(t, \bar{\mathbf{r}}', \bar{\mathbf{r}}_o \right) = \Delta \omega_y \left(t - t_o \right) - k_o d_y \kappa_y - \Delta k_y \hat{\mathbf{r}}_o \cdot \bar{\mathbf{r}}' \ , \tag{3.44}
$$

68

and

$$\Psi\left(t, \bar{\mathbf{r}}', \bar{\mathbf{r}}_o\right) = \Delta\omega_z\left(t - t_o\right) - k_o d_z \kappa_z - \Delta k_z \hat{\mathbf{r}}_o \cdot \bar{\mathbf{r}}' . \tag{3.45}$$

Having reduced the FDA array factor to the same form as Equation (3.18), the derivation in Equation (3.19) to Equation (3.23) is used to simplify Equation (3.43) to

$$f\left(t, \bar{\mathbf{r}}', \bar{\mathbf{r}}_o\right)_{FDA} = \exp\left[j\left(\phi_{FDA_y} + \phi_{FDA_z}\right)\right] \frac{\sin\left(\frac{N}{2}\Theta\right)\sin\left(\frac{P}{2}\Psi\right)}{\sin\left(\frac{1}{2}\Theta\right)\sin\left(\frac{1}{2}\Psi\right)} , \tag{3.46}$$

where

$$\phi_{FDA_y} = \left(\frac{N-1}{2}\right)\Theta ,$$

$$\phi_{FDA_z} = \left(\frac{P-1}{2}\right)\Psi . \tag{3.47}$$

The FDA power pattern is the magnitude of Equation (3.46) squared

$$W\left(\psi_o, \theta_o, t, \bar{\mathbf{r}}', \bar{\mathbf{r}}_o\right)_{FDA} = \left|\frac{\sin\left(\frac{N}{2}\Theta\right)\sin\left(\frac{P}{2}\Psi\right)}{\sin\left(\frac{1}{2}\Theta\right)\sin\left(\frac{1}{2}\Psi\right)}\right|^2 . \tag{3.48}$$

Unlike Equation (3.25) in the CFA case, the FDA pattern in Equation (3.48) is no longer solely a function of azimuth and elevation. Due to the time-dependency in Equations (3.44) and (3.45), the power pattern for the FDA can only be fully specified for a given instant in time. Additionally, as will be shown in Section 3.4.2, the FDA beam sweeps across all θ, ψ as a function of time and that this scanning does not change as a function of array size, i.e., N and P.

An analytic model and constraints to describe the FDA antenna beam has now been established. Next, the dynamic nature is analyzed in order to better understand how an FDA illuminates the environment.

3.4.2 FDA Pattern Analysis. The authors in [48] present a general analysis of a linear FDA showing a periodic modulated pattern in range, angle, and time. This section expands the analysis for a planar FDA.

As in the case for the CFA in Equation (3.25), the maximum field in Equation (3.48) having the amplitude of $|NP|^2$ is achieved when

$$\frac{1}{2}\Theta = \pi u$$
$$\frac{1}{2}\left[\Delta\omega_y\left(t - t_o\right) - k_o d_y \kappa_y - \Delta k_y \hat{\mathbf{r}}_o \cdot \bar{\mathbf{r}}'\right] = \pi u, \qquad u = 0, \pm 1, \dots, \qquad (3.49)$$

and

$$\frac{1}{2}\Psi = \pi v$$
$$\frac{1}{2}\left[\Delta\omega_z\left(t - t_o\right) - k_o d_z \kappa_z - \Delta k_z \hat{\mathbf{r}}_o \cdot \bar{\mathbf{r}}'\right] = \pi v, \qquad v = 0, \pm 1, \dots, \qquad (3.50)$$

are simultaneously satisfied. Recalling range r is inherent in propagation time t_o and ψ, θ are inherent in κ_y, κ_z, the conditions in Equation (3.49) and Equation (3.50) reveal that at a fixed time infinitely many unique (r, ψ, θ) triplets exist to satisfy the conditions above. Similarly, at a fixed range infinitely many unique (t, ψ, θ) triplets exist where Equation (3.48) reaches to its maximum.

Setting $\bar{\mathbf{r}}' = 0$ for generality, and solving both Equations (3.49) and (3.50) for time t yields

$$\begin{aligned} t &= \frac{2\pi}{\Delta\omega_y}u + \frac{k_o d_y \kappa_y}{\Delta\omega_y} + t_o \\ &= \frac{1}{\Delta f_y}u + \frac{k_o d_y \kappa_y}{\Delta\omega_y} + t_o, \end{aligned} \qquad (3.51)$$

and similarly

$$t = \frac{1}{\Delta f_z}v + \frac{k_o d_z \kappa_z}{\Delta\omega_z} + t_o. \qquad (3.52)$$

Both Equations (3.51) and (3.52) show the periodicity of the antenna patten in time. For a fixed location in range, azimuth angle, and elevation angle the horizontal frequency progression causes that location to be illuminated with a period of $1/\Delta f_y$. Similarly, the vertical frequency progression causes the point to be illuminated with a

70

Table 3.2: FDA parameters used to produce the array pattern shown in Figure 3.6 to Figure 3.9.

Parameter	Value
Number Azimuth Elements (N)	9
Number Elevation Elements (P)	9
Base Operating Frequency ($\omega_o = 2\pi f_o$)	$2\pi(10 \text{ GHz})$
Azimuth Elemental Spacing (d_y)	$\lambda_o/2 = 0.015 \text{ m}$
Elevation Elemental Spacing (d_z)	$\lambda_o/2 = 0.015 \text{ m}$
Azimuth Frequency Progression ($\Delta\omega_y = 2\pi\Delta f_y$)	$2\pi(1.5 \text{ kHz})$
Elevation Frequency Progression ($\Delta\omega_z = 2\pi\Delta f_z$)	$2\pi(-1 \text{ kHz})$

period of $1/\Delta f_z$. Therefore, the maximum power on the point will occur in time when the two scanning periods coincide, i.e., when Equation (3.51) and Equation (3.52) are true simultaneously. Both scan periods are dependent only on frequency progression and not on individual channel frequencies.

Additionally, Equation (3.49) and Equation (3.50) can be used to find the location(s) in azimuth and elevation where the antenna pattern is at peak power when time and range are held constant. Substituting κ_z from Equation (2.7) into Equation (3.50), with $\bar{\mathbf{r}}' = 0$, yields the maximum at elevation ψ_{max} where

$$\frac{1}{2}\left[\Delta\omega_z\left(t - t_o\right) - k_o d_z \sin\psi_{max}\right] = \pi v$$

$$\psi_{max} = \sin^{-1}\left[\frac{\Delta\omega_z\left(t - t_o\right) - 2\pi v}{k_o d_z}\right] . \tag{3.53}$$

It is straightforward to show that substituting κ_z from Equation (2.7) and ψ_{max} from Equation (3.53) into Equation (3.49) yields the maximum at azimuth θ_{max} where

$$\frac{1}{2}\left[\Delta\omega_y\left(t - t_o\right) - k_o d_y \cos\psi_{max}\sin\theta_{max}\right] = \pi u$$

$$\theta_{max} = \sin^{-1}\left[\frac{\Delta\omega_y\left(t - t_o\right) - 2\pi u}{k_o d_y \cos\psi_{max}}\right] . \tag{3.54}$$

The power pattern for an FDA is shown in Figure 3.6 to Figure 3.9 using the parameters in Table 3.2. Figure 3.6 shows a cross-section of the power pattern for the

FDA cut along the y-z plane of Figure 3.1 at time $t = 0\,\mathrm{sec}$. At this time instant the antenna is steered to $\psi = 0°, \theta = 0°$ and is identical to the CFA pattern in Figure 3.3. The pattern's dependence on azimuth and elevation is evident. Figure 3.7 shows the same cross-section at $t = 250\,\mu\mathrm{sec}$. While the pattern is still dependent upon azimuth and elevation, the time dependency introduced by the frequency progression caused an electronic scan to $\psi = 30°, \theta = -60°$, and can be shown to agree with Equation (3.53) and Equation (3.54).

Figure 3.8 and Figure 3.9 illustrate the power pattern at $t = 0\,\mathrm{sec}$ along the principal azimuth and elevation planes respectively. In both cases, the patterns are no longer independent of range as in the CFA case. The negative vertical frequency progression $\Delta\omega_z$ in Table 3.2 causes the pattern to scan toward positive elevation as seen in Figure 3.8. Similarly, the positive horizontal frequency progression $\Delta\omega_y$ in Table 3.2 causes the pattern to scan toward negative azimuth as seen in Figure 3.9. Additionally these figures show that the greater the frequency progression, the more drastic change in pattern with range.

3.4.3 FDA Pattern Verification. It is important to verify the analytical FDA model developed as it forms the basis for FDA SAR processing. The following verification is performed both analytically and empirically. It will be shown that the FDA pattern reverts to a CFA pattern when frequency progression across both dimensions is removed. Additionally, the planar FDA pattern reverts to the linear FDA pattern previously presented in [48] when the number of elevation channels is $P = 1$. Finally, results from a high fidelity EM software simulation are used to empirically verify the models.

The array factors for the CFA and FDA are given in Equation (3.23) and Equation (3.46), respectively. The limiting case of an FDA with no frequency progressing is the CFA. With $\Delta\omega_y = \Delta\omega_z = 0$ (and therefore $\Delta k_y = \Delta k_z = 0$), Equation (3.46) should reduce to Equation (3.23). The phase terms in Equation (3.47) reduce to
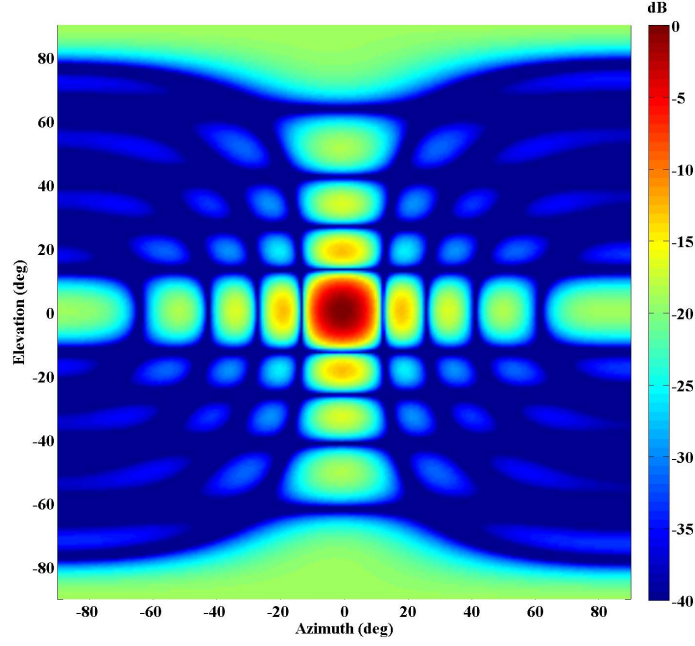
Figure 3.6: Cross-section of FDA power pattern for a 9×9 array cut along the y-z plane at $t = 0 \sec$. The pattern's dependence on azimuth and elevation is evident.
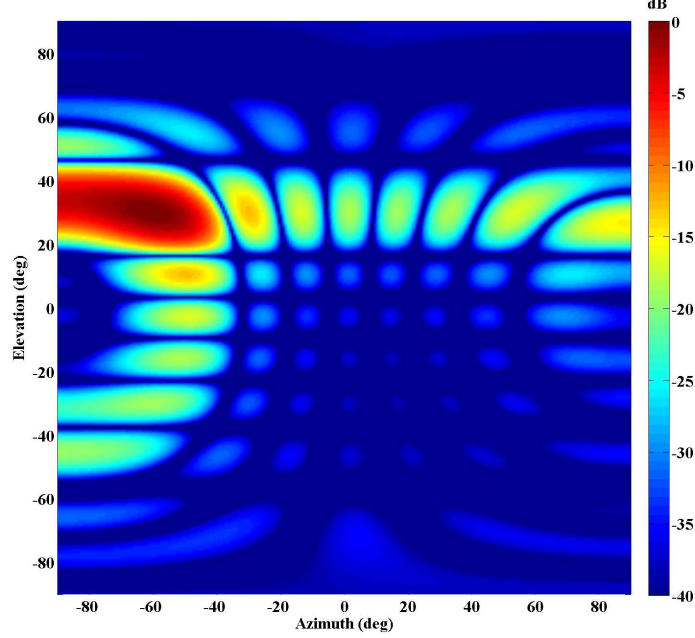
Figure 3.7: Cross-section of FDA power pattern for a 9×9 array cut along the y-z plane at $t = 250\,\mu\text{sec}$. At this time instant the frequency progression caused an electronic scan to $\psi = 30°, \theta = -60°$.
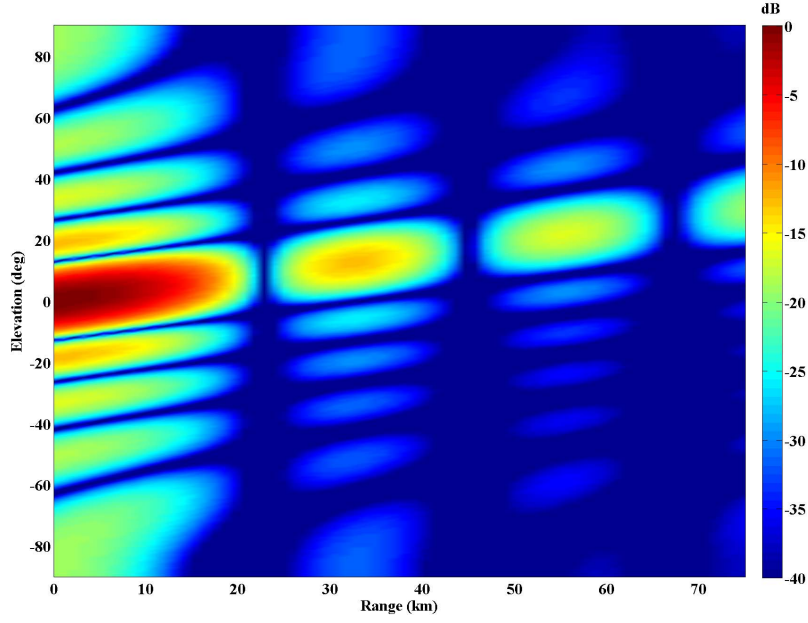
Figure 3.8: Cross-section of FDA power pattern for a 9×9 array cut along the x-z plane for $\theta = 0°$ at $t = 0$ sec. The negative vertical frequency progression $\Delta\omega_z$ causes the pattern to scan toward positive elevation.

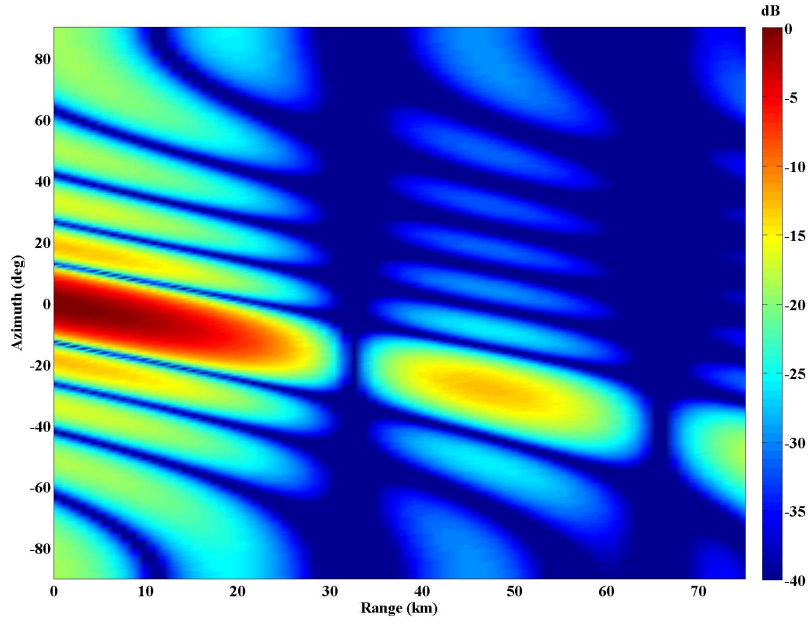Figure 3.9: Cross-section of FDA power pattern for a 9×9 array cut along the x-y plane for $\psi = 0°$ at $t = 0$ sec. The positive horizontal frequency progression $\Delta\omega_y$ causes the pattern to scan toward negative azimuth.

Equation (3.24) when frequency progression is eliminated

$$
\begin{aligned}
\phi_{FDA_y} &= \left(\frac{N-1}{2}\right)\left[\Delta\omega_y\left(t-t_o\right) - k_o d_y \kappa_y - \Delta k_y \hat{\mathbf{r}}_o \cdot \bar{\mathbf{r}}'\right] \\
&= -k_o\left(\frac{N-1}{2}\right)d_y\kappa_y\ , \\
\phi_{FDA_z} &= \left(\frac{P-1}{2}\right)\left[\Delta\omega_z\left(t-t_o\right) - k_o d_z \kappa_z - \Delta k_z \hat{\mathbf{r}}_o \cdot \bar{\mathbf{r}}'\right] \\
&= -k_o\left(\frac{P-1}{2}\right)d_z\kappa_z\ .
\end{aligned} \tag{3.55}
$$

Similarly, without any frequency progression the FDA amplitude term reduces to

$$
\begin{aligned}
&\frac{\sin\left\{\frac{N}{2}\left[\Delta\omega_y\left(t-t_o\right) - k_o d_y \kappa_y - \Delta k_y \hat{\mathbf{r}}_o \cdot \bar{\mathbf{r}}'\right]\right\}}{\sin\left\{\frac{1}{2}\left[\Delta\omega_y\left(t-t_o\right) - k_o d_y \kappa_y - \Delta k_y \hat{\mathbf{r}}_o \cdot \bar{\mathbf{r}}'\right]\right\}} \\
&\times\ \frac{\sin\left\{\frac{P}{2}\left[\Delta\omega_z\left(t-t_o\right) - k_o d_z \kappa_z - \Delta k_z \hat{\mathbf{r}}_o \cdot \bar{\mathbf{r}}'\right]\right\}}{\sin\left\{\frac{1}{2}\left[\Delta\omega_z\left(t-t_o\right) - k_o d_z \kappa_y - \Delta k_z \hat{\mathbf{r}}_o \cdot \bar{\mathbf{r}}'\right]\right\}} \\
&= \frac{\sin\left(-k_o\frac{N}{2}d_y\kappa_y\right)\sin\left(-k_o\frac{P}{2}d_z\kappa_z\right)}{\sin\left(-k_o\frac{1}{2}d_y\kappa_y\right)\sin\left(-k_o\frac{1}{2}d_z\kappa_z\right)} \\
&= \frac{\sin\left(k_o\frac{N}{2}d_y\kappa_y\right)\sin\left(k_o\frac{P}{2}d_z\kappa_z\right)}{\sin\left(k_o\frac{1}{2}d_y\kappa_y\right)\sin\left(k_o\frac{1}{2}d_z\kappa_z\right)}\ ,
\end{aligned} \tag{3.56}
$$

where $\sin\left(-\varphi\right) = -\sin\left(\varphi\right)$ is used in the final step. Again, the limiting FDA amplitude in Equation (3.56) is the same as the CFA amplitude in Equation (3.23).

Next, the planar FDA model is considered for a linear array, i.e., $P = 1$ elevation channel. With $P = 1$, ϕ_{FDA_z} in Equation (3.47) is eliminated removing the phase component. Amplitude contribution in Equation (3.46) is normalized by

$$
\frac{\sin\left(\frac{P}{2}\Psi\right)}{\sin\left(\frac{1}{2}\Psi\right)} = 1\ . \tag{3.57}
$$

The remaining FDA pattern is given by

$$
f\left(t,\bar{\mathbf{r}}',\bar{\mathbf{r}}_o\right)_{FDA} = \exp\left(j\phi_{FDA_y}\right)\frac{\sin\left(\frac{N}{2}\Theta\right)}{\sin\left(\frac{1}{2}\Theta\right)}\ , \tag{3.58}
$$

and agrees with that previously shown in [48].

Table 3.3: FDA parameters used to computationally verify Equation (3.46) and produce the array patterns in Figure 3.10 to Figure 3.14.

Parameter	Value
Number Azimuth Elements (N)	9
Number Elevation Elements (P)	9
Base Operating Frequency ($\omega_o = 2\pi f_o$)	$2\pi(10 \text{ GHz})$
Azimuth Elemental Spacing (d_y)	$\lambda_o/2 = 0.015$ m
Elevation Elemental Spacing (d_z)	$\lambda_o/2 = 0.015$ m
Azimuth Frequency Progression, Scenario A ($\Delta\omega_y = 2\pi\Delta f_y$)	$2\pi(30 \text{ MHz})$
Azimuth Frequency Progression, Scenario B ($\Delta\omega_y = 2\pi\Delta f_y$)	$2\pi(150 \text{ MHz})$
Elevation Frequency Progression ($\Delta\omega_z = 2\pi\Delta f_z$)	0

Frequency progression across both dimensions is introduced with the goal of validating the constraint in Equation (3.39). This validation is performed empirically by using simulation to compare the actual array factor as stated in Equation (3.35) to the analytical array factor in Equation (3.46), recalling the latter is an approximation after eliminating quadratic phase terms. A planar FDA is simulated using the parameters in Table 3.3 with two scenarios presented. In Scenario A horizontal frequency progression is selected to produces a quadratic phase of $\pi/4$, i.e at the limit of the restriction imposed by Equation (3.39). In Scenario B, the frequency progression is intentionally increased by a factor of five such that Equation (3.39) is no longer satisfied. In both cases, no vertical frequency progression exists enabling the FDA range and time dependency to be shown completely in the principal elevation plane.

With no vertical frequency progression, i.e., $\Delta k_z = 0$, and analysis performed in the principal elevation plane, i.e., $\psi = 0$ and so $\kappa_z = \sin\psi = 0$, $\kappa_y = \cos\psi \sin\theta = \sin\theta$, Equation (3.39) reduces to

$$N^2 \Delta k_y d_y \sin\theta < \pm\frac{\pi}{4} \; . \tag{3.59}$$

Figure 3.10 to Figure 3.14 display the actual and analytical array factor for the two scenarios. The power pattern is shown only to 3 dB for clarity. Figure 3.10 and Figure 3.11 plot the actual and analytical array factors respectively for Scenario A.

No appreciable difference between the two plots is observed as total uncompensated phase error in the analytical formulation is limited to $\pi/4$, verifying the analytical model.

Note that Figure 3.10 and Figure 3.11 are plotted only to a range of 10 m. From Equation (3.51) it was observed that the horizontal frequency progression illuminated a point every $1/\Delta f_y$ sec. Alternatively, multiple ranges spaced $c/\Delta f_y$ m apart are illuminated at a given time. With the parameters for Scenario A, this spacing is $c/\Delta f_y = 10$ m and the simulation verifies FDA theory. The antenna pattern is periodic in range and the pattern from $r = 10$ m to $r = 20$ m is identical to the plot presented.

Figure 3.12 and Figure 3.13 show the actual and analytical array factors for Scenario B with the difference between the two shown in Figure 3.14. The plots are limited to a range of $r = 2$ m due the new periodicity of the pattern given the higher frequency progression. The five-fold increase in frequency progression reduced the periodicity in range by a factor of five. In this case, uncompensated phase error in the analytical formulation is $5\pi/4$ at $\theta = \pm 90°$ and the analytical solution diverges from the actual array factor only at the azimuth extremes. By observing Figure 3.14 it is important to note that the errors are not significant until azimuth angle is greater than $\theta = \pm 45°$. Using parameters for Scenario B in Table 3.3 with Equation (3.59),

$$N^2 \Delta k_y d_y \sin\left(\pm 45°\right) = \pm \frac{3.5\pi}{4} \ . \tag{3.60}$$

Peak error occurs at $\theta = \pm 90°$ where, when normalized to peak antenna power, the maximum error is limited to -1.2 dB.

In spotlight mode SAR, elevation and azimuth angles of only a few degrees are of interest. Therefore Equation (3.46) along with the limits imposed by Equation (3.39) are used in FDA SAR processing.

Finally, the analytical pattern in Equation (3.46) was compared to finite-difference time-domain (FDTD) simulation. FDTD is a commonly used computational electro-
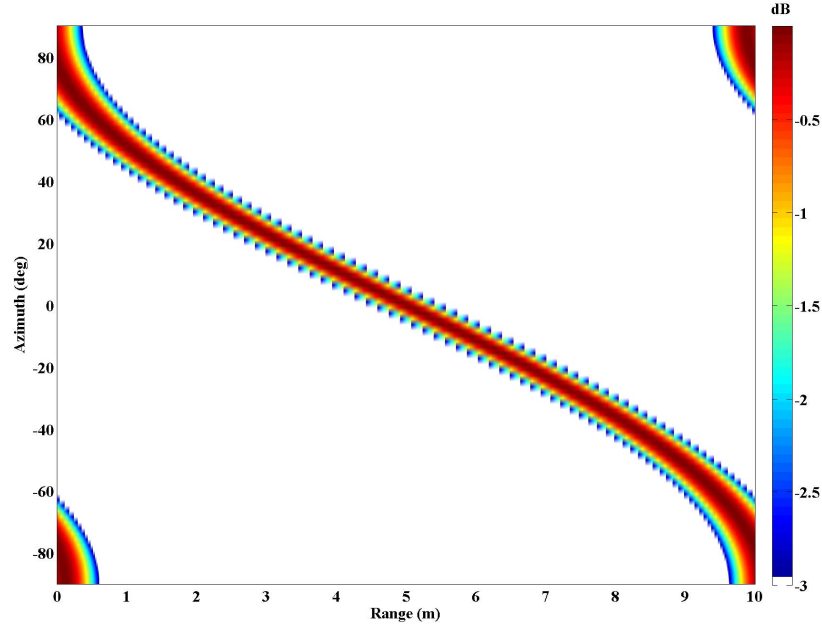
Figure 3.10: *Actual* 9×9 FDA array factor with relatively small frequency progression of $\Delta\omega_y = 2\pi(30 \text{ MHz})$.
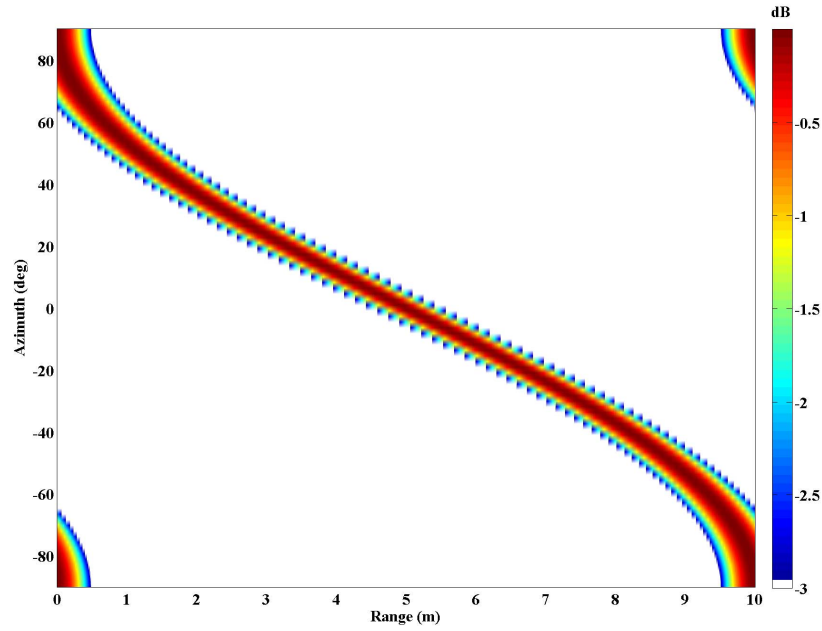
Figure 3.11: *Analytical* 9×9 FDA array factor with relatively small frequency progression of $\Delta\omega_y = 2\pi(30 \text{ MHz})$, such that Equation (3.40) produces a quadratic phase of $\pi/4$. There is no appreciable difference between this plot and Figure 3.10.
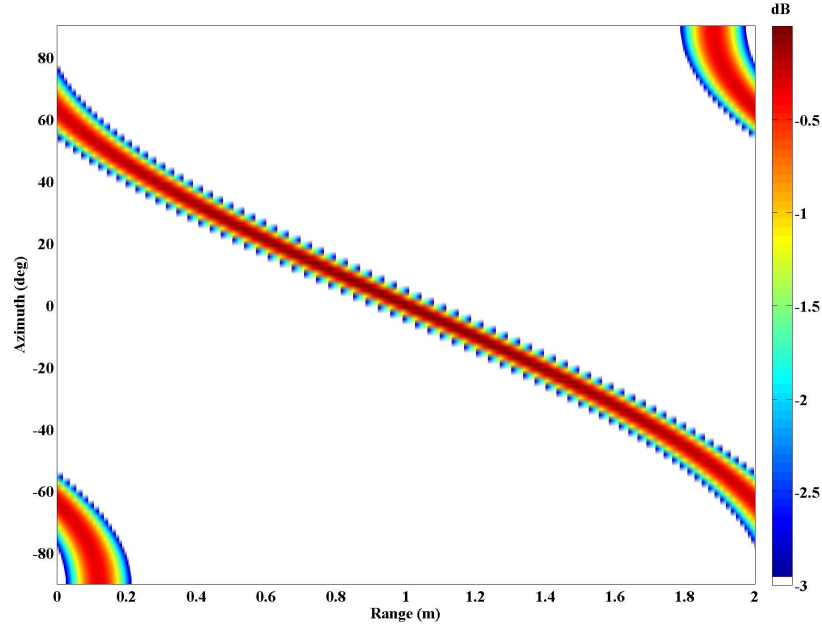
Figure 3.12: *Actual* 9×9 FDA array factor with relatively large frequency progression of $\Delta \omega_y = 2\pi(150 \text{ MHz})$.
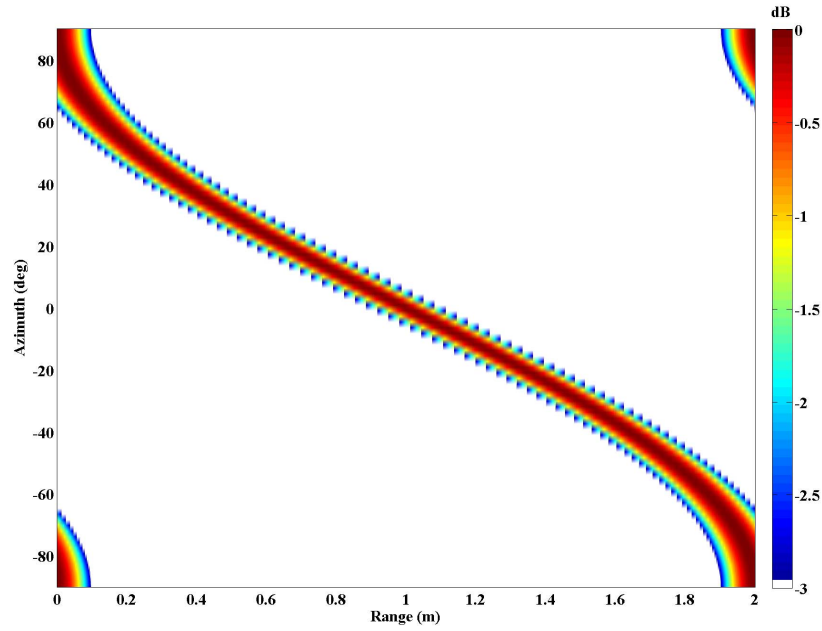
Figure 3.13: *Analytical* 9×9 FDA array factor with relatively large frequency progression of $\Delta \omega_y = 2\pi(150 \text{ MHz})$, such that Equation (3.40) produces a quadratic phase of $5\pi/4$.
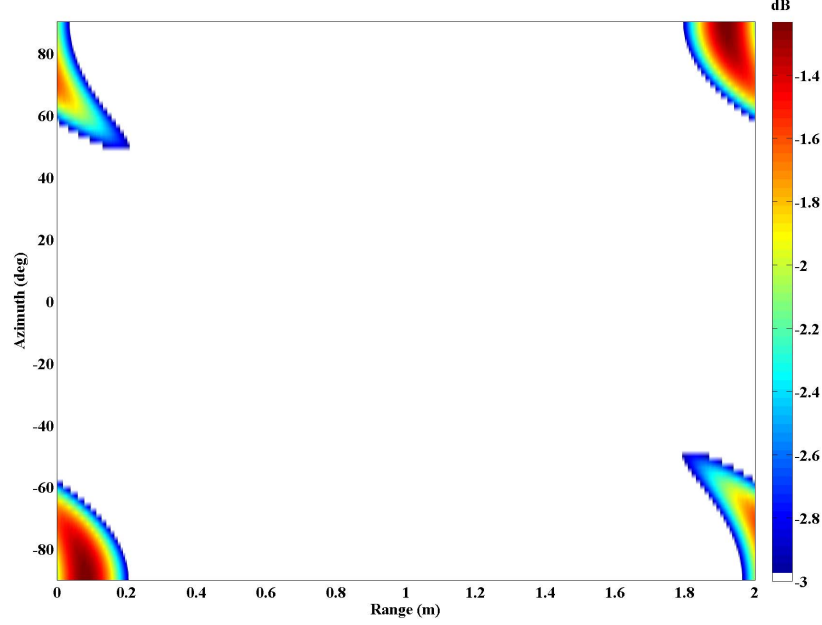
Figure 3.14: Difference plot of results in Figure 3.12 and Figure 3.13. Errors in the analytical development are not significant until azimuth angle is greater than $\theta = \pm 45°$ with peak error occurring at $\theta = \pm 90°$. When normalized to peak antenna power, the maximum error is limited to -1.2 dB

dynamics modelling technique based on Maxwell's equations to compute electric and magnetic fields at every point in a pre-defined region [54]. FDTD simulation time was sufficient to allow FDA pattern to be analyzed in the far-field. Analytical models developed during this research compare favorably with both observed FDTD patterns [45] and 3-D EM simulation radiation characteristics independently reported in [28].

IV. Frequency Diverse Array Waveform Development

Chapter III developed the antenna patterns for both the CFA and FDA systems. The development was used to differentiate between CFA and FDA environment illumination. Before introducing FDA SAR processing, the FDA signal model is developed.

This chapter presents a novel technique to producing a wideband, widebeam waveform through the use of an FDA. The wideband nature is not achieved through common approaches using complex radar hardware or phase coding techniques. Rather, the wideband is realized through simultaneous transmission of frequency offset sinusoidal tones. The real advantage in this technique is scalability. The frequency band coverage is increased/decreased through the addition/removal of antenna elements without the need to redesign waveform generators and other associated hardware. Though this waveform is used in the context of SAR imaging in the following chapter, the signal model developed in this chapter enables the waveform to be utilized in a variety of radar applications.

4.1 Analytic Waveform Development

In typical spotlight SAR applications the platform altitude, and thus grazing angle ψ, is small and approximately constant through the CPI. Once the antenna is steered to the appropriate grazing angle, only steering in azimuth is required to maintain focus on the target scene. In fact, in some SAR systems utilizing phased array antennas rely on mechanical steering for elevation control and electronic steering in azimuth [41]. Therefore, it is appropriate to consider a planar FDA with frequency progression only in azimuth, i.e., $\Delta\omega_y \neq 0$ and $\Delta\omega_z = 0$, in the FDA SAR development.

The composite FDA signal received at point $\bar{\mathbf{r}}'$ is given in Equations (3.42) and (3.46). Combining these two equations yields

$$
\begin{aligned}
s_T\left(t, \bar{\mathbf{r}}', \bar{\mathbf{r}}_o\right)_{FDA} = \ & \exp\left\{j\left[\omega_o\left(t-t_o\right) - k_o\hat{\mathbf{r}}_o \cdot \bar{\mathbf{r}}' + \phi_{FDA_y} + \phi_{FDA_z}\right]\right\} \\
& \times \frac{\sin\left\{\frac{N}{2}\left[\Delta\omega_y\left(t-t_o\right) - k_o d_y \kappa_y - \Delta k_y \hat{\mathbf{r}}_o \cdot \bar{\mathbf{r}}'\right]\right\}}{\sin\left\{\frac{1}{2}\left[\Delta\omega_y\left(t-t_o\right) - k_o d_y \kappa_y - \Delta k_y \hat{\mathbf{r}}_o \cdot \bar{\mathbf{r}}'\right]\right\}} \\
& \times \frac{\sin\left\{\frac{P}{2}\left[\Delta\omega_z\left(t-t_o\right) - k_o d_z \kappa_z - \Delta k_z \hat{\mathbf{r}}_o \cdot \bar{\mathbf{r}}'\right]\right\}}{\sin\left\{\frac{1}{2}\left[\Delta\omega_z\left(t-t_o\right) - k_o d_z \kappa_y - \Delta k_z \hat{\mathbf{r}}_o \cdot \bar{\mathbf{r}}'\right]\right\}} \ ,
\end{aligned}
\tag{4.1}
$$

where

$$
\begin{aligned}
\phi_{FDA_y} &= \left(\frac{N-1}{2}\right)\left[\Delta\omega_y\left(t-t_o\right) - k_o d_y \kappa_y - \Delta k_y \hat{\mathbf{r}}_o \cdot \bar{\mathbf{r}}'\right] \ , \\
\phi_{FDA_z} &= \left(\frac{P-1}{2}\right)\left[\Delta\omega_z\left(t-t_o\right) - k_o d_z \kappa_z - \Delta k_z \hat{\mathbf{r}}_o \cdot \bar{\mathbf{r}}'\right] \ .
\end{aligned}
\tag{4.2}
$$

If $\Delta\omega_z = 0$, then $\Delta k_z = 0$, and with $\psi = \psi_o$ a constant, Equation (4.1) and Equation (4.2) reduce to

$$
\begin{aligned}
s_T\left(t, \bar{\mathbf{r}}', \bar{\mathbf{r}}_o\right)_{FDA} = \ & E\left(\psi_o\right)\exp\left\{j\left[\omega_o\left(t-t_o\right) - k_o\hat{\mathbf{r}}_o \cdot \bar{\mathbf{r}}' + \phi_{FDA_y}\right]\right\} \\
& \times \frac{\sin\left\{\frac{N}{2}\left[\Delta\omega_y\left(t-t_o\right) - k_o d_y \kappa_y - \Delta k_y \hat{\mathbf{r}}_o \cdot \bar{\mathbf{r}}'\right]\right\}}{\sin\left\{\frac{1}{2}\left[\Delta\omega_y\left(t-t_o\right) - k_o d_y \kappa_y - \Delta k_y \hat{\mathbf{r}}_o \cdot \bar{\mathbf{r}}'\right]\right\}} \ ,
\end{aligned}
\tag{4.3}
$$

where

$$
E\left(\psi_o\right) = \exp\left[-j\left(\frac{P-1}{2}\right)k_o d_z \kappa_z\right]\frac{\sin\left(\frac{P}{2}k_o d_z \kappa_z\right)}{\sin\left(\frac{1}{2}k_o d_z \kappa_z\right)} \ .
\tag{4.4}
$$

Amplitude and phase contributions from $E\left(\psi_o\right)$ are constant as P, k_o, d_z, and $\kappa_z = \sin\psi_o$ do not vary throughout the CPI. This term contains known features of the pulse return and is removed by the receiver. Substituting ϕ_{FDA_y} from Equation (4.2)

into Equation (4.3) and collecting like terms results in

$$
\begin{aligned}
s_T\left(t, \bar{\mathbf{r}}', \bar{\mathbf{r}}_o\right)_{FDA} =\ & \exp\left\{j\left[\omega_o + \left(\frac{N-1}{2}\right)\Delta\omega_y\right](t - t_o)\right\} \\
& \times \exp\left\{-j\left[k_o + \left(\frac{N-1}{2}\right)\Delta k_y\right]\hat{\mathbf{r}}_o \cdot \bar{\mathbf{r}}'\right\} \\
& \times \exp\left[-j\left(\frac{N-1}{2}\right)k_o d_y \kappa_y\right] \\
& \times \frac{\sin\left\{\frac{N}{2}\left[\Delta\omega_y\left(t - t_o\right) - k_o d_y \kappa_y - \Delta k_y \hat{\mathbf{r}}_o \cdot \bar{\mathbf{r}}'\right]\right\}}{\sin\left\{\frac{1}{2}\left[\Delta\omega_y\left(t - t_o\right) - k_o d_y \kappa_y - \Delta k_y \hat{\mathbf{r}}_o \cdot \bar{\mathbf{r}}'\right]\right\}} \ .
\end{aligned}
\tag{4.5}
$$

From Equation (4.5) it is observed that the composite signal is an amplitude modulated sinusoidal tone. The center frequency ω_c is

$$
\omega_c = \omega_o + \left(\frac{N-1}{2}\right)\Delta\omega_y \ ,
\tag{4.6}
$$

with corresponding wavenumber k_c

$$
k_c = \frac{\omega_c}{c} \ ,
\tag{4.7}
$$

and wavevector $\bar{\mathbf{k}}_c$

$$
\bar{\mathbf{k}}_c = k_c \hat{\mathbf{r}}_o \ .
\tag{4.8}
$$

The use of center frequency agrees with convention for wideband waveforms. Incorporating Equations (4.6) and (4.7) simplifies Equation (4.5) to

$$
\begin{aligned}
s_T\left(t, \bar{\mathbf{r}}', \bar{\mathbf{r}}_o\right)_{FDA} =\ & \exp\left[j\omega_c\left(t - t_o\right)\right]\exp\left(-j\bar{\mathbf{k}}_c \cdot \bar{\mathbf{r}}'\right) \\
& \times \exp\left[-j\left(\frac{N-1}{2}\right)k_o d_y \kappa_y\right] \\
& \times \frac{\sin\left\{\frac{N}{2}\left[\Delta\omega_y\left(t - t_o\right) - k_o d_y \kappa_y - \Delta k_y \hat{\mathbf{r}}_o \cdot \bar{\mathbf{r}}'\right]\right\}}{\sin\left\{\frac{1}{2}\left[\Delta\omega_y\left(t - t_o\right) - k_o d_y \kappa_y - \Delta k_y \hat{\mathbf{r}}_o \cdot \bar{\mathbf{r}}'\right]\right\}} \ ,
\end{aligned}
\tag{4.9}
$$

where geometric phase effects are represented as time delays seen in many SAR references [29, 51].

Table 4.1: FDA parameters used to produce the waveforms shown in Figure 4.1 to Figure 4.3.

Parameter	Value
Number Azimuth Elements (N)	9
Number Elevation Elements (P)	1
Base Operating Frequency ($\omega_o = 2\pi f_o$)	$2\pi(10 \text{ GHz})$
Azimuth Elemental Spacing (d_y)	$\lambda_o/2 = 0.015 \text{ m}$
Azimuth Frequency Progression, Scenario A ($\Delta\omega_y = 2\pi\Delta f_y$)	$2\pi(1 \text{ kHz})$
Azimuth Frequency Progression, Scenario B ($\Delta\omega_y = 2\pi\Delta f_y$)	$2\pi(1 \text{ GHz})$

Before proceeding, an example is used to visualize the waveform in Equation (4.9). The parameters given in Table 4.1 are used to generate $s_T\left(t, \bar{\mathbf{r}}', \bar{\mathbf{r}}_o\right)_{FDA}$ for two scenarios. The resulting waveforms are shown in Figure 4.1 and Figure 4.2. In Scenario A (Figure 4.1) horizontal frequency progression is small while in Scenario B (Figure 4.2), this value is increased six orders of magnitude. The two features of the amplitude pattern critical to SAR imaging are the periodicity of the amplitude envelope and time extent of peak amplitude response. It will be shown that, when used as a radar waveform, the periodicity leads to range ambiguities while the width of the peak amplitude response is related to range resolution. These two features are analyzed next.

Figure 4.3 displays the magnitude of Figure 4.2. From Figure 4.3 it is evident that the amplitude envelope is periodic in time. Though not strictly a $\operatorname{sinc}(\cdot)$ function given by Equation (2.72), the envelope

$$\frac{\sin\left(\frac{N}{2}\Theta\right)}{\sin\left(\frac{1}{2}\Theta\right)} , \tag{4.10}$$

where Θ is given in Equation (3.44), exhibits a similar structure. The periodicity of the antenna pattern in range, angle, and time due to the low frequency amplitude modulation were analyzed in Section 3.4.2 and in [48]. Equation (3.51) shows the periodicity of the antenna patten in time. The maxima of s_T were shown to occur with a period of $1/\Delta f_y$ sec. This period is dependent only on frequency progression

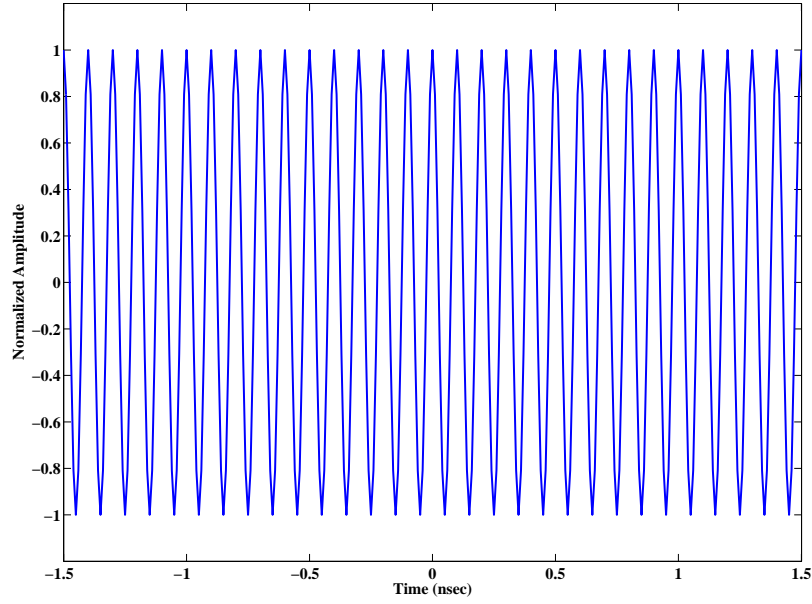Figure 4.1: FDA waveform for a 9×1 array with $\Delta f_y = 1$ kHz. Due to the relatively low frequency progression, no amplitude modulation is observable within the timescale shown.
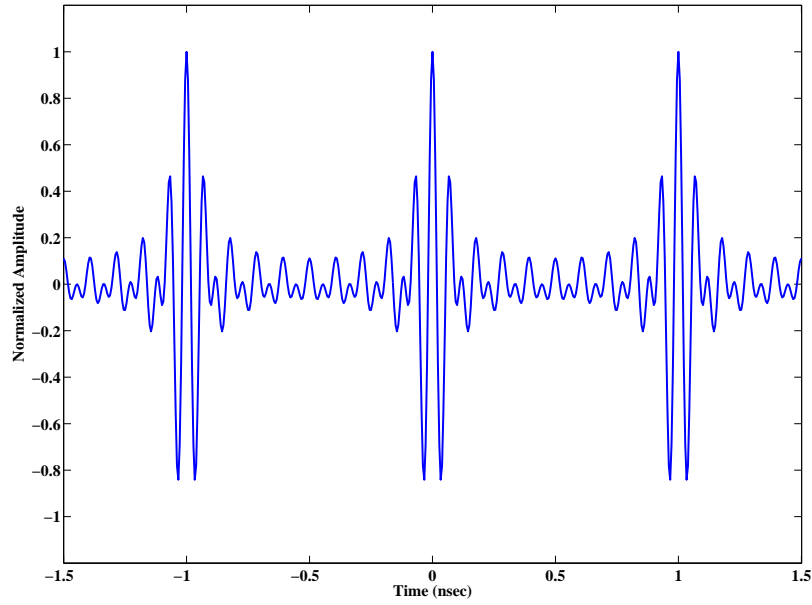
Figure 4.2: FDA waveform for a 9×1 array with $\Delta f_y = 1$ GHz. With a relatively high frequency progression, amplitude modulation is clearly observed within the timescale shown. The periodicity is $1/1$ GHz = 1 nsec as seen here.
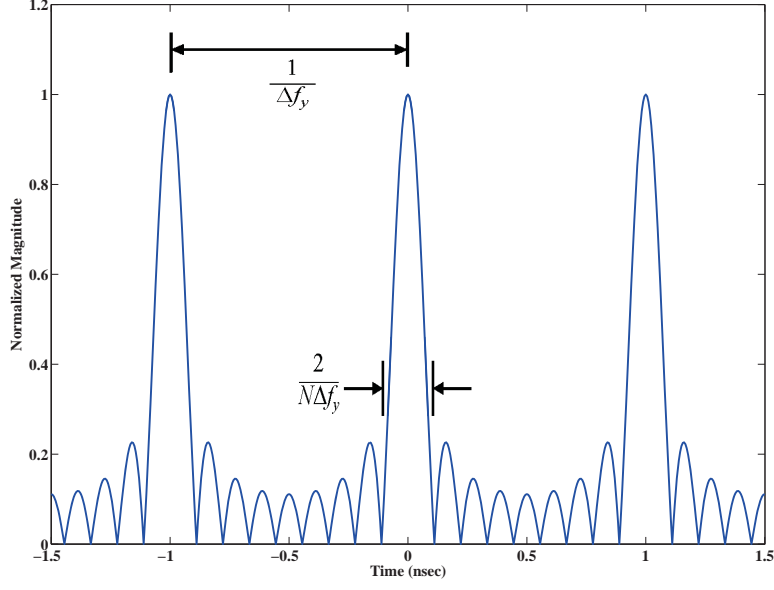
Figure 4.3: Magnitude of FDA waveform from Figure 4.2 with the periodicity and main lobe width shown.

and is independent of center frequency ω_c. In Scenario A with $\Delta f_y = 1$ kHz, this period is $1/1$ kHz $= 1$ msec and the amplitude modulation is not observed within the timescale shown in Figure 4.1. However, in Scenario B with $\Delta f_y = 1$ GHz, the periodicity is $1/1$ GHz $= 1$ nsec and amplitude modulation is easily observed in Figure 4.2 when s_T is plotted over the same timescale. In both figures, the FDA waveform is evaluated at antenna boresight, i.e., $\theta_o = 0$, and at $\bar{\mathbf{r}}' = 0$.

The time extent of the peak amplitude response is given by computing the time between first nulls on either side of the maximum. In Equation (4.9) the first nulls occur at time t when

$$\frac{N}{2}\left[\Delta\omega_y\left(t - t_o\right) - k_o d_y \kappa_y - \Delta k_y \hat{\mathbf{r}}_o \cdot \bar{\mathbf{r}}'\right] = \pi u, \qquad u = \pm 1 . \qquad (4.11)$$

For $u = +1$

$$t_{+1} = \frac{1}{N\Delta f_y} + \frac{k_o d_y \kappa_y}{\Delta\omega_y} + \frac{\hat{\mathbf{r}}_o \cdot \bar{\mathbf{r}}'}{c} + t_o , \qquad (4.12)$$

86

and for $u = -1$

$$t_{-1} = -\frac{1}{N\Delta f_y} + \frac{k_o d_y \kappa_y}{\Delta \omega_y} + \frac{\hat{\mathbf{r}}_o \cdot \bar{\mathbf{r}}'}{c} + t_o \,. \tag{4.13}$$

The time extent given by difference between Equation (4.12) and Equation (4.13) is

$$\Delta t = \frac{2}{N\Delta f_y} \,. \tag{4.14}$$

In Figure 4.3 the sinc-shaped amplitude modulation and periodicity is clearly displayed. One critical observation is that a windowed portion of this waveform is similar in structure to a pulse compressed waveform [25]. Pulse compression is traditionally performed in receiver processing to improve range resolution. A novel technique proposed here in achieving pulse compression is the use of an FDA. The FDA effectively performs pulse compression by simultaneously transmitting N sinusoidal pulses. The composite signal has a peak response concentrated in a time duration shorter than the total pulse width, and the waveform appears as a very narrow pulse. This compression is not due to any channel level amplitude modulation. In order to ensure maximum power on target, each element should transmit peak power for the duration of a pulse [50] as is the case with the FDA waveform. The resulting amplitude modulation is a result of interference between the waveforms transmitted by each channel. The use of the FDA waveform for radar applications was first introduced in [22].

4.2   Selection of FDA Waveform Parameters

The FDA waveform in Equation (4.9) depends on many system parameters and optimal selection of these parameter values are application specific. In this presentation parameter selection is optimized for FDA SAR imaging. Upon initial inspection, the base frequency ω_o, horizontal frequency progression Δf_y, number of horizontal channels N, horizontal elemental spacing d_y, and pulse width τ_c are variable. However, it will be shown that these parameters are mutually dependent such that design trade-offs must be considered.

A high ω_o is desired as cross-range resolution is improved with the associated shorter wavelength λ_o per Equation (2.3). It is noted however that ω_o is restricted by practical considerations such as hardware limitations, frequency dependent atmospheric attenuation effects, and operational restrictions such as Federal Communications Commission regulations. Elemental spacing d_y is commonly set as $\lambda_o/2$ to prevent grating lobes [52] and therefore is dependent on ω_o. There is little flexibility in selecting these parameters.

The periodicity in waveform amplitude directly influences selection of pulse width. A long pulse is desired to maximize power on target [49, 52] as mentioned. However, the FDA waveform cannot have an arbitrarily long pulse width. The composite signal will contain multiple maxima (see Figure 4.3) resulting in range ambiguities. Having analyzed waveform periodicity in Section 3.4.2, restricting the pulse width on all channels to

$$\tau_c = \left| \frac{1}{\Delta f_y} \right| , \tag{4.15}$$

ensures exactly one peak will occur during the pulse duration. The absolute value accounts for a possible negative frequency progression. The FDA waveform is then defined by

$$s\left(t\right) = \text{rect}\left(\frac{t}{\tau_c}\right) s_T\left(t, \bar{\mathbf{r}}', \bar{\mathbf{r}}_o\right)_{FDA} . \tag{4.16}$$

With each channel transmitting a pulsed sinusoid, FDA waveform bandwidth is next derived. The 3 dB bandwidth for a pulsed sinusoid is inversely proportional to pulse width. The selection of τ_c in Equation (4.15) leads to bandwidth for the nth channel B_n of [16]

$$B_n = 0.886\frac{1}{\tau_c} = 0.886\Delta f_y \approx \Delta f_y, \qquad n = 0, \ldots, N - 1 . \tag{4.17}$$

The subscript p is omitted as, with no vertical frequency progression, each vertical row of array elements operates at the same center frequency and bandwidth. The above selection of τ_c and Δf_y leads to an FDA with N channels spaced Δf_y in frequency,

each operating over spectrum of width Δf_y. Thus, total waveform bandwidth B_{FDA} of the FDA waveform is

$$B_{FDA} = N \left| \Delta f_y \right| . \tag{4.18}$$

Figure 4.4 plots the spectrum of individual channels of Scenario B from Table 4.1. With $\Delta f_y = 1$ GHz, the pulse width is $\tau_c = 1$ nsec from Equation (4.15). It is easily seen that each channel operates over a unique frequency band, with no overlap between bands to the 3 dB level (dashed line in Figure 4.4), and the $N = 9$ elements operate over a contiguous frequency bands. Figure 4.5 plots the spectrum of the composite pulsed FDA waveform. The simultaneous use of individual narrowband sinusoidal pulses produces a wideband composite signal with bandwidth given by Equation (4.18), $B_{FDA} = 9$ GHz in this case, and centered at $\omega_c = 14$ GHz from Equation (4.6).

One metric used to measure a radar waveform's utility is the pulse compression ratio (PCR) [26, 52]. The PCR is the ratio of the uncompressed pulse width to the compressed pulse width. The PCR is alternatively expressed by the time-bandwidth product (TBP). Long pulse duration is desired for more energy on target and larger bandwidth improves range resolution. Therefore, a large TBP is desired. From Equation (4.15) and Equation (4.18), this value is easily computed for the FDA waveform as

$$\text{TBP}_{FDA} = \tau_c B_{FDA} = N . \tag{4.19}$$

Increasing horizontal channels therefore improves the TBP and system performance.

Finer range resolution is proportional to waveform bandwidth from Equation (2.1). Though increasing bandwidth in the FDA waveform requires a large Δf_y and/or large N from Equation (4.18), upper limits restrict selection of these two parameters. From Equation (4.15), a large frequency progression limits pulse duration and has the undesirable effect of reducing power on target. Practical size constraints limit the number of horizontal channels N.
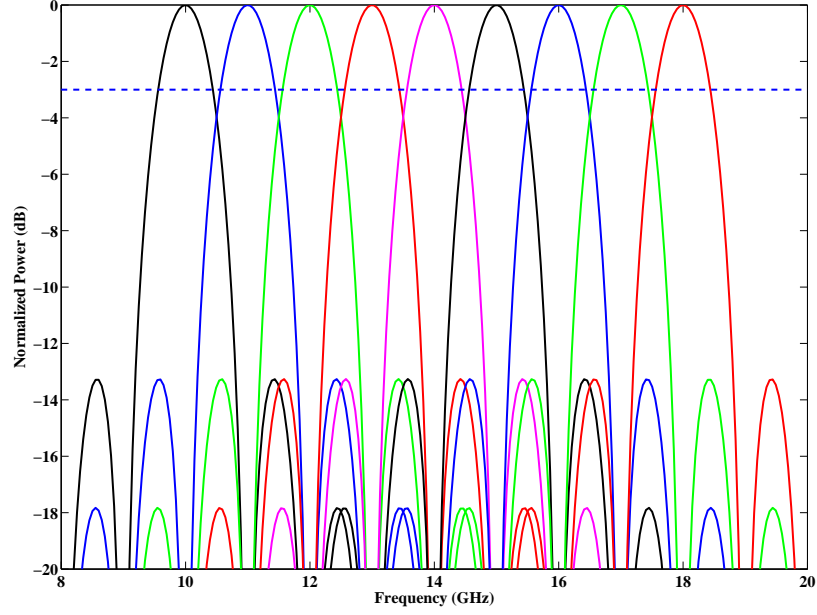
Figure 4.4: The spectrum of individual channels from Scenario B from Table 4.1. Each channel operates over a unique frequency band, with no overlap between bands to the 3 dB level (dashed line in figure).
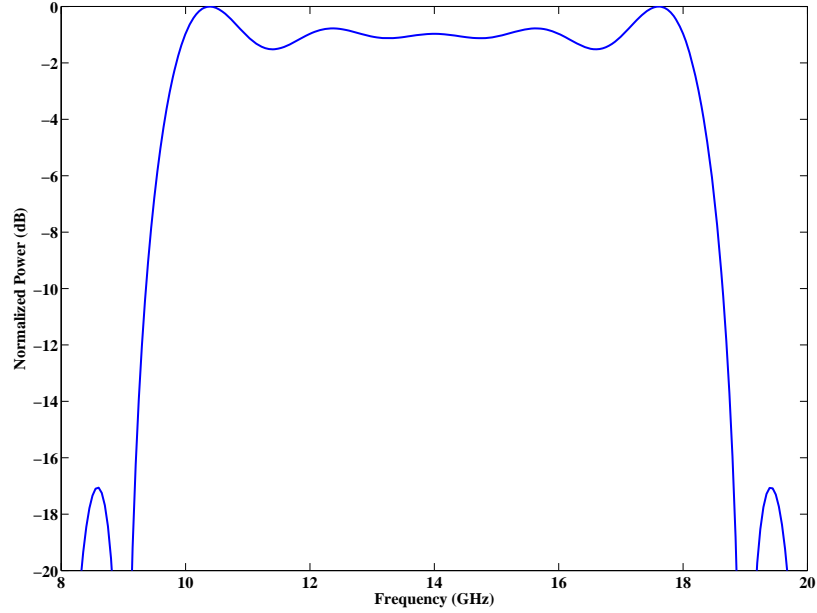

Figure 4.5: Composite FDA waveform spectrum. The simultaneous use of individual narrowband sinusoidal pulses produces a wideband composite signal.

4.3 Comparison of FDA and LFM Waveform

In Chapter II, it was stated that linear frequency modulation is the most common form of pulse compression. Thus, it is of interest to compare LFM and FDA waveform properties. The LFM bandwidth is given by Equation (2.44) making the time-bandwidth product

$$\text{TBP}_{LFM} = \tau_c \frac{\alpha \tau_c}{\pi} = \frac{\alpha \tau_c^2}{\pi} \ . \tag{4.20}$$

The TBP is improved by either increasing chirp rate α or increasing pulse duration τ_c. With the FDA waveform, this increase is achieved by increasing the total number of transmit channels N.

An important aspect of radar signals is analysis of matched filter characteristics through the ambiguity function [33]. In general radar applications, a pulse return is a delayed and possibly Doppler shifted replica of the transmitted pulse. Thus, if the transmitted pulse is given by $s(t)$, the pulse return $r(t)$ is

$$r(t) = s(t - \tau_o) \exp(j2\pi f_d t) \ , \tag{4.21}$$

where τ_o is the round-trip propagation time from Equation (2.45) and f_d is the Doppler frequency shift. A pulse return's signal power is a small fraction of that transmitted and matched filtering is used to maximize SNR. The matched filtering operation often also performs pulse compression. It has been shown that for complex transmitted signal $s(t)$, the optimum matched filter is given by $s^*(-t)$ assuming Gaussian noise, where * denotes conjugation [49]. This signal is a time reversed and conjugated replica of the transmitted signal and the matched filter can be seen as an autocorrelation operation. The output of the matched filter is given by [25]

$$y(\tau_o, f_d) = \int_{-\infty}^{\infty} s(t - \tau_o) s^*(t) \exp(j2\pi f_d t) \, dt \ , \tag{4.22}$$

and is often called the time-frequency autocorrelation function (TFACF). Note that the matched filter $s^*(-t)$ does not account for any range delay or Doppler shift in the pulse return in Equation (4.21). The effect of range and frequency mismatch on the output of the matched filter is given by the ambiguity function (AF), $\chi(\tau_o, f_d)$, which is often shown as the magnitude squared of Equation (4.22)

$$\chi(\tau_o, f_d) = |y(\tau_o, f_d)|^2 \ . \tag{4.23}$$

The AF for the LFM and FDA waveforms are shown in Figure 4.6 and Figure 4.7 respectively to enable an empirical comparison of the two waveforms. The LFM waveform is produced using a 9×1 array with center frequency $f_c = 14$ GHz, $B_{LFM} = 9$ GHz, and $\tau_c = 1$ nsec. The FDA waveform is produced also for a 9×1 array with base frequency $f_o = 10$ GHz, $\Delta f_y = 1$ GHz, and $\tau_c = 1$ nsec as per Scenario B in Table 4.1. With each channel using $B_n = 1$ GHz of bandwidth, the total bandwidth utilized by the FDA is $B_{FDA} = 9$ GHz from Equation (4.18). These parameters were selected such that the two waveforms have the same time duration, bandwidth, and center frequency.

The principal disadvantage of LFM compression is range-doppler coupling [52] that is evident in the AF in Figure 4.6. A positive Doppler shift on the pulse return causes the matched filter output to peak sooner than if no shift was present, and the apparent target range appears closer than the true range. A negative Doppler shift has the opposite effect. However, with the FDA case illustrated in Figure 4.7, no range-doppler coupling is present and the matched filter output occurs at the correct time (range) even with severe Doppler shifts present.

As discussed, the LFM pulse is compressed via matched filtering when the pulse return is received by the radar. The FDA (solid line) and compressed LFM (dashed line) waveforms are compared in Figure 4.8. These plots are essentially cuts of the respective AF along the $f_d = 0$ Hz axis. The two waveforms have a comparable TBP and range resolution given the same pulse width and bandwidth used. It is important

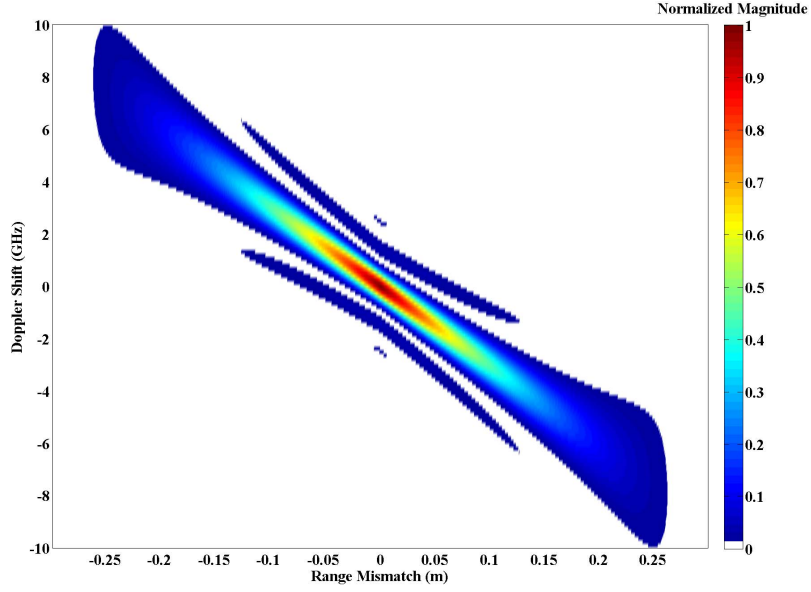Figure 4.6: Ambiguity function for *LFM waveform* using a 9×1 array with center frequency $f_c = 14$ GHz, $B_{LFM} = 9$ GHz, and $\tau_c = 1$ nsec. Range-doppler coupling is clearly evident.
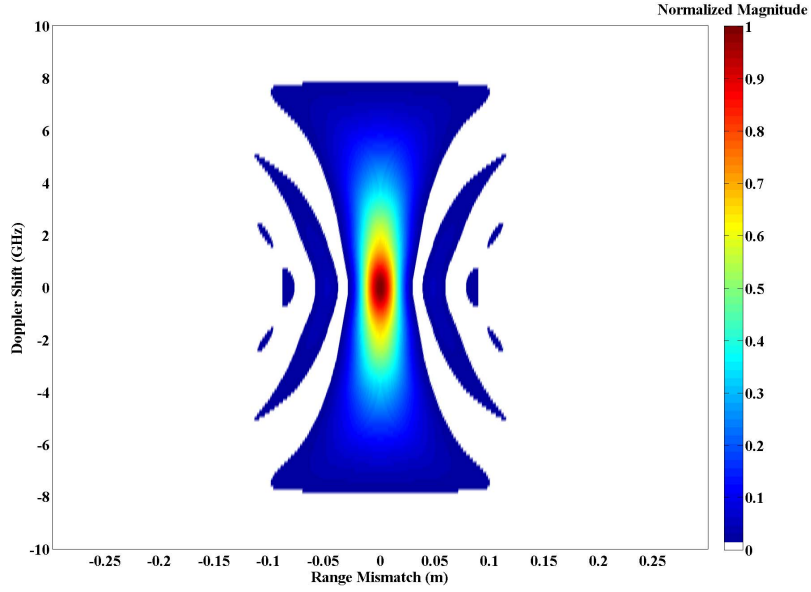
Figure 4.7: Ambiguity function for *FDA waveform* using a 9×1 array with base frequency $f_o = 10$ GHz, $\Delta f_y = 1$ GHz, and $\tau_c = 1$ nsec. No range-doppler coupling is present.
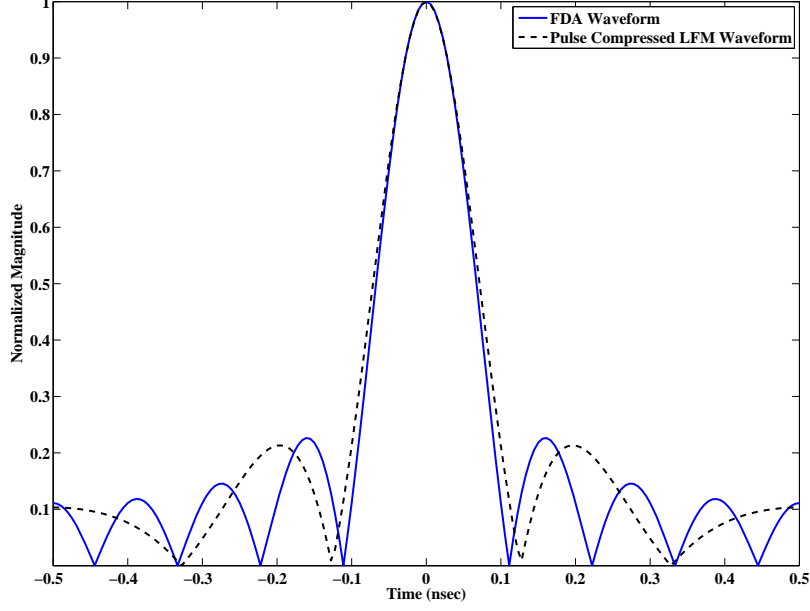
Figure 4.8: Transmitted pulse magnitudes for 9×1 array: (Solid Line) FDA processing with $f_o = 10$ GHz, $\Delta f_y = 1$ GHz, and $\tau_c = 1$ nsec, and (Dashed Line) LFM waveform with $B_{LFM} = 9$ GHz of bandwidth and $\tau_c = 1$ nsec. The two waveforms yield similar range resolution.

to note that with a linear array transmitting LFM pulses, each element transmits across the entire waveform bandwidth, whereas in FDA each element transmits across a $1/N$ portion of the spectrum.

4.4 Azimuth Dependent Point Spread Function (PSF)

In Section 4.3 it is shown that no range-doppler coupling is present in the FDA AF. The FDA waveform however does introduce a coupling between range and azimuth. From Equation (3.49) it is shown that FDA maxima occur when

$$\frac{1}{2} \left[\Delta\omega_y \left(t - t_o \right) - k_o d_y \kappa_y - \Delta k_y \hat{\mathbf{r}}_o \cdot \bar{\mathbf{r}}' \right] = \pi u, \qquad u = 0, \pm 1, \dots, \qquad (4.24)$$

In Equation (4.15), pulse width is restricted such that only one maximum is realized during the pulse duration. This maximum corresponds to the $u = 0$ case in Equation (4.24). When analyzing the timing of the maximum at scene center, i.e., $\bar{\mathbf{r}}' = 0$,

Equation (4.24) reduces to

$$\Delta\omega_y\,(t - t_o) - k_o d_y \kappa_y = 0\,.\tag{4.25}$$

Substituting $\Delta\omega_y = 2\pi\Delta f_y$, $k_o = 2\pi/\lambda_o$, $\kappa_y = \cos\psi_o\sin\theta_o$ and solving for t in Equation (4.25), the maximum occurs at time

$$t_{app} = t_o + \frac{d_y\cos\psi_o\sin\theta_o}{\lambda_o\Delta f_y}\,.\tag{4.26}$$

In Equation (4.26), t_o is the actual propagation time to the target. The second term is an additional time difference Δt_{FDA} that is a function of the target's azimuth and FDA frequency progression (ψ_o is constant as previously stated)

$$\Delta t_{FDA}\,(\theta_o, \Delta f_y) = \frac{d_y\cos\psi_o\sin\theta_o}{\lambda_o\Delta f_y}\,.\tag{4.27}$$

This value has the effect of making the target range appear to be greater or smaller than actual range, and the subscript *app* is included in Equation (4.26). The range offset decreases with increasing frequency progression, where in the limiting case $t_{app} = t_o$.

The azimuth dependency is clearly evident when the waveform is plotted. Figure 4.9 plots a $\tau_c = 1$ nsec pulse and parameters from Scenario B in Table 4.1. This snapshot represents the waveform after $t = 2$ nsec propagation time. The array is oriented along the cross-range axis with the reference element located at $(0,0)$ and remaining elements in the negative y (cross-range) direction. Azimuth dependency is considered for three cases: along antenna boresight (black dashed line at $\theta_o = 0$), positive azimuth (red dashed line at $\theta_o = \pi/4$), and negative azimuth (green dashed line at $\theta_o = -\pi/4$). The wide beam nature of the antenna pattern is observed in this figure.

At antenna boresight, $\theta_o = 0$ (black dashed in Figure 4.9) and therefore $\Delta t_{FDA} = 0$ from Equation (4.27). In this case the maximum occurs in the center of the pulse

Figure 4.9: A $\tau_c = 1$ nsec pulse radiated from a 9×1 FDA with $f_o = 10$ GHz, and $\Delta f_y = 1$ GHz after $t = 2$ nsec propagation. The azimuth dependency is clearly evident as the peak response occurs late in the pulse duration for positive azimuth (red dashed line), is centered at radar boresight (black dashed line), and occurs early in the pulse for negative azimuth (green dashed line).
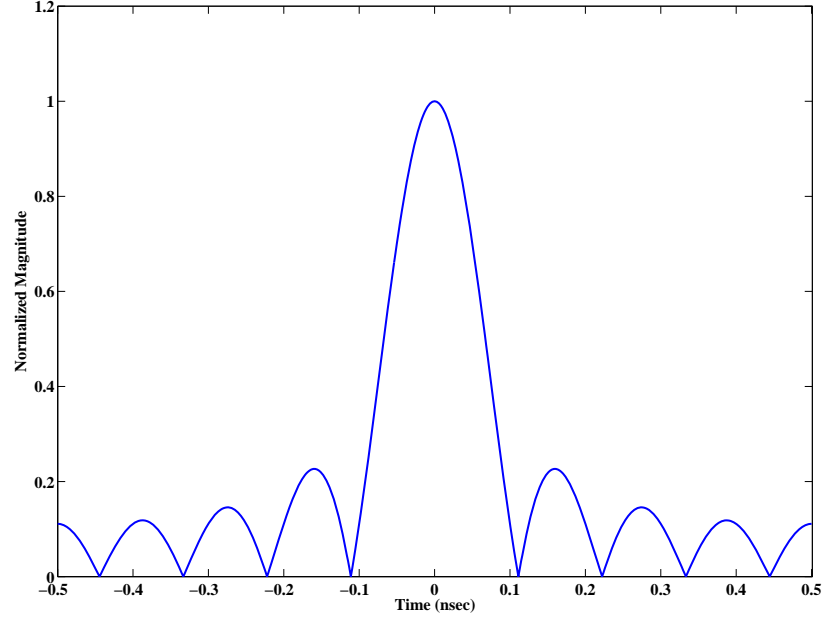
Figure 4.10: Cross-section of FDA waveform from Figure 4.9 for $\theta = 0$ (black dashed in Figure 4.9). At antenna boresight, the peak is centered in the pulse.
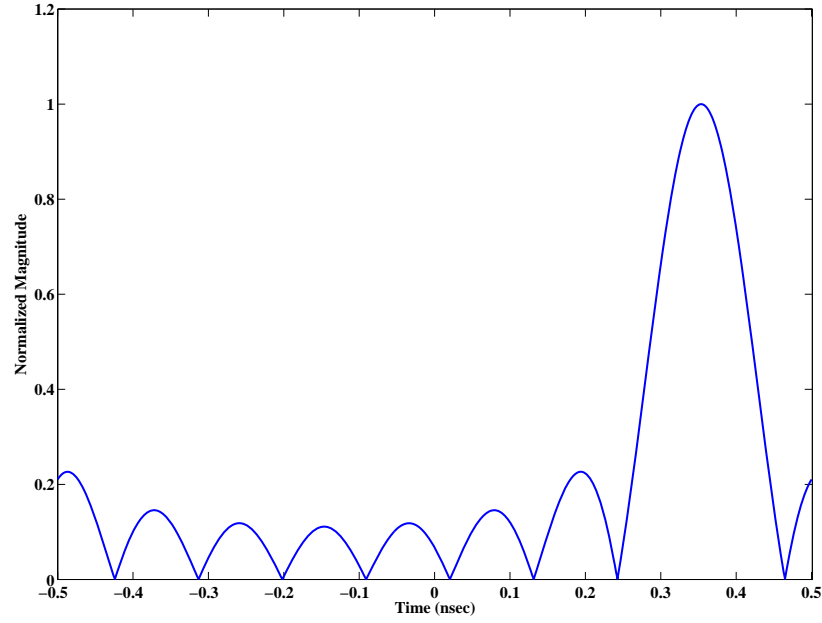
Figure 4.11: Cross-section of FDA waveform from Figure 4.9 for $\theta = \pi/4$ (red dashed in Figure 4.9). For positive azimuth the location of the peak magnitude is delayed within the pulse duration. The parameters used yield a delay of $\Delta t_{FDA} = 0.35$ nsec.
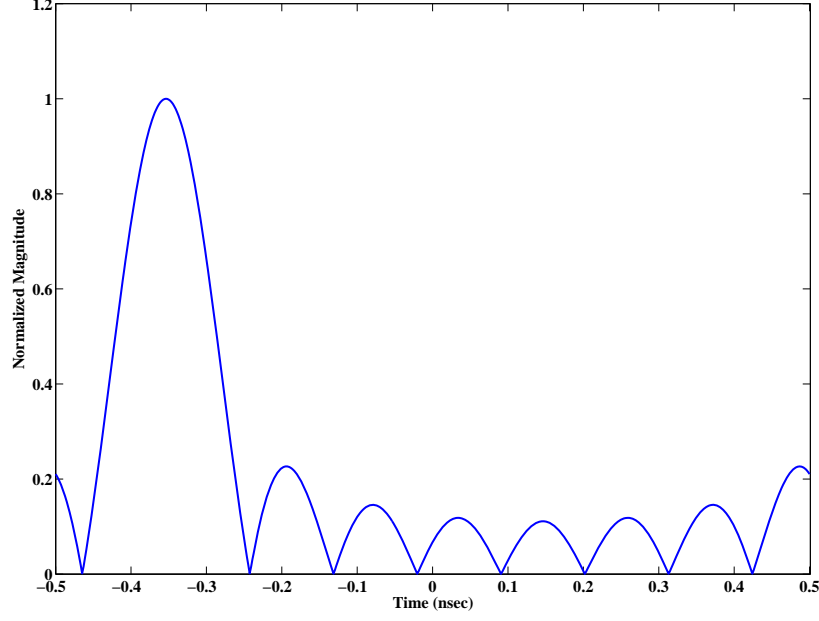
Figure 4.12: Cross-section of FDA waveform from Figure 4.9 for $\theta = -\pi/4$ (green dashed in Figure 4.9). For negative azimuth the location of the peak magnitude is advanced within the pulse duration. The parameters used yield an advance of $\Delta t_{FDA} = -0.35$ nsec.
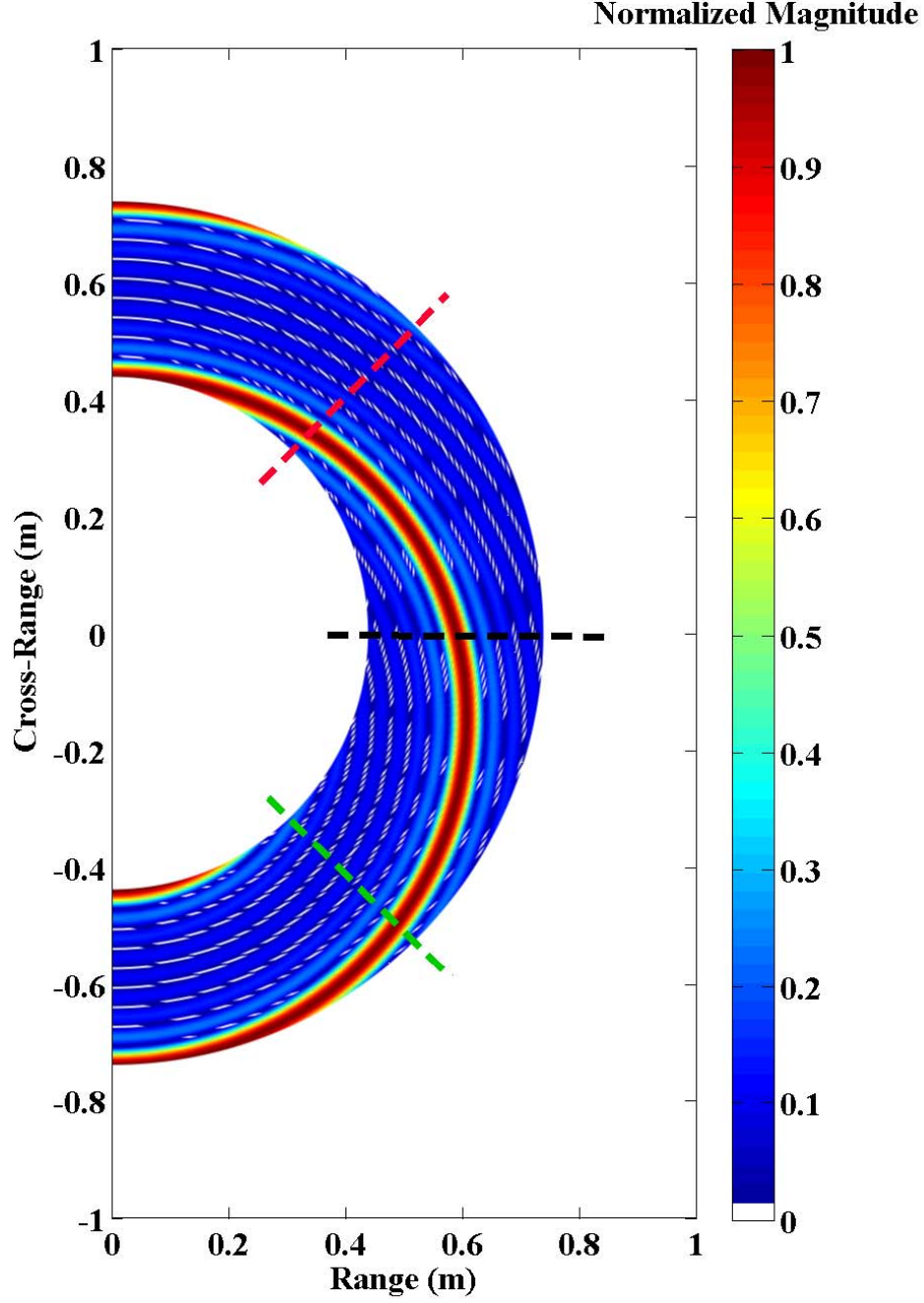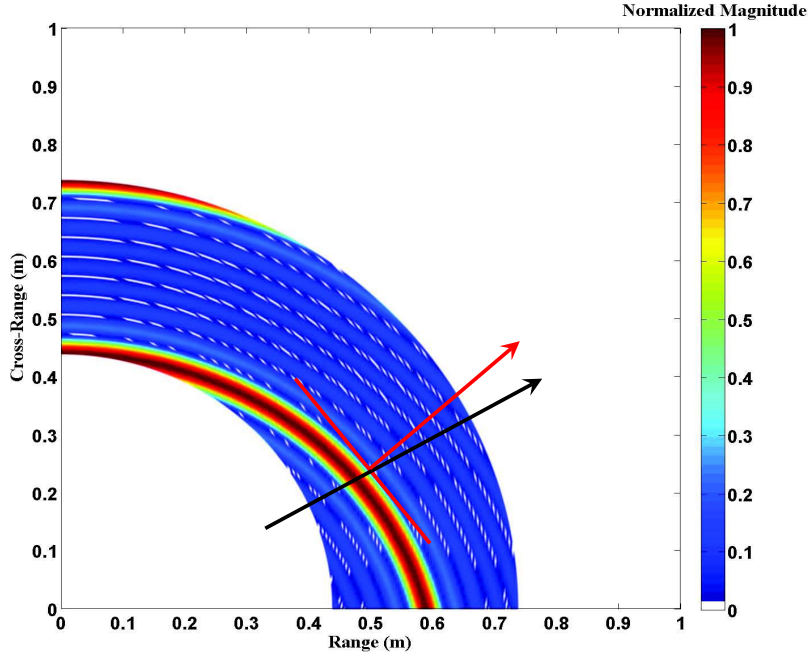

Figure 4.13: A $\tau_c = 1$ nsec pulse radiated from a 9×1 FDA with $f_o = 10$ GHz, and $\Delta f_y = 1$ GHz after $t = 2$ nsec propagation. The solid black line represents the normal to the plane of uniform phase at a given azimuth angle. The solid red line represents the normal to the plane of uniform amplitude the pulse.

98

as seen in Figure 4.10. However, if $\theta_o > 0$ then $\Delta t_{FDA} > 0$ and the waveform maximum is delayed in the pulse. Figure 4.11 shows the transmitted waveform for this case when $\theta_o = \pi/4$ (red dashed in Figure 4.9). With the parameters used and setting $\psi_o = 0$, Equation (4.27) equates to $\Delta t_{FDA} = 0.35$ nsec for $\theta_o = \pi/4$, and is confirmed by the figure. Finally, if $\theta_o < 0$ then $\Delta t_{FDA} < 0$ and the maximum appears earlier in the pulse. Figure 4.12 shows the transmitted waveform for this case when $\theta_o = -\pi/4$ (green dashed in Figure 4.9). With the parameters used and setting $\psi_o = 0$, Equation (4.27) equates to $\Delta t_{FDA} = -0.35$ nsec for $\theta_o = -\pi/4$ where the negative sign indicates an advance. A negative frequency progression has the opposite effect by advancing the appearance of the maximum for positive azimuth and delaying the maximum for negative azimuth. From Equation (4.27) it is seen that Δt_{FDA} increases with azimuth and is inversely proportional to frequency progression.

The scattered return is a time-delayed replica of transmitted signal. Thus the return, and therefore range PSF, for a point target depends on the target's azimuth location. This azimuth-dependent range profile is an important consideration in FDA SAR processing. As the radar traverses the synthetic aperture, the varying $\theta_o$ causes the apparent a shift in target range between collection locations. This apparent target motion induced by FDA waveform produces a defocued image and must be accounted for.

Along with varying the apparent target range, the FDA waveform exhibits another interesting characteristic. In Sec. 2.1.3 it was shown that the orientation of the propagating uniform plane wave is normal to propagation direction by Equation (2.31). In the base case, both phase and amplitude were uniform across the plane. The FDA waveform produces a non-uniform plane wave as seen in Figure 4.13. Equation (4.9) and Equation (2.22) contain the same phase content, and therefore phase is constant for a given range. Waveform amplitude is azimuth dependent and, for a given range, planes of constant phase and constant amplitude do not coincide. As the waveform propagates, these two planes have differing orientations.

99

In Figure 4.13, the solid black line represents the normal to the plane of uniform phase at a given azimuth angle. The solid red line represents the normal to the plane of uniform amplitude the pulse. It is difficult to define propagation direction with the two different orientations.

4.5   Receive Signal Modelling

Heretofore, FDA illumination patterns were discussed, i.e., the development considered one-way propagation from the np^{th} antenna channel to a target in the scene at point r'. SAR data collection is a two-way problem and signal models developed in Chapter III are now modified to reflect this fact.

Derivation of the receive signal follows analysis of the FDA illumination pattern in Section 3.4. The analysis must retain the two-way path length from each channel to the target and back. The total path length travelled for a signal transmitted for channel np is broken down into the round-trip distance between that channel and the reference channel, and the round-trip distance from the reference channel to point r'.

Specific receiver architecture designs drives the composite received signal. Hardware may be designed such that each channel has an associated wideband receive module that is able to capture entire bandwidth of the FDA waveform. The drawback of this approach is the need for NP wideband receive elements. Additionally, phase shifters are required on each channel to properly align phase of the incoming signal.

Alternatively, receiver architecture may be designed such that each channel receives at its specific transmit frequency and bandwidth. In this second method, the composite wideband waveform is reconstructed as a post-processing step. The benefit of this approach is that each channel essentially operates independently. While negating the need for dedicated wideband receive modules, each channel requires a band-pass filter instead. Such filters must be sufficiently narrowband to pass appropriate frequency content to prevent cross-channel bleedthrough. With the selection of

frequency progression and pulse width in Section 4.2, it was shown in Figure 4.4 there was no overlap in operating bands to the 3 dB level and initially shows this assumption to be appropriate. However, strict requirements on center frequency and pass band region require filters to be near ideal. Any deviation in filter properties or selection of waveform parameters different than in Section 4.2 may lead to cross-channel interference.

The approach used in this research aims to simplify receiver design. A single wideband receiver is co-located with the reference element and is the design used in [48]. Development of the receive signal begins by modifying the transmit signal in Equation (3.35)

$$
s_T\left(t, \bar{\mathbf{r}}', \bar{\mathbf{r}}_o\right) \;=\; \sum_{n=0}^{N-1}\sum_{p=0}^{P-1} \exp\left[j\omega_{np}\left(t - t_o\right)\right]
$$
$$
\times \exp\left(j\bar{\mathbf{k}}_{np}\cdot\bar{\mathbf{d}}_{np}\right)\exp\left(-j\bar{\mathbf{k}}_{np}\cdot\bar{\mathbf{r}}'\right) \;, \qquad (4.28)
$$

to account for two-way propagation. Equation (4.28) shows the one-way path length travelled by the transmitted waveform received at r' is the path length from the np^{th} element to the reference element $(\bar{\mathbf{d}}_{np})$, the path length from the reference element to scene center $(\bar{\mathbf{r}}_o$ inherent in $t_o)$, and the path length from scene center to point r' $(\bar{\mathbf{r}}')$. With the selected receiver architecture, the total path length travelled by a sinusoid transmitted by each channel to the single wideband receiver at the reference element must account for round-trip distance over $\bar{\mathbf{r}}_o$ and $\bar{\mathbf{r}}'$ and one-way distance over $\bar{\mathbf{d}}_{np}$.

The received signal $r\left(t, \bar{\mathbf{r}}', \bar{\mathbf{r}}_o\right)_{FDA}$ at the reference element from a point scatterer at $\bar{\mathbf{r}}'$ with reflectivity $\rho_{\bar{\mathbf{r}}'}$ is then

$$
r\left(t, \bar{\mathbf{r}}', \bar{\mathbf{r}}_o\right)_{FDA} \;=\; \sum_{n=0}^{N-1}\sum_{p=0}^{P-1} \rho_{\bar{\mathbf{r}}'} \exp\left[j\omega_{np}\left(t - 2t_o\right)\right]
$$
$$
\times \exp\left(j\bar{\mathbf{k}}_{np}\cdot\bar{\mathbf{d}}_{np}\right)\exp\left(-j2\bar{\mathbf{k}}_{np}\cdot\bar{\mathbf{r}}'\right) \;. \qquad (4.29)
$$

Following the development in Chapter III, Equation (4.29) is reduced to

$$
\begin{aligned}
r\left(t, \bar{\mathbf{r}}', \bar{\mathbf{r}}_o\right)_{FDA} = {} & \rho_{\bar{\mathbf{r}}'} \exp\left\{j\left[\omega_o\left(t - 2t_o\right) - 2k_o\hat{\mathbf{r}}_o \cdot \bar{\mathbf{r}}' + \phi'_{FDA_y} + \phi'_{FDA_z}\right]\right\} \\
& \times \frac{\sin\left\{\frac{N}{2}\left[\Delta\omega_y\left(t - 2t_o\right) - k_o d_y \kappa_y - 2\Delta k_y \hat{\mathbf{r}}_o \cdot \bar{\mathbf{r}}'\right]\right\}}{\sin\left\{\frac{1}{2}\left[\Delta\omega_y\left(t - 2t_o\right) - k_o d_y \kappa_y - 2\Delta k_y \hat{\mathbf{r}}_o \cdot \bar{\mathbf{r}}'\right]\right\}} \\
& \times \frac{\sin\left\{\frac{P}{2}\left[\Delta\omega_z\left(t - 2t_o\right) - k_o d_z \kappa_z - 2\Delta k_z \hat{\mathbf{r}}_o \cdot \bar{\mathbf{r}}'\right]\right\}}{\sin\left\{\frac{1}{2}\left[\Delta\omega_z\left(t - 2t_o\right) - k_o d_z \kappa_y - 2\Delta k_z \hat{\mathbf{r}}_o \cdot \bar{\mathbf{r}}'\right]\right\}} \ , \qquad (4.30)
\end{aligned}
$$

where

$$
\begin{aligned}
\phi'_{FDA_y} &= \left(\frac{N-1}{2}\right)\left[\Delta\omega_y\left(t - 2t_o\right) - k_o d_y \kappa_y - 2\Delta k_y \hat{\mathbf{r}}_o \cdot \bar{\mathbf{r}}'\right] \ , \\
\phi'_{FDA_z} &= \left(\frac{P-1}{2}\right)\left[\Delta\omega_z\left(t - 2t_o\right) - k_o d_z \kappa_z - 2\Delta k_z \hat{\mathbf{r}}_o \cdot \bar{\mathbf{r}}'\right] \ . \qquad (4.31)
\end{aligned}
$$

Finally, assuming only a horizontal frequency progression and omitting elevation term $E\left(\psi_o\right)$ from Equation (4.4) as before, the received signal is

$$
\begin{aligned}
r\left(t, \bar{\mathbf{r}}', \bar{\mathbf{r}}_o\right)_{FDA} = {} & \rho_{\bar{\mathbf{r}}'} \exp\left[j\omega_c\left(t - 2t_o\right)\right] \exp\left(-j2\bar{\mathbf{k}}_c \cdot \bar{\mathbf{r}}'\right) \\
& \times \exp\left[-j\left(\frac{N-1}{2}\right) k_o d_y \kappa_y\right] \\
& \times \frac{\sin\left\{\frac{N}{2}\left[\Delta\omega_y\left(t - 2t_o\right) - k_o d_y \kappa_y - 2\Delta k_y \hat{\mathbf{r}}_o \cdot \bar{\mathbf{r}}'\right]\right\}}{\sin\left\{\frac{1}{2}\left[\Delta\omega_y\left(t - 2t_o\right) - k_o d_y \kappa_y - 2\Delta k_y \hat{\mathbf{r}}_o \cdot \bar{\mathbf{r}}'\right]\right\}} \ , \qquad (4.32)
\end{aligned}
$$

where ω_c and $\bar{\mathbf{k}}_c$ were given in Equation (4.6) and Equation (4.8), respectively.

V. Frequency Diverse Array Application to SAR

With traditional waveforms, the range profile for a point target, i.e., the range PSF, is invariant to viewing angle θ_o. When performing backprojection, sampled returns add coherently at the true target location in the reconstruction grid producing a focused SAR image. Chapter IV introduced the FDA waveform and showed a PSF that changed with viewing angle. As azimuth angle θ_o varies while the collection platform traverses the synthetic aperture, a range error proportional to Equation (4.27) is induced at each collection location. The apparent target location varies across the CPI and it will be shown that this effect causes target defocusing in the reconstructed image.

This chapter details processing of FDA collected data for SAR imaging. Various approaches can be applied to account for the FDA induced range and azimuth effects to obtain a properly focused SAR image. It may be possible to manipulate the phase history directly to account for these effects before image reconstruction. Alternatively, the specific image reconstruction algorithm used can be modified to ensure formation of a focused SAR image. The latter approach is used in this research.

Variation in waveform amplitude resulted in an apparent time advance or delay per Equation (4.26). The time-domain backprojection algorithm introduced in Section 2.2.2 performed image reconstruction based on time delays and therefore is most suited to account for FDA effects. Additionally, it will be seen that FDA SAR processing produces a set of apparent collection locations. These locations are non-uniformly spaced and appear to alter the platform's actual flight path. While these facts are transparent to the backprojection algorithm, two-dimensional interpolation in FFT-based algorithms discussed in Section 2.2.1 is made more difficult.

Two alternative modifications to the backprojection algorithm are presented. In Section 5.1, backprojection is performed as usual. However, it will be shown that the sample return chosen for backprojection to any given pixel is not simply the interpolated sample corresponding to round-trip propagation time. The second approach detailed in Section 5.2 aims to exploit the unique properties of the FDA waveform to

Table 5.1: FDA parameters used in simulating FDA based phase history of the scenario in Figure 2.11.

Parameter	Value
Number Azimuth Elements (N)	45
Number Elevation Elements (P)	1
Base Operating Frequency (f_o)	10 GHz
Center Frequency (f_c)	10.44 GHz
Azimuth Frequency Progression (Δf_y)	20 MHz
Waveform Bandwidth	900 MHz
L	430 m

improve cross-range resolution in SAR imagery. Specifically, an additional processing step is introduced between data collection and image reconstruction that creates a mapping from the set of actual collection locations to a set of apparent SAR collection locations. This mapping aims to match the phase history collected using the FDA waveform at the actual collection locations with phase history collected from the apparent collection locations had traditional waveforms been used.

5.1 Image Reconstruction: Modified Backprojection

The need for a modified backprojection algorithm with FDA collected data can be seen by a simple imaging example. Figure 5.1 shows the reconstructed image of the scenario in Figure 2.11. FDA data collection is performed with parameters used in Table 5.1 and backprojection is applied without modification. Given the higher center frequency as compared to that used in Section 2.2.2, a synthetic aperture length of $L = 430$ m (reduced from $L = 450$ m) is required to achieve equal range and cross-range resolutions $\delta_x = \delta_y = 0.167$ m. As previously discussed, the azimuth dependent PSF induces apparent target motion leading to a defocused image.

The first approach developed to properly account for FDA effects modifies the backprojection algorithm. With traditional backprojection, the interpolated time sample chosen for backprojection to reconstruction grid point $\hat{\mathbf{r}}'$ is dictated by actual

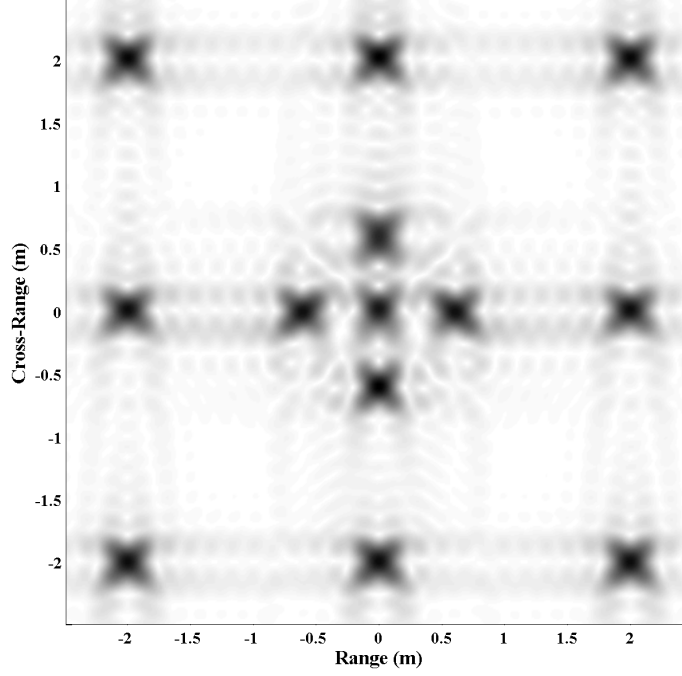Figure 5.1: Reconstructed image of the scenario in Figure 2.11 using FDA collected data. The Backprojection algorithm is used for image reconstruction without modification. The azimuth dependent PSF induces apparent target motion leading to a defocused image.
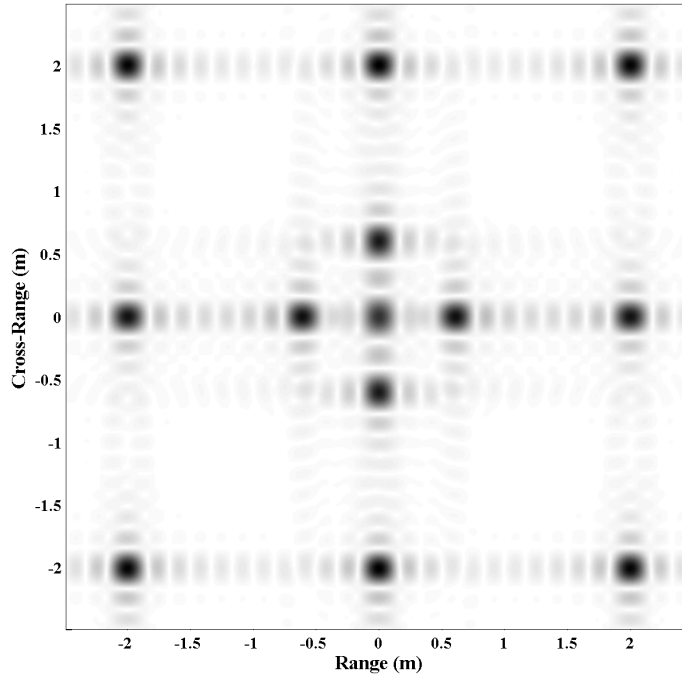

Figure 5.2: By applying an appropriate time and phase correction to account for FDA waveform effects, the modified backprojection algorithm produces a focused image.

105

target range in Equation (2.78) as

$$\hat{\tau}' = 2t_o + \frac{2\,\hat{\mathbf{r}}_o \cdot \hat{\mathbf{r}}'}{c} \ . \tag{5.1}$$

However, apparent target range is computed by analyzing the timing of peak magnitude in the pulse return. The peak time in Equation (4.32) is given when

$$\frac{1}{2}\left[\Delta\omega_y\left(t - 2t_o\right) - k_o d_y \kappa_y - 2\Delta k_y \hat{\mathbf{r}}_o \cdot \bar{\mathbf{r}}'\right] = 0 \ , \tag{5.2}$$

and solving for t yields the apparent round-trip target time as

$$t_{app} = 2t_o + \frac{2\,\hat{\mathbf{r}}_o \cdot \bar{\mathbf{r}}'}{c} + \frac{d_y \cos\psi_o \sin\theta_o}{\lambda_o \Delta f_y} \ . \tag{5.3}$$

Because image formation is performed in two dimensions, $\bar{\mathbf{r}}'$ in Equation (5.3) is replaced with $\hat{\mathbf{r}}'$ and the interpolated time sample chosen for backprojection to $\hat{\mathbf{r}}'$ is

$$\hat{\tau}'_{app} = 2t_o + \frac{2\,\hat{\mathbf{r}}_o \cdot \hat{\mathbf{r}}'}{c} + \frac{d_y \cos\psi_o \sin\theta_o}{\lambda_o \Delta f_y} \ . \tag{5.4}$$

In conjunction with this timing correction, an associated phase correction of

$$\exp\left(-j\omega_c \frac{d_y \cos\psi_o \sin\theta_o}{\lambda_o \Delta f_y}\right) \ . \tag{5.5}$$

must also be applied. Implementing these changes into the backprojection algorithm produces a focused SAR image as shown in Figure 5.2.

5.2 Image Reconstruction: Modified SAR Baseline

Section 5.1 presented one method of processing FDA data to produce a focused SAR image with range and cross-range resolutions consistent with Equation (2.1) and Equation (2.3) respectively. This capability extends wideband waveforms available for SAR applications with the advantage of simplicity in waveform generation and scalability to wider bandwidths. An alternative method to image reconstruction

106

modifies locations from which the phase history is backprojected. Specifically, the actual collection locations are individually mapped to an apparent set of collection locations from which the backprojection process is performed. This secondary set of locations creates an apparent synthetic aperture.

Derivation of the apparent synthetic aperture is presented first, and it will be shown that focused SAR imagery is produced with the modified processing. Next FDA parameters are varied to achieve an improvement in cross-range resolution.

5.2.1 Apparent Collection Locations. The first step in deriving the secondary set of collection locations is computation of the plane of uniform amplitude for the FDA waveform. In Section 2.1.3, the orientation of the propagating uniform plane wave was derived as the slope of a line tangent to the spherical phasefront. Similarly, the slope of a line tangent to uniform amplitude wavefront is used to derive an apparent azimuth angle θ_{app} from which the signal originated.

Equation (4.26) describes the location of peak amplitude in the transmitted signal. Propagation time t_o is given in Equation (2.28), and from Equation (2.17)

$$
\begin{aligned}
\sin \theta_o &= \frac{y - R_y}{r_o \cos \psi_o} \\
&= \frac{y - R_y}{\cos \psi_o \sqrt{(x - R_x)^2 + (y - R_y)^2 + (z - R_z)^2}} \, .
\end{aligned}
\tag{5.6}
$$

Substituting Equation (5.6) into Equation (4.26) and implicitly differentiating with respect to y yields

$$
\begin{aligned}
D\left[t_{app}\right] &= D\left[t_o\right] + D\left[\frac{d_y \cos \psi_o \sin \theta_o}{\lambda_o \Delta f_y}\right] \\
0 &= D\left[t_o\right] \\
&\quad + \frac{d_y}{\lambda_o \Delta f_y} D\left[\frac{y - R_y}{\sqrt{(x - R_x)^2 + (y - R_y)^2 + (z - R_z)^2}}\right] \, ,
\end{aligned}
\tag{5.7}
$$

where $D[\cdot]$ denotes denotes a partial derivative with respect to y $(\partial/\partial y)$. In Equation (2.30), $D[t_o]$ is shown to be

$$\frac{(x - R_x)\frac{\partial x}{\partial y}}{cr_o} + \frac{(y - R_y)}{cr_o} + \frac{(z - R_z)\frac{\partial z}{\partial y}}{cr_o} \; . \tag{5.8}$$

The second term in Equation (5.7) can be shown to simplify to

$$\frac{d_y}{\lambda_o \Delta f_y r_o^2} \left[r_o + \frac{(y - R_y)(x - R_x)\frac{\partial x}{\partial y}}{r_o} \right.$$
$$\left. + \frac{(y - R_y)^2}{r_o} + \frac{(y - R_y)(z - R_z)\frac{\partial z}{\partial y}}{r_o} \right] \; . \tag{5.9}$$

The slope of the tangent line in the x-y image reconstruction plane is of interest and the $\partial z/\partial y$ terms are omitted as before. Collecting like terms in Equations (5.8) and (5.9) and solving for $\partial x/\partial y$ yields

$$\frac{\partial x}{\partial y} = -\frac{(y - R_y) + \frac{d_y f_o}{\Delta f_y}\left[1 + \left(\frac{y - R_y}{r_o}\right)^2\right]}{(x - R_x) + \frac{d_y f_o}{\Delta f_y}\left[\frac{(y - R_y)}{r_o}\frac{(x - R_x)}{r_o}\right]} \; . \tag{5.10}$$

From Equation (2.17),

$$\frac{y - R_y}{r_o} = \cos\psi_o \frac{y - R_y}{r_o \cos\psi_o} = \cos\psi_o \sin\theta_o = \kappa_y \; , \tag{5.11}$$

and

$$\frac{x - R_x}{r_o} = \cos\psi_o \frac{x - R_x}{r_o \cos\psi_o} = \cos\psi_o \cos\theta_o = \kappa_x \; , \tag{5.12}$$

allows simplification of Equation (5.10) to

$$\frac{\partial x}{\partial y} = -\frac{(y - R_y) + \frac{d_y f_o}{\Delta f_y}\left(1 + \kappa_y^2\right)}{(x - R_x) + \frac{d_y f_o}{\Delta f_y}\left(\kappa_x \kappa_y\right)} \; . \tag{5.13}$$

The apparent azimuth angle θ_{app} at scene center is the inverse tanget of the slope in Equation (5.13) evaluated at $y = Y_c$, $x = X_c$

$$\theta_{app} = -\tan^{-1}\left[\frac{(Y_c - R_y) + \frac{d_y f_o}{\Delta f_y}\left(1 + \kappa_y^2\right)}{(X_c - R_x) + \frac{d_y f_o}{\Delta f_y}\left(\kappa_x \kappa_y\right)}\right] . \qquad (5.14)$$

Typically, f_o remains fixed and, as elemental spacing is referenced to associated wavelength λ_o, d_y also is fixed. At a given collection location and with f_o and d_y fixed, θ_{app} depends solely on frequency progression Δf_y. A decrease in frequency progression leads to increase in the apparent view angle. Conversely, increasing Δf_y decreases its effect on θ_{app} until the limiting case where $\theta_{app} = \theta' = \theta_o$ in Equation (2.31).

Having computed apparent view angle, discussion turns to range correction. The time offset Δt_{FDA} is given in Equation (4.27) and can be compensated by adjusting range r_o by an offset of

$$\begin{aligned}
\Delta r_o &= c\left(\frac{d_y \cos \psi_o \sin \theta_o}{\lambda_o \Delta f_y}\right) \\
&= \frac{d_y f_o \cos \psi_o \sin \theta_o}{\Delta f_y} ,
\end{aligned} \qquad (5.15)$$

resulting in a new apparent range to scene center

$$r_{app} = r_o + \Delta r_o . \qquad (5.16)$$

With θ_{app} in Equation (5.14) and r_{app} in Equation (5.16) a new set of collection points can now be computed. For each actual collection location, the apparent collection locations R_{xapp}, R_{yapp}, and R_{zapp} are found using Equation (2.17)

$$\begin{aligned}
R_{xapp} &= X_c - r_{app} \cos \psi_o \cos \theta_{app} , \\
R_{yapp} &= Y_c - r_{app} \cos \psi_o \sin \theta_{app} , \\
R_{zapp} &= Z_c - r_{app} \sin \psi_o .
\end{aligned} \qquad (5.17)$$

The set of apparent collection locations require $\bar{\mathbf{r}}_o$, $\hat{\mathbf{r}}_o$, $\bar{\mathbf{k}}_{app}$, and $\overline{\mathbf{R}}$ to be redefined as

$$\bar{\mathbf{r}}_{app} = r_{app} \left(\hat{\mathbf{x}} \cos \psi_o \cos \theta_{app} + \hat{\mathbf{y}} \cos \psi_o \sin \theta_{app} + \hat{\mathbf{z}} \sin \psi_o \right) \ ,$$

$$\hat{\mathbf{r}}_{app} = \hat{\mathbf{x}} \cos \psi_o \cos \theta_{app} + \hat{\mathbf{y}} \cos \psi_o \sin \theta_{app} + \hat{\mathbf{z}} \sin \psi_o \ ,$$

$$\bar{\mathbf{k}}_{app} = k_c \hat{\mathbf{r}}_{app} \ ,$$

$$\overline{\mathbf{R}}_{app} = \hat{\mathbf{x}} R_{xapp} + \hat{\mathbf{y}} R_{yapp} + \hat{\mathbf{z}} R_{zapp} \ . \tag{5.18}$$

Image reconstruction using time-domain backprojection proceeds as usual with two notable exceptions. First, the phase history is backprojected from the apparent collection locations $\overline{\mathbf{R}}_{app}$ and not actual collection locations. Second, altering view angle to θ_{app} and range to r_{app} require respective phase corrections during backprojection.

In the pulse return of Equation (4.32), phase content in

$$\exp\left[j\omega_c \left(t - 2t_o \right) \right] \exp\left[-j \left(\frac{N-1}{2} \right) k_o d_y \kappa_y \right] \ , \tag{5.19}$$

are known features of the recovered signal and are removed by the radar receiver. Ideally, it is desired that the remaining phase history be corrected to accurately portray phase content as if collected at $\overline{\mathbf{R}}_{app}$.

The first phase correction accounts for range adjustment Δr_o made in Equation (5.16). This phase correction is identical to Equation (5.5) and is independent of target location $\bar{\mathbf{r}}'$. The second phase correction must account for the difference between actual wavevector $\bar{\mathbf{k}}_c$ and apparent wavevector $\bar{\mathbf{k}}_{app}$. Target phase information in Equation (4.32) is

$$\exp\left(-j2\,\bar{\mathbf{k}}_c \cdot \bar{\mathbf{r}}' \right) \ . \tag{5.20}$$

Had collection actually been performed at points $\overline{\mathbf{R}}_{app}$, this phase would have been

$$\exp\left(-j2\,\bar{\mathbf{k}}_{app} \cdot \bar{\mathbf{r}}' \right) \ , \tag{5.21}$$

110

and, ideally, the required phase correction is given by

$$\exp\left[-j2\,\bar{\mathbf{r}}'\cdot\left(\bar{\mathbf{k}}_{app}-\bar{\mathbf{k}}_c\right)\right]\ .\tag{5.22}$$

However, Equation (5.22) is target location specific. Specifically, this phase can be perfectly corrected for a single target at $\bar{\mathbf{r}}'$, given this information is known a priori. For the moment this phase will remain uncorrected and re-addressed in Section 5.4.

5.2.2 Modified FDA Point Spread Function. Development of the modified PSF for FDA SAR processing follows the base case in Section 2.2.2. Target reflectivity and phase information in Equation (4.32) for a single point scatterer is given by

$$\rho_{\bar{\mathbf{r}}'}\exp\left(-j2\,\bar{\mathbf{k}}_c\cdot\bar{\mathbf{r}}'\right)\ ,\tag{5.23}$$

where
$$2\,\bar{\mathbf{k}}_c\cdot\bar{\mathbf{r}}' = 2\,k_c\left(x'\cos\psi_o\cos\theta_o + y'\cos\psi_o\sin\theta_o + z'\sin\psi_o\right)\ .\tag{5.24}$$

With traditional backprojection, the phase correction in Equation (2.83) is applied to each pixel. When backprojecting from $\overline{\mathbf{R}}_{app}$, the phase associated with each grid location $\hat{\mathbf{r}}'$ is

$$2\,\bar{\mathbf{k}}_{app}\cdot\hat{\mathbf{r}}' = 2\,k_c\left(\hat{x}'\cos\psi_o\cos\theta_{app} + \hat{y}'\cos\psi_o\sin\theta_{app}\right)\ .\tag{5.25}$$

and Equation (2.84) becomes

$$\begin{aligned}
2\,\bar{\mathbf{k}}_c\cdot\bar{\mathbf{r}}' - 2\,\bar{\mathbf{k}}_{app}\cdot\hat{\mathbf{r}}' &=\ 2k_c\left[\cos\psi_o\left(x'\cos\theta_o - \hat{x}'\cos\theta_{app}\right)\right.\\
&\qquad \left. +\cos\psi_o\left(y'\sin\theta_o - \hat{y}'\sin\theta_{app}\right) + z'\sin\psi_o\right]\\
&=\ 2k_c\left[\cos\psi_o\cos\theta_o\left(x' - \hat{x}'\frac{\cos\theta_{app}}{\cos\theta_o}\right)\right.\\
&\qquad \left. +\cos\psi_o\sin\theta_o\left(y' - \hat{y}'\frac{\sin\theta_{app}}{\sin\theta_o}\right) + z'\sin\psi_o\right]\ .\tag{5.26}
\end{aligned}$$

The integration of these phase corrections across θ_{app} defines the PSF

$$\text{PSF}_{FDA} = \int\limits_{\theta_{app}} d\theta_{app}\, \rho_{\bar{\mathbf{r}}'} \exp\left[-j2\left(\bar{\mathbf{k}}_c \cdot \bar{\mathbf{r}}' - \bar{\mathbf{k}}_{app} \cdot \hat{\mathbf{r}}'\right)\right] \ . \tag{5.27}$$

Using small angel approximations, Equation (5.26) is reduced to

$$
\begin{aligned}
2\left(\bar{\mathbf{k}}_c \cdot \bar{\mathbf{r}}' - \bar{\mathbf{k}}_{app} \cdot \hat{\mathbf{r}}'\right) \;=\; & 2k_c\Bigg[\cos\psi_o \cos\theta_o \left(x' - \hat{x}'\right) \\
& + \cos\psi_o \sin\theta_o \left(y' - \hat{y}'\frac{\theta_{app}}{\theta_o}\right) + z'\sin\psi_o\Bigg] \\
\;=\; & 2k_c\left[\kappa_x \left(x' - \hat{x}'\right) + \kappa_y \left(y' - \hat{y}'\frac{\theta_{app}}{\theta_o}\right) + z'\kappa_z\right] \ . \tag{5.28}
\end{aligned}
$$

and the PSF simplifies to

$$
\begin{aligned}
\text{PSF}_{FDA} \;\approx\; & \rho_{\bar{\mathbf{r}}'}\int\limits_{\theta_{app}} d\theta_{app}\, \exp\left[-j2k_c \left(x' - \hat{x}'\right)\kappa_x\right] \\
& \times \exp\left[-j2k_c \left(y' - \hat{y}'\frac{\theta_{app}}{\theta_o}\right)\kappa_y\right] \\
& \times \exp\left(-j2k_o z'\kappa_z\right) \ . \tag{5.29}
\end{aligned}
$$

Equation (5.29) is nearly identical to the traditional Backprojection PSF given by Equation (2.86) in Section 2.2.2. In Equation (5.29), $\exp\left(-j2k_o z'\kappa_z\right)$ only contributes a constant phase across the integral and, with no effect on final pixel magnitude, is eliminated as before. Setting $y' = \hat{y}'$ yields the range PSF

$$\text{PSF}_{FDA_{range}} = \rho_{\bar{\mathbf{r}}'}\int\limits_{\theta_{app}} d\theta_{app}\, \exp\left[-j2k_c \left(x' - \hat{x}'\right)\kappa_x\right] \ . \tag{5.30}$$

This PSF has the same form as Equation (2.101) and again the backprojection algorithm provides no range information. Setting $x' = \hat{x}'$ yields the cross-range PSF

$$\text{PSF}_{FDA_{cross\ range}} = \rho_{\bar{\mathbf{r}}'}\int\limits_{\theta_{app}} d\theta_{app}\, \exp\left[-j2k_c \left(y' - \hat{y}'\frac{\theta_{app}}{\theta_o}\right)\kappa_y\right] \ . \tag{5.31}$$

Table 5.2: Frequency progression is reduced by an order-of-magnitude as compared to Table 5.1 in order to observe the change in θ_{app}. N is increased by a proportional amount to ensure system bandwidth and center frequency remain constant.

Parameter	Value
Number Azimuth Elements (N)	450
Number Elevation Elements (P)	1
Base Operating Frequency (f_o)	10 GHz
Center Frequency (f_c)	10.44 GHz
Azimuth Frequency Progression (Δf_y)	2 MHz
Waveform Bandwidth	900 MHz
L	430 m
L_{app}	430 m

5.2.3 Simulation Results. Simulation is performed to empirically validate the approach proposed in Section 5.2.2. Through the remainder of this chapter, a series of three plots are used to show results for each simulation. The first plot displays the actual and apparent synthetic apertures. Blue O symbols represent actual collection location while red X symbols represent mapped collection locations. The second plot shows the reconstructed image when backprojected from the apparent synthetic aperture. The final plot highlights the center target, Target #6 in Figure 2.11, in order to show any effects on the PSF. The green dashed lines on center target plots outline theoretical range and cross-range resolutions of $\delta_x = \delta_y = 0.167$ m.

As a baseline, the mapping technique is applied to the scenario in Figure 2.11 with parameters used in Table 5.1. Recall that traditional backprojection produced a defoused image as shown in Figure 5.1. The apparent synthetic aperture and reconstructed image are shown in Figure 5.3. By creating the apparent synthetic aperture from which backprojection is performed, a focused image is produced. The first nulls of the PSF coincide with the theoretical range and cross-range resolutions outlined by the green dashed lines.

It is shown in Section 5.2.1 that θ_{app} varies inversely with Δf_y. Thus decreasing the frequency progression should yield a corresponding increase in apparent view angle. Simulation is performed with a modified set of FDA parameters shown in Ta-
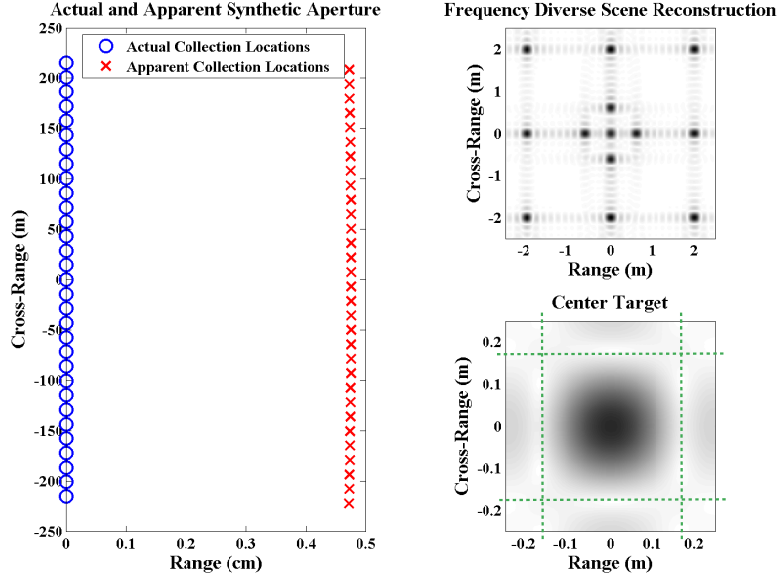
Figure 5.3: Blue O symbols represent actual collection location while red X symbols represent mapped collection locations. By creating the set of apparent collection locations from which backprojection is performed, the backprojection algorithm produces a focused image. The green dashed lines on center target plots outline theoretical range and cross-range resolutions.
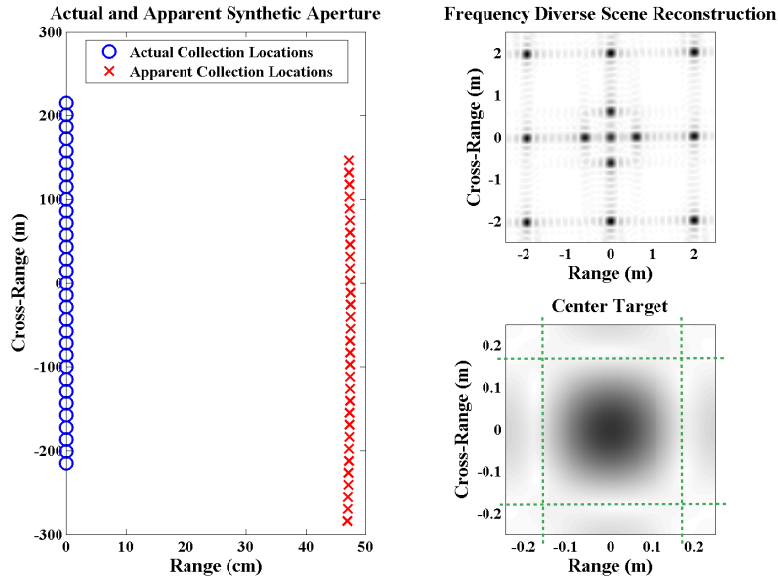

Figure 5.4: The effect of reducing frequency progression by a factor of 10 can be seen on the apparent synthetic aperture locations. The increased θ_{app} maps each actual collection location in the negative cross-range direction, though the overall length of the aperture is unchanged.

114

ble 5.2 to observe the effect of a smaller frequency progression on both the apparent synthetic aperture locations and reconstructed image. While the frequency progression is decreased by an order-of-magnitude to $\Delta f_y = 2$ MHz, it is noted the number of azimuth elements N are correspondingly increased by the same factor to $N = 450$. This change is performed to ensure system bandwidth given in Equation (4.18) and center frequency from Equation (4.6) remain constant and do not alter image resolution. However, the greater number of elements N does increase the physical antenna size.

The apparent synthetic aperture and reconstructed image are shown in Figure 5.4 when $\Delta f_y = 2$ MHz. The increased θ_{app} maps each actual collection location in the negative cross-range direction per Equation (5.14), though the overall length of the aperture is unchanged as noted by the observed $L_{app} = L$ given Table 5.2. The apparent synthetic aperture properly accounts for the drastic decrease in frequency progression and a focused image is produced. Image resolution remains unchanged.

In simulations performed thus far, a positive frequency is applied across the physical aperture. It is of interest to study the effect of inserting a negative frequency progression across array channels. Simulation with the parameters shown in Table 5.2 is performed once again, with the exception that $\Delta f_y = -2$ MHz. Figure 5.5 shows the resulting apparent synthetic aperture and reconstructed image. Each actual collection location is mapped in the positive cross-range direction. Once again, the length of the actual and apparent synthetic apertures are the same. The new apparent synthetic aperture properly accounts for the new frequency progression and a focused image is produced, and image resolution remains unchanged.

5.3   Improving Cross-Range Resolution

Section 5.2.3 aimed to validate the proposed methodology of Section 5.2.1. Through the scenarios presented, use of the apparent synthetic aperture for image reconstruction effectively compensated for the azimuth dependent PSF. Backprojec-
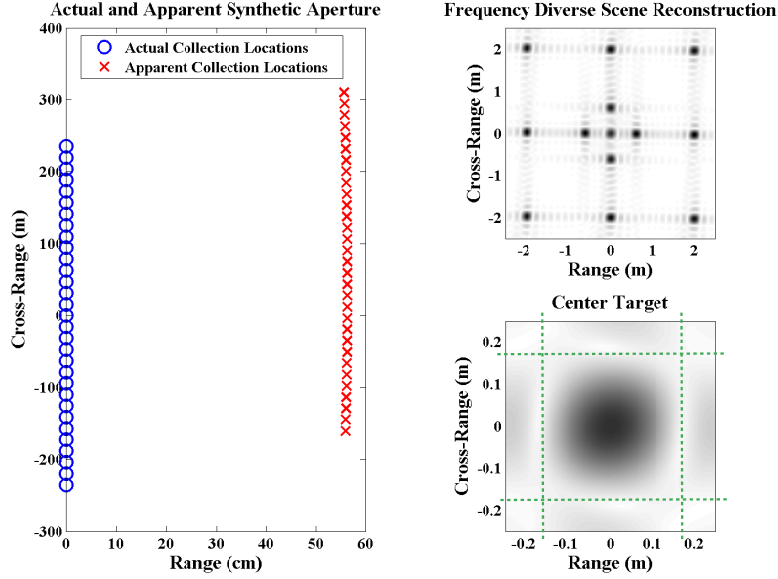
Figure 5.5: The effect of a negative frequency progression can be seen on the apparent synthetic aperture locations. The computed θ_{app} maps each actual collection location in the positive cross-range direction, though the overall length of the aperture is unchanged. The new apparent synthetic aperture properly accounts for the new frequency progression and a focused image is produced.

tion from the modified locations produced focused images with the theoretical range and cross-range resolutions of $\delta_x = \delta_y = 0.167$ m per parameters in Table 5.1 and Equation (2.1) and Equation (2.3). Waveform bandwidth is intentionally held constant across the various scenarios and lead to a consistent range resolution. It is observed that although the mapping produced an apparent synthetic aperture, the length of the new aperture and the actual aperture were approximately equal and cross-range resolution remained unchanged.

    5.3.1 Modified FDA Operation. From Equation (5.14) and Figure 5.4, a positive frequency progression produces an apparent synthetic aperture shifted in the negative cross-range dimension. A negative frequency progression produced the opposite effect as seen in Figure 5.5. Given the capability to map individual collection locations, it is proposed that FDA processing can increase apparent synthetic aperture length L_{app} and therefore improve cross-range resolution through a modified concept of

116

operations. Assuming the airborne collection platform flight path is along the cross-range axis from negative to positive, $+\Delta f_y$ is first used in the FDA. Thus, actual collection locations are projected back as in Figure 5.4. At the point where radar boresight crosses scene center, i.e., when the target area is perfectly broadside, the FDA reverts to a negative frequency progression of $-\Delta f_y$. Actual collection locations are then projected forward as in Figure 5.5.

An important consideration in the proposed approach is selection of base frequency. It is shown in Equation (4.6) that FDA center frequency is

$$\omega_c = \omega_o + \left(\frac{N-1}{2} \right) \Delta \omega_y , \tag{5.32}$$

and so

$$f_c = f_o + \left(\frac{N-1}{2} \right) \Delta f_y . \tag{5.33}$$

Simply changing the frequency progression from $+\Delta f_y$ to $-\Delta f_y$ at the center of the synthetic aperture causes the corresponding two subsets of the phase history to have differing center frequencies per Equation (5.33). For example, in Table 5.2 center frequency is shown to be $f_c = 10.44$ GHz. A frequency progression $\Delta f_y = -2$ MHz changes the center frequency to $f_c = 9.55$ GHz. When performing backprojection, pulse returns from each subset of the phase history will add incoherently corrupting the final image.

This challenge can be alleviated by changing the base frequency in conjunction with frequency progression. At the start of data collection, the reference element transmits at f_o while element $(N-1)$, i.e., the element furthest from the reference, transmits at

$$f_{(N-1)} = f_o + (N-1)\Delta f_y , \tag{5.34}$$

with center frequency given by Equation (5.33). At the point frequency progression is switched from positive to negative, the reference element operating frequency is set

to $f'_o = f_{(N-1)}$ with corresponding FDA center frequency

$$
\begin{aligned}
f_c &= f'_o + \left(\frac{N-1}{2}\right)(-\Delta f_y) \\
&= [f_o + (N-1)\Delta f_y] - \left(\frac{N-1}{2}\right)\Delta f_y \\
&= f_o + \frac{(N-1)}{2}\Delta f_y \,,
\end{aligned}
\tag{5.35}
$$

and is the same as Equation (5.33). A common center frequency is established across the phase history while achieving the desired mapping of collection locations with the change in Δf_y.

Three scenarios are considered to evaluate performance of the proposed procedure. Two scenarios consider the parameters in Table 5.1 and Table 5.2 with $N = 45$, $\Delta f_y = \pm 20$ MHz and $N = 450$, $\Delta f_y = \pm 2$ MHz respectively. One intermediate scenario with $N = 225$, $\Delta f_y = \pm 4$ MHz is used to provide an intermediate data point. Once again, waveform and collection parameters are set for equal range and cross-range resolution of $\delta_x = \delta_y = 0.167$ m. The results of processing are shown in Figure 5.6 to Figure 5.8.

Figure 5.6 displays the results of the baseline FDA case with $N = 45$, $\Delta f_y = \pm 20$ MHz. The apparent synthetic aperture is no longer continuous and the observed length is $L_{app} = 445$ m, an increase of 3% over the actual $L = 430$ m. L_{app} is computed as the cross-range difference between the first and last apparent collection locations. Though in theory a proportional improvement in cross-range resolution should be observed, the small difference is not visible on the scale presented. One artifact that is observed is an increase in peak sidelobe level (PSL), most noticeable in the Target #1 to Target #3 and Target #11 to Target #13 responses (reference Figure 2.11). The next two scenarios will show the trade-off presented between finer cross-range resolution and increased PSL.

Decreasing the magnitude of Δf_y by a factor of five, Figure 5.7 displays the results of $N = 225$, $\Delta f_y = \pm 4$ MHz. The apparent synthetic aperture is discontinuous
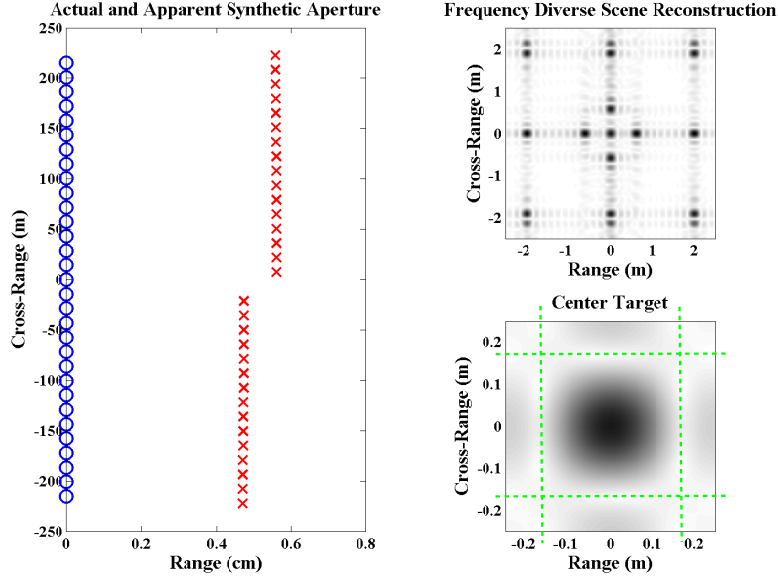
Figure 5.6: Results of processing an expanded synthetic aperture baseline using $N = 45$, $\Delta f_y = \pm 20$ MHz. The apparent synthetic aperture is no longer continuous and exceeds the actual aperture by 3%. A corresponding increase in cross-range resolution is not observed on the scale shown and an increase in peak sidelobes is noted.
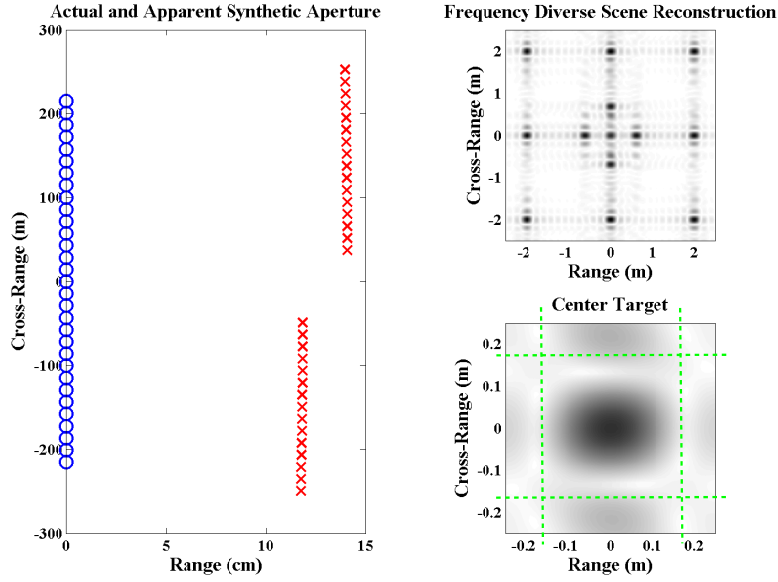

Figure 5.7: Results of processing an expanded synthetic aperture baseline using $N = 225$, $\Delta f_y = \pm 4$ MHz. With $L_{app} = 502$ m, cross-range resolution is improved at the cost of peak sidelobe level.

Actual and Apparent Synthetic Aperture

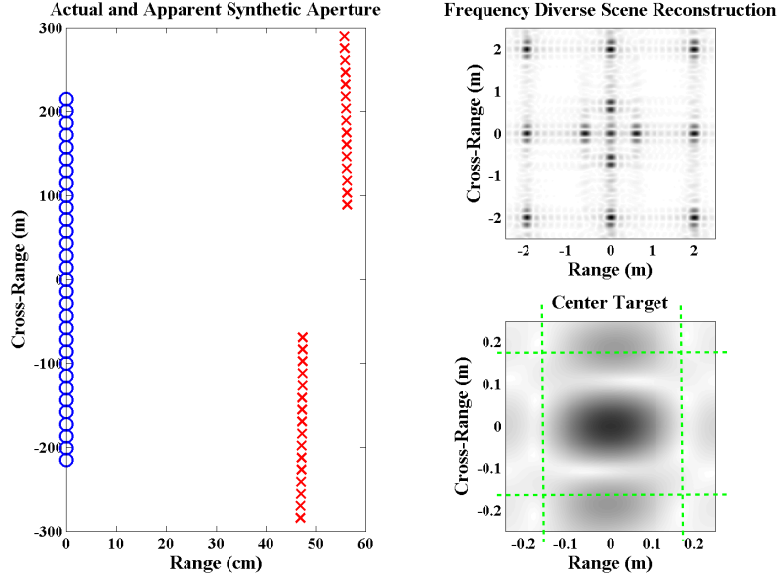**Frequency Diverse Scene Reconstruction**

Center Target

Figure 5.8: Results of processing an expanded synthetic aperture baseline using $N = 450$, $\Delta f_y = \pm 2$ MHz. With $L_{app} = 574$ m, cross-range resolution is further improved as compared to Figure 5.6 and Figure 5.7, at the cost of peak sidelobe level.

with a region in the center entirely omitted. With $L_{app} = 502$ m, an increase of 17% over the actual aperture length, and using small angle assumptions,

$$\Delta \theta_{app} \approx \frac{L_{app}}{R_c} \ , \tag{5.36}$$

the new expected cross-range resolution is $\delta_y = 0.143$ m. The first nulls in cross-range PSF of center target in Figure 5.7 occur within the theoretical values (green dashed box), and indicates finer cross-range resolution consistent with the new expected value. The PSL is more pronounced.

In the final simulation, the FDA uses $N = 450$, $\Delta f_y = \pm 2$ MHz with results shown in Figure 5.8. With the large region of no effective phase history, the apparent synthetic aperture can be interpreted as two distinct apertures. The observed L_{app} is 574 m, a full 33% increase over the baseline, and the new expected cross-range resolution is $\delta_y = 0.125$ m. The finer cross-range resolution is observed in conjunction with further elevated PSL.
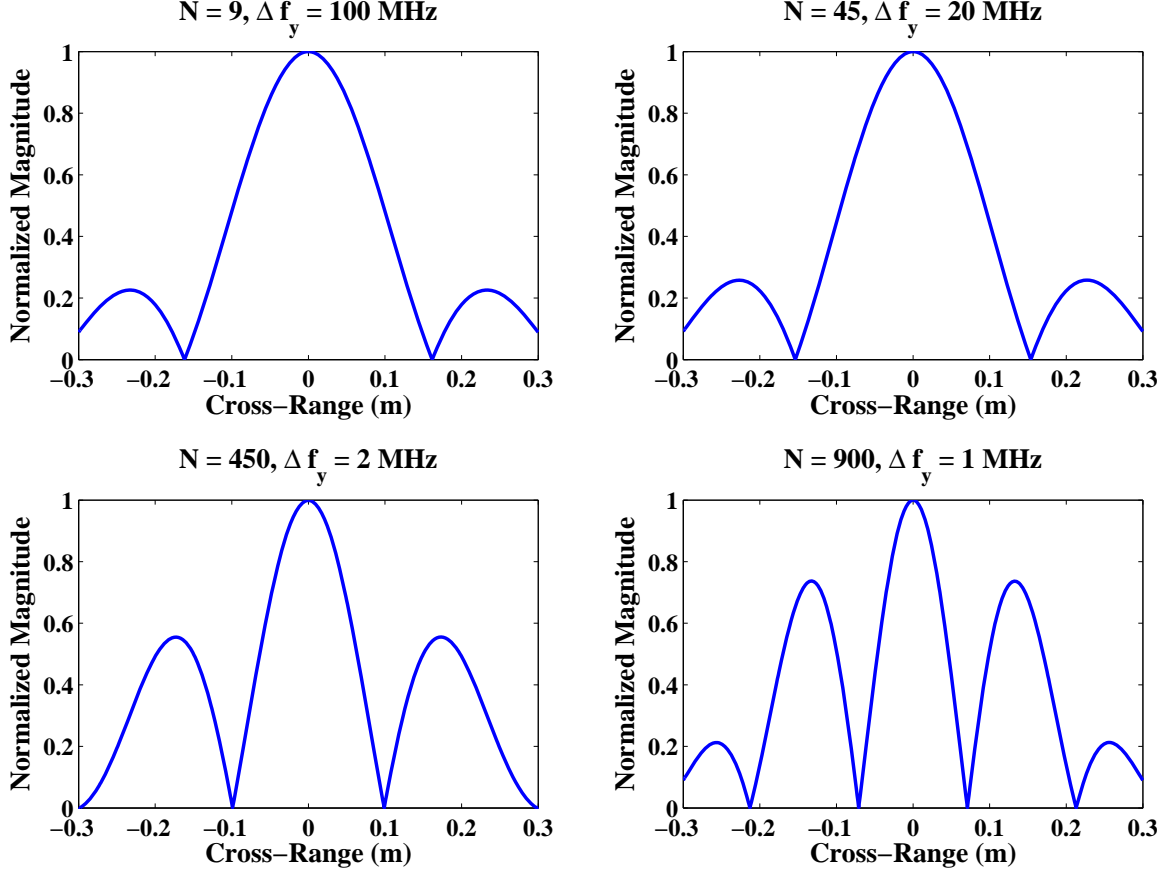
Figure 5.9: The cross-range PSF for Target #6 at scene center is shown for four $(N, \Delta f_y)$ pairs as indicated. The improvement in cross-range resolution, as given by the first nulls, and increase in PSL is seen with decreasing frequency progression.

5.3.2   Resolution Improvement and PSL Trends.   The FDA model developed in Chapter IV and FDA processing proposed in Section 5.3 allow continued analysis of varying Δf_y while noting effects on apparent synthetic aperture, image reconstruction, resolutions, etc. A main concern of a any SAR system is interpretability of resulting images. Fine resolution is desired to provide more detail, while sidelobe level must be kept low to prevent strong scatterers from masking adjacent weaker scatterers. It is of interest then to establish trends of improvement in cross-range resolution and increase in PSL.

In Figure 5.9, the cross-range PSF for Target #6 at scene center is shown for four $(N, \Delta f_y)$ pairs as indicated. The improvement in cross-range resolution, as given

by the first nulls, and increase in PSL is seen with decreasing frequency progression. The plots in Figure 5.9 represents snapshots of the effect of Δf_y on the PSF. In order to characterize the cross-range PSF attributes of resolution and PSL trends are shown in Figure 5.10 and Figure 5.11 respectively. This data and signal models developed under this research allow designers to optimize system design to suit specific operational requirements.

Figure 5.10 shows the improvement in cross-range resolution δ_y against Δf_y. Note a logarithmic x-axis is used to show two orders-of-magnitude change in Δf_y. Observed δ_y on the y-axis is normalized to the baseline $\delta_y = 0.167$ m resolution. A smaller observed δ_y corresponds to finer resolution, and a smaller normalized value is desirable. When the frequency progression is high, on the far right of the figure, little change in observed δ_y is noted as Δf_y decreases from 100 MHz to 10 MHz. However, between 10 MHz and 1 MHz the cross-range resolution is drastically improved. Though these results seem promising, the data in Figures 5.11 show the penalty paid in PSL. The Figures 5.11, PSL is referenced to the maximum target response giving the peak sidelobe level ratio (PSLR). At $\Delta f_y = 100$ MHz, PSLR $= -13$ dB is noted and this level is common in SAR. The PSLR degrades the cross-range PSF, especially between 10 MHz and 1 MHz.

5.4 FDA SAR Limitations

Limitations exist on the applicability for both FDA SAR processing techniques presented in Section 5.1 and Section 5.2. First, physical and hardware restrictions limit FDA size. In Section 5.2, trend analysis is performed for $\Delta f_y = 100$ MHz to $\Delta f_y = 1$ MHz. In order to satisfy the constant bandwidth constraint, the number of azimuth channels varied accordingly from $N = 9$ to $N = 900$. With inter-element spacing d_y fixed at $\lambda_c/2 = 0.14$ m, the array physical size increases from $D = 0.12$ m to $D = 12$ m and may not be be feasible for airborne systems. Additionally, strict restrictions are placed on associated hardware for each channel to operate precisely

on the assigned transmit frequency for the duration of the CPI. Clearly, this task is difficult for large arrays.

Next, recall small angle assumptions are used throughout the analytical development. Caution is required with any increase in θ_o to obtain a longer actual synthetic aperture, or corresponding θ_{app}, to achieve a longer apparent aperture. Such changes require that small angle assumptions be reverified.

Finally, the phase term in Equation (5.22) cannot be corrected for all possible scatterers in the scene. This limitation restricts the scene size over which the proposed processing can be applied. Targets at or near scene center appear most focused while those at increasing distances are more defocused. The extent of target defocusing depends on the difference between θ_o and θ_{app} and target distance from the scene center.
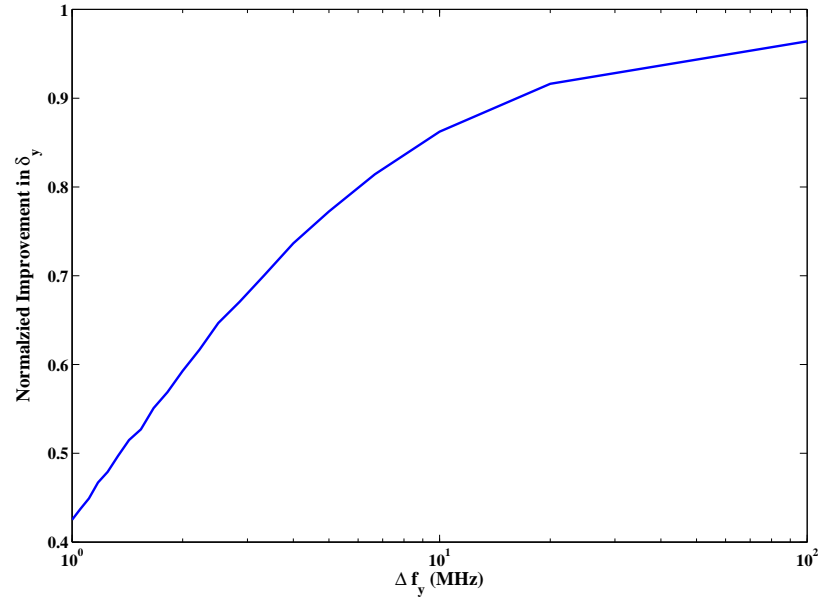
Figure 5.10: Little change in observed δ_y is noted as Δf_y decreases from 100 MHz to 10 MHz. However, between 10 MHz and 1 MHz the cross-range resolution is drastically improved.
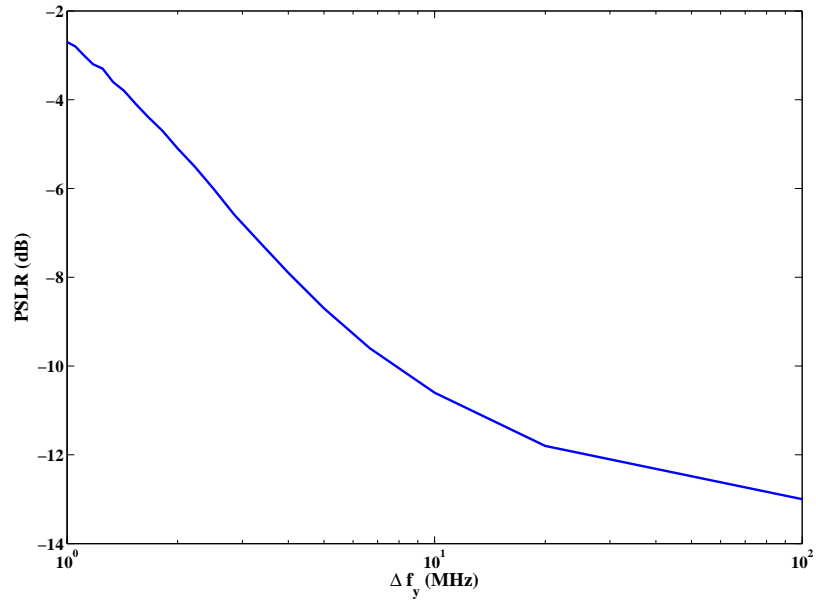

Figure 5.11: The PSLR degrades the cross-range PSF with decreasing Δf_y. The change is especially drastic between 10 MHz and 1 MHz.

VI. Conclusion

6.1 Research Summary

This research establishes a generalized formulation for applying waveform diversity to SAR. Though a majority of the effort focused on frequency diversity, the unique geometrical framework emphasizes three-dimensional data collection and enables the development of SAR signal modelling and imaging within the context of waveform diversity. A vector construct is used throughout the mathematical development as common across many disciplines. This presentation allows those unfamiliar with radar to better understand waveform diversity in the context of SAR.

Analytical formulation of the planar FDA extends previous work by considering a 2-D planar array with frequency progression across both dimensions. The capability to continually scan in azimuth and elevation, where scan periods are controlled solely by horizontal and vertical frequency progression, may have application beyond conventional spotlight SAR. Potential applications include stripmap SAR, GMTI, wide area surveillance, and STAP. The analysis and models developed under this research directly aid further study of FDA application to radar.

FDA pattern analysis enabled the development of a novel technique for producing a wideband, widebeam waveform through the use of an FDA. The wideband nature is not achieved through common approaches using complex radar hardware, phase coding, and/or pulse compression techniques. Rather, wideband performance is realized through simultaneous transmission of frequency offset sinusoidal tones. The frequency band coverage is easily scalable through the addition/removal of array elements without requiring redesign of waveform generators and other associated hardware. Though the FDA technique is addressed in the context of SAR imaging, a variety of radar applications may benefit from this new capability.

The FDA waveform is applied to SAR imaging through only minor modification of the existing backprojection algorithm. Two techniques were analyzed in applying the FDA waveform to SAR imaging. In the first method, a simple time and phase correction produced a focused SAR image with resolutions consistent with theoretical

values. This alone is a benefit as the new capability extends wideband waveforms available for SAR applications, with the advantage of simplicity in waveform generation and scalability to wider bandwidths.

The second approach exploits unique properties of the FDA waveform to improve cross-range resolution in SAR imagery. The creation of an apparent synthetic aperture from which backprojection is performed is a novel approach for enhancing SAR image resolution. Through manipulation of FDA frequency progression, target responses at individual collection locations are mapped to apparent collection locations. The synthesized apparent aperture is longer than the actual aperture and yields superior cross-range resolution. Though limits are placed on application of the proposed processing, this research represents an critical step in focusing attention on applying waveform diversity to improve cross-range resolution. For many years, efforts in waveform diversity have been directed at improving range resolution. However, the additional collection time required to achieve adequate cross-range resolution that collection platforms and aircrews unnecessarily exposed to hostile forces. As addressed here, FDA SAR processing aims to decrease the amount of time that Air Force personnel and equipment are in harm's way. The importance of this research has been recognized by the military community [20], the electromagnetics community [21], and the radar community [22],.

6.2   Suggestions for Further Research

Beyond frequency diversity, waveform diversity concepts could be studied using the constructs provided in Chapter II. Section 3.4.1 identified the conceptual similarity between stepped-frequency and FDA waveforms, the difference being the temporal versus spatial application of the frequency step. Similarly, the development in Chapter III can be extended to include other frequency-coded waveforms, e.g. Costas codes. These codes are popular and have nearly ideal range and doppler sidelobe behavior in the ambiguity function presented in Section 4.3 [33]. Costas codes are similar to the stepped-frequency waveform, except pulse coding is not based on

126

incremental frequency progression. Instead, frequency selection is based on Costas arrays designed for optimal ambiguity function behavior. When applying frequency assignment across the physical aperture, the associated array pattern can be derived using Equation (3.35)

$$s_T\left(t, \bar{\mathbf{r}}', \bar{\mathbf{r}}_o\right) = \sum_{n=0}^{N-1} \sum_{p=0}^{P-1} \exp\left[j\omega_{np}\left(t - t_o\right)\right] \exp\left(j\bar{\mathbf{k}}_{np} \cdot \bar{\mathbf{d}}_{np}\right) \exp\left(-j\bar{\mathbf{k}}_{np} \cdot \bar{\mathbf{r}}'\right) , \qquad (6.1)$$

where ω_{np} (and therefore $\bar{\mathbf{k}}_{np}$) is based on the chosen Costas code.

Alternatively, FDA parameters can be modified to provide array directivity. In Chapter IV, the FDA is shown to illuminate all azimuth angles. This may or may not be a desirable attribute for some radar applications. This limitation is easily overcome using subarrays, whereby elements in the $N \times P$ physical aperture are grouped into $R \times S$ subarrays, each of which acts as a CFA and can be steered to a particular azimuth and elevation angle. Instead of applying the frequency progression across elements in the traditional FDA fashion, the frequency progression can be applied across the subarrays. In this case, the modified aperture retains FDA functionality while gaining directivity.

Collection geometries beyond broadside SAR using linear flight paths may be of interest to study. The geometrical framework presented accommodates study of squinted geometries and/or arbitrary flight paths. Important research areas, like circular SAR, can effectively be addressed using the tools developed under this research. Additionally, this research exploited FDA patterns when only a horizontal frequency progression is present. The analytical models enable potential exploitation of vertical frequency progression which may help alleviate adverse 3-D SAR effects (like range layover) or help analyze a 3-D PSF behavior.

Lastly, scene sizes in Chapter V were intentionally limited to keep simulation times manageable. It is of interest to observe the proposed FDA SAR operations on larger scenes. One tool readily available to support such an investigation is the

Research Lab Space-Time Adaptive Processing (RLSTAP) simulation. With the high fidelity radar hardware models and ability to generate complex signal data based on real-world terrain data, RLSTAP may be the ideal tool for analyzing FDA SAR performance on extended targets.

Bibliography

1. *Alternatives for Military Space Radar*. Technical report, Congress of the United States, 2007.

2. Antonik, Paul, Michael C. Wicks, Hugh D. Griffiths, and Christopher J. Baker. "Frequency Diverse Array Radars". *Proceedings 2006 IEEE Radar Conference*. 2006.

3. Antonik, Paul, Michael C. Wicks, Hugh D. Griffiths, and Christopher J. Baker. "Multi-Mission Multi-Mode Waveform Diversity". *Proceedings 2006 IEEE Radar Conference*. 2006.

4. Antonik, Paul, Michael C. Wicks, Hugh D. Griffiths, and Christopher J. Baker. "Range-Dependent Beamforming Using Element Level Waveform Diversity". *2006 Waveform Diversity Conference*. 2006.

5. Baizert, Piotr. *Forward-looking Radar Clutter Suppression using Frequency Diverse Arrays*. Master's thesis, Air Force Institute of Technology, 2006.

6. Baizert, Piotr, Todd B. Hale, Michael A. Temple, and Michael C. Wicks. "Forward-looking Radar GMTI Benefits Using a Linear Frequency Diverse Array". *Electronics Letters*, 42(22), October 2006.

7. Balanis, Constantine A. *Advanced Engineering Electromagnetics*. John Wiley & Sons, Inc., New York NY, 1989.

8. Balanis, Constantine A. *Antenna Theory Analysis and Design, 3rd Edition*. John Wiley & Sons, Inc., Hoboken NJ, 2005.

9. Bolton, A. G., N. S. Martin, and L. C. Jain. "A Technique for Enhanced Slant Range Resolution for SAR Systems in Knowledge-Based Environment". *IEEE Aerospace and Electronic Systems Magazine*, 9(8), August 1994.

10. Brookner, Eli. "Phased-Array and Radar Breakthroughs". *Proceedings 2007 IEEE Radar Conference*. 2007.

11. Buckreuss, S., R. Werninghaus, and W. Pitz. "The German Satellite Mission TerraSAR-X". *Proceedings 2008 IEEE Radar Conferences*. 2008.

12. Carrara, Walter G., Ron S. Goodman, and Ronald M. Majewski. *Spotlight Synthetic Aperture Radar: A Signal Processing Algorithms*. Artech House, Boston MA, 1995.

13. Cerutti-Maori, D., W. Burger, J. H. G. Ender, and A. R. Brenner. "Experimental Results of Ground Moving Target Detection Achieved with the Multi-Channel SAR/MTI System PAMIR". *Proceedings 2005 European Radar Conference*. 2005.

14. Cho, Z. H., C. M. Chen, and S. Y. Lee. "Incremental Algorithm - A New Fast Backprojection Scheme for Parallel Beam Geometries". *IEEE Transactions on Medical Imaging*, 9(2), June 1990.

15. Cook, Charles E. and W. M. Siebert. "The Early History of Pulse Compression Radar". *IEEE Transactions on Aerospace and Electronic Systems*, 24(6), November 1988.

16. Cumming, Ian G. and Frank H. Wong. *Digital Processing of Synthetic Aperture Radar Data*. Artech House, Boston MA, 2005.

17. Ender, J. H. G. "Space-time Processing for Multichannel Synthetic Aperture Radar". *Electronics and Communication Engineering Journal*, 11(1), February 1999.

18. Ender, J. H. G. "Liner and Non-linear Techniques for Multi-Channel SAR Image Generation". *Proceedings 2000 EUSAR Conference*. 2000.

19. Ender, J. H. G. and A. R. Brenner. "PAMIR - A Wideband Phased-Array SAR/MTI System". *IEE Proceedings - Radar, Sonar, Navigation*, 150(3), June 2003.

20. Farooq, Jawad, Michael A. Saville, and Michael A. Temple. "Application of Frequency Diverse Array Processing to Improve Synthetic Aperture Radar Imaging". *Proceedings 2008 Tri-Service Radar Symposium Waveform Diversity Workshop*. 2008.

21. Farooq, Jawad, Michael A. Temple, and Michael A. Saville. "Application of Frequency Diverse Arrays to Synthetic Aperture Radar Imaging". *Proceedings 2007 International Conference on Electromagnetics in Advanced Applications*. 2007.

22. Farooq, Jawad, Michael A. Temple, and Michael A. Saville. "Exploiting Frequency Diverse Array Processing to Improve SAR Image Resolution". *Proceedings 2008 IEEE Radar Conference*. 2008.

23. Gao, Guozhong and Carlos Torres-Verdin. "High-Order Generalized Extended Born Approximation for Electromagnetic Scattering". *IEEE Transactions on Antennas and Propagation*, 54(4), April 2006.

24. Goodman, N. A., Sih-Chung-Lin, D. Rajakrishna, and J.M. Stiles. "Processing of Multiple-Receiver Spaceborne Arrays for Wide-Area SAR". *IEEE Transactions on Geoscience and Remote Sensing*, 40(4), April 2002.

25. Hale, Todd B. "EENG 668 Advanced Radar Systems Analysis", 2005. Course Notes.

26. Hale, Todd B. "EENG 535 Radar Systems Analysis", 2006. Course Notes.

27. Himed, Braham and Mehrdad Soumekh. "Synthetic Aperture Radar Moving Target Indicator Processing of Multi-Channel Airborne Radar Measurement Data". *IEE Proceedings - Radar, Sonar, Navigation*, 153(6), December 2006.

28. Huang, Jingjing, Kin-Fai Tong, and C. J. Baker. "Frequency Diverse Array with Beam Scanning Feature". *Proceedings 2008 Antennas and Propagation Society International Symposium*. 2008.

29. Jakowatz, Charles V., Daniel E. Wahl, Paul H. Eichel, Dennis C. Ghiglia, and Paul A. Thompson. *Spotlight-mode Synthetic Aperture Radar: A Signal Processing Approach*. Kluwer Academic Publishers, Boston MA, 1996.

30. Klemm, Richard. *Principles of Space-Time Adaptive Processing*. IEE Publishing, United Kingdom, 2002.

31. Krieger, Gerhard, Nicolas Gebert, and Alberto Moreira. "Multidimensional Waveform Encoding: A New Digital Beamforming Technique for Synthetic Aperture Radar Remote Sensing". *IEEE Transactions on Geoscience and Remote Sensing*, 46(1), January 2008.

32. Lathi, B. P. *Signal Processing and Linear Systems*. Oxford University Press, New York NY, 1998.

33. Levanon, Nadav and Eli Mozeson. *Radar Signals*. Wiley - IEEE Press, Hoboken NJ, 2004.

34. Martin, N. S. "SAR Systems Resolution Reviewed for Target Classification in Knowledge-Based Environment". *Proceedings Electronic Technology Directions to the Year 2000, 1995*. 2005.

35. Muehe, Charles E. and Melvin Labitt. "Displaced-Phase-Center Antenna Technique". *Lincoln Laboratory Journal*, 12(2), 2000.

36. Munson, David C. "An Introduction to Strip-Mapping Synthetic Aperture Radar". *Proceedings IEEE International Conference on Acoustics, Speech, and Signal Processing*. 1987.

37. Munson, David C., James D. O'Brien, and W. Kenneth Jenkins. "A Tomographic Formulation of Spotlight-Mode Synthetic Aperture Radar". *Proceedings of the IEEE*, 71(8), August 1983.

38. Munson, David C. and Jorge L. C. Sanz. "Image Reconstruction from Frequency-Offset Fourier Data". *Proceedings of the IEEE*, 72(6), June 1984.

39. Munson, David C. and Robert L. Visenten. "A Signal Processing View of Strip-Mapping Synthetic Aperture Radar". *IEEE Transaction on Acoustics, Speech, and Signal Processing*, 37(12), December 1989.

40. Nie, X., D. Y. Zhu, and Z. D. Zhu. "Application of Synthetic Bandwidth Approach in SAR Polar Format Algorithm Using the Deramp Technique". *Progress In Electromagnetics Research*, 80, 2008.

41. Olsen, R. C. *Remote Sensing from Air and Space*. SPIE Press, Bellingham WA, 2007.

42. Oppenheim, Alan V., Ronald W. Schafer, and John R. Buck. *Discrete-Time Signal Processing, 2nd Edition*. Prentice Hall, Upper Saddle River NJ, 1999.

43. Richards, Mark A. "A Beginner's Guide to Interferometric SAR Concepts and Signal Processing". *IEEE Aerospace and Electronic Systems Magazine*, 22(9), September 2007.

44. Rosenberg, Luke and Doug Gray. "Multichannel SAR Imaging with Backprojection". *Proceedings 2004 Intelligent Sensors, Sensor Networks and Information Processing Conference*. 2004.

45. Saville, Michael A. Personal Communication, 2008.

46. Saville, Michael A. "EENG 714 Advanced Topics in Radar Applications", 2008. Course Notes.

47. Schimpf, H., A. Wahlen, and H. Essen. "High Range Resolution by Means of Synthetic Bandwidth Generated by Frequency-Stepped Chirps". *IET Electronic Letters*, 39(18), September 2003.

48. Secmen, Mustafa, Simsek Demir, Altunkan Hizal, and Taylan Eker. "Frequency Diverse Array Antenna with Periodic Time Modulated Pattern in Range and Angle". *Proceedings 2007 IEEE Radar Conferences*. 2007.

49. Skolnik, Merrill I. *Introduction to Radar Systems*. McGraw Hill, Boston MA, 2001.

50. Skolnik, Merrill I. *Radar Handbook*. McGraw Hill, New York NY, 2008.

51. Soumekh, Mehrdad. *Synthetic Aperture Radar Signal Processing with MATLAB Algorithms*. John Wiley & Sons, Inc., New York NY, 1999.

52. Stimson, George W. *Introduction to Airborne Radar*. SciTech Publishing, Inc., Mendham NJ, 1998.

53. Sullivan, Roger J. *Radar Foundations for Imaging and Advanced Concepts*. SciTech Publishing, Inc., Raleigh NC, 2004.

54. Taflove, Allen and Susan C. Hagness. *Computational Electrodynamics: The Finite-Difference Time-Domain Method, 3rd Edition*. Artech House, Boston MA, 2005.

55. Wicks, Michael C. 2009 Waveform Diversity Tutorial, 2009.

56. Xu, JianJun, TatSoon Yeo, and Pangshyan Kooi. "Simulated STAP Performance for Multi-Channel SAR Processing". *Proceedings IEEE 2000 International Geoscience and Remote Sensing Symposium*. 2000.

57. Yegulalp, Ali F. "Fast Backprojection Algorithm for Synthetic Aperture Radar". *Proceedings 1999 IEEE Radar Conference*. 1999.

58. Younis, M., C. Fisher, and W. Wiesbeck. "Digital Beamforming in SAR Systems". *IEEE Transactions on Geoscience and Remote Sensing*, 41(7), July 2003.

REPORT DOCUMENTATION PAGE

1. REPORT DATE *(DD-MM-YYYY)*	2. REPORT TYPE	3. DATES COVERED *(From – To)*
26-03-2009	Doctoral Dissertation	September 2005-March 2009

4. TITLE AND SUBTITLE

Frequency Diversity for Improving Synthetic Aperture Radar Imaging

5a. CONTRACT NUMBER

5b. GRANT NUMBER

5c. PROGRAM ELEMENT NUMBER

6. AUTHOR(S)

Farooq, Jawad, Major, USAF

5d. PROJECT NUMBER
JON# 09244

5e. TASK NUMBER

5f. WORK UNIT NUMBER

7. PERFORMING ORGANIZATION NAMES(S) AND ADDRESS(S)

Air Force Institute of Technology
Graduate School of Engineering and Management (AFIT/EN)
2950 Hobson Way
WPAFB OH 45433-7765 DSN: 785-3636

8. PERFORMING ORGANIZATION REPORT NUMBER

AFIT/DEE/ENG/09-04

9. SPONSORING/MONITORING AGENCY NAME(S) AND ADDRESS(ES)

Air Force Research Laboratory
Attn: AFRL/RY (Dr. Michael Wicks)
26 Electronics Parkway
Rome, NY 13441-4514
Michael.Wicks@rl.af.mil
COMM: (315) 330-2556, DSN: 587-2556

10. SPONSOR/MONITOR'S ACRONYM(S)
AFRL

11. SPONSOR/MONITOR'S REPORT NUMBER(S)

12. DISTRIBUTION/AVAILABILITY STATEMENT

APPROVED FOR PUBLIC RELEASE; DISTRIBUTION UNLIMITED

13. SUPPLEMENTARY NOTES

14. ABSTRACT

In this work, a novel theoretical framework is presented for using recent advances in frequency diversity arrays (FDAs). Unlike a conventional array, the FDA simultaneously transmits a unique frequency from each element in the array. As a result, special time and space properties of the radiation pattern are exploited to improve cross-range resolution. The idealized FDA radiation pattern is compared with and validated against a full-wave electromagnetic solver, and it is shown that the conventional array is a special case of the FDA. A new signal model, based on the FDA, is used to simulate SAR imagery of ideal point mass targets and the new model is used to derive the impulse response function of the SAR system, which is rarely achievable with other analytic methods. This work also presents an innovative solution for using the convolution back-projection algorithm, the gold standard in SAR image processing, and is a significant advantage of the proposed FDA model. The new FDA model and novel SAR system concept of operation are shown to reduce collection time by 33 percent while achieving a 4.5 dB improvement in cross-range resolution as compared to traditional imaging systems.

15. SUBJECT TERMS
SAR, Frequency Diverse Arrays, Waveform Diversity

16. SECURITY CLASSIFICATION OF:			17. LIMITATION OF ABSTRACT	18. NUMBER OF PAGES	19a. NAME OF RESPONSIBLE PERSON
REPORT U	**ABSTRACT** U	**c. THIS PAGE** U	UU	151	Major Michael A. Saville (ENG)

19a. NAME OF RESPONSIBLE PERSON
Major Michael A. Saville (ENG)

19b. TELEPHONE NUMBER *(Include area code)*
(937) 255-3636 x4719; email: Michael.Saville@afit.edu